Dissertation

submitted to the

Combined Faculty of Mathematics, Engineering and Natural Sciences

of Heidelberg University, Germany

for the degree of

Doctor of Natural Sciences

Put forward by

Julia Ines Jäger

born in: Karlsruhe, Germany

Oral examination: 24.07.2025

Progress on antiproton cooling and an improved direct limit on the antiproton lifetime

Referees: Prof. Dr. Klaus Blaum
Prof. Dr. Ulrich Uwer

Progress on antiproton cooling and an improved direct limit on the antiproton lifetime

Abstract The Baryon Antibaryon Symmetry Experiment (BASE) probes CPT symmetry by comparing the fundamental properties of protons and antiprotons with highest precision. We have compared proton/antiproton charge-to-mass ratios with a fractional precision of 16 parts in a trillion and proton and antiproton magnetic moments with a precision on the parts per billion level. Located at CERN's Antimatter Factory, BASE is currently constrained to perform the high-precision studies within the accelerator shutdown period. For this purpose, several antiprotons are caught and then stored almost indefinitely in a dedicated Reservoir trap.

High precision g-factor measurements require regular re-cooling of an isolated antiproton. This thesis describes the characterization and optimization of a novel cyclotron-mode cooling device, which lowers the cyclotron mode cooling time from previously 15 hours to only 8 minutes and thus enables us to maximize the number of measurement cycles in the limited window of opportunity. With the improved cooling performance, the spin transition detection error rate is reduced by more than three orders of magnitude to < 0.000023.

Furthermore, the optimization and routine operation of the Reservoir trap enabled us to store antiprotons for (up until now) 1.5 years, with a typical consumption rate of about one particle per two months for experimental purposes, highlighting the feasibility of long-term measurement campaigns and experiments with extremely rare species. By continuously monitoring the stored antiprotons in this time range, this thesis extracts a direct lower limit on the antiproton lifetime of 52.54 years with a confidence level of 68%. This improves the previous best value by a factor of five.

Fortschritt bei der Antiprotonenkühlung und eine verbesserte direkte Untergrenze der Antiprotonenlebensdauer

Zusammenfassung Das Baryon Antibaryon Symmetry Experiment (BASE) untersucht CPT-Symmetrie, indem es die grundlegenden Eigenschaften von Protonen und Antiprotonen mit höchster Präzision vergleicht. Wir haben die Ladungs-zu-Masse-Verhältnisse von Protonen und Antiprotonen mit einer Genauigkeit von 16 p.p.t. und das magnetische Moment von Protonen und Antiprotonen mit einer Genauigkeit im Bereich p.p.b.

verglichen. Das BASE-Experiment befindet sich in der Antimateriefabrik des CERNs und ist derzeit auf hochpräzise Messungen während der Stillstandszeit des Beschleunigers beschränkt. Zu diesem Zweck werden mehrere Antiprotonen eingefangen und dann nahezu unbegrenzt in einer speziellen Reservoir-Falle gespeichert.
Hochpräzise g-Faktor-Messungen erfordern eine regelmäßige Nachkühlung eines isolierten Antiprotons. Diese Arbeit beschreibt die Charakterisierung und Optimierung eines neuartigen Kühlapparats für die modifizierte Zyklotronmode, der die benötigte Kühlzeit von bisher 15 Stunden auf nur 8 Minuten verkürzt und es uns somit ermöglicht, die Anzahl der Messzyklen in dem begrenzten Zeitfenster zu maximieren. Mit der verbesserten Kühlung konnte die Fehlerrate bei der Spinübergangsdetektion um mehr als drei Größenordnungen auf $< 0,000023$ reduziert werden. Darüber hinaus ermöglichten uns die Optimierung und der routinemäßige Betrieb der Reservoir-Falle die Speicherung von Antiprotonen für (bislang) 1,5 Jahre bei einer typischen Verbrauchsrate von etwa einem Teilchen alle zwei Monate für experimentelle Zwecke, was die Durchführbarkeit von Langzeitmesskampagnen und Experimenten mit extrem seltenen Teilchen unterstreicht. Durch kontinuierliche Überwachung der in diesem Zeitraum gespeicherten Antiprotonen wurde innerhalb dieser Dissertation eine direkte Untergrenze für die Antiprotonenlebensdauer von 52,54 Jahren mit einer Konfidenz von 68% ermittelt. Dies verbessert den bisherigen Bestwert um einen Faktor fünf.

Contents

Chapter 1

Introduction

The Standard Model (SM) of particle physics [1] has been tested in numerous experiments and, on many occasions, has produced theoretical predictions about the existence of particles prior to their experimental discovery. This includes, for example, the discovery of the exchange quanta of the weak interaction ($W^{\pm}$ & Z^0) [2–5], the detection of the top-quark [6, 7], and culminated in the discovery of the Higgs-Boson [8, 9].

Despite its tremendous success, the Standard Model has numerous shortcomings. For instance, it does not include gravity – one of four known fundamental forces. Another shortcoming is its inability to describe large parts of the composition of the universe. According to data from the PLANCK space telescope [10], the universe consists of approximately 69% dark energy, 26% dark matter, and only 5% of baryonic matter. It is only this small latter fraction – described by the SM – that forms stars, planets, and other celestial bodies. And even these 5% have yet to be understood. For example, the observation of neutrino oscillation contradicts the massless nature of SM-neutrinos [11].

One of the most pressing questions of modern physics is the striking imbalance of matter and antimatter in the universe. The Standard Model is a local, Lorentz invariant quantum field theory, and as such, it is invariant under the combined transformation of charge (C), parity (P) and time (T) [1]. According to the CPT-theorem [12, 13], particles and their antiparticle-conjugates are perfect mirror images of each other, implying equal production during the Big Bang [14]. Yet, during the earliest moments of the universe, an excess of baryons over antibaryons emerged, which is referred to as baryogenesis [15].

Combining the SM and the cosmological Λ-CDM model, the expected radiative universe would yield equal densities of baryons and antibaryons $N_{\mathrm{B}} = N_{\bar{\mathrm{B}}}$, and a baryon-to-photon ratio of $N_{\mathrm{B}} \approx N_{\bar{\mathrm{B}}} \approx 10^{-18} N_{\gamma}$. However, observations indicate a significantly larger

baryon/antibaryon asymmetry, quantified by the parameter η [1, 16]:

$$\eta = \frac{N_{\mathrm{B}} - N_{\bar{\mathrm{B}}}}{N_{\gamma}} \approx 10^{-10}, \tag{1.1}$$

where N_{B}, $N_{\bar{\mathrm{B}}}$, N_{γ} are the numbers of baryons, antibaryons, and photons, respectively. This observed value is more than eight orders of magnitude larger than the prediction of our best theories [1].

A pioneer dealing with baryogenesis was Andrei Sakharov. He proposed three necessary conditions to explain the baryogenesis, which are now known under his name [17, 18]:

1. Baryon number violation:
   In order for a difference in abundance of matter and antimatter to exist, the baryon number, normally conserved, has to be violated.

2. C- and CP-violation:
   In case of CP-conservation, for each reaction that would generate more antibaryons than baryons, a CP conjugate reaction would exist generating more baryons than antibaryons.

3. Interaction out of thermal equilibrium:
   In thermal equilibrium, all baryon number violating processes will be balanced by their corresponding inverse reaction. In order to generate more baryons over antibaryons, the violating process has to happen out of thermal equilibrium.

Although CP-violation was discovered – first indirectly in Kaon decay [19], later also directly [20–25], and most recently in baryons [26] – it is not sufficient to explain the observed baryon asymmetry in the universe [16]. A different explanation for the baryogenesis could be caused by CPT-violation together with baryon number violation [27].

As a consequence of the fundamental CPT symmetry of the SM [28], particles and antiparticles have identical masses and lifetimes, as well as equal but opposite electric charges and magnetic moments. Additionally, matter and their corresponding antimatter counterparts have exactly the same energy spectrum [28]. Consequently, experiments are inspired to compare and test these fundamental properties in matter and their antimatter conjugates with the highest precision.

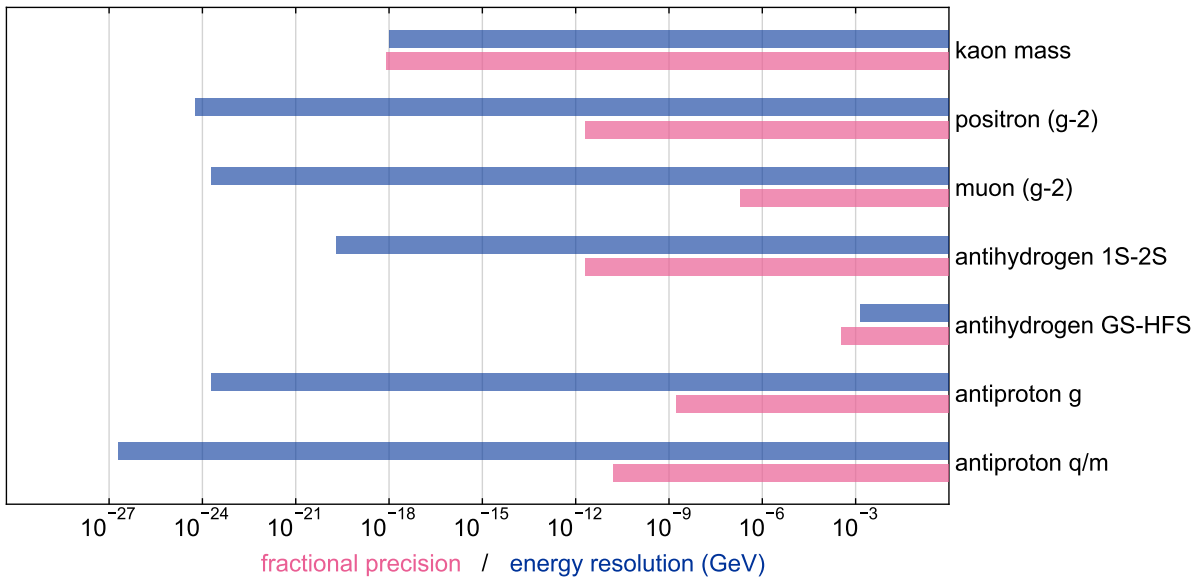

Figure 1.1: Selection of several CPT tests in matter/antimatter systems. The pink bars show the fractional precision of the experiments, while the blue bars shows the energy resolution $\Delta E = h\Delta\nu$ which is typically used in the Standard Model Extension.

1.1 Test of CPT symmetry

As CPT symmetry is a fundamental property of the Standard Model, no established fundamental physics theory introduces a CPT-violating effect [28]. However – inspired by interactions in string theories that lead to spontaneous breaking of Lorentz invariance [29] – Alan Kostelecky and colleagues proposed an effective field theory allowing for Lorentz- and CPT violation [30, 31] based on a minimal extension of the Standard Model. This so-called Standard Model Extension (SME) provides coupling coefficients of the Lorentz violating terms with the Standard Model, which can be constrained by experimental observations [32]. In this context, exotic interactions V_e cause variations of the energy levels E_k of the system under study, resulting in modified energy levels $E_k + \Delta E_k$ with $\Delta E_k = \langle\psi|V_e|\psi\rangle$. Here, ψ is the eigenstate of the unperturbed Hamiltonian H_0, such that $E_k = \langle\psi|H_0|\psi\rangle$. For example, H_0 might represent a charged particle in a Penning trap. In order to compare CPT tests within different systems, it is therefore practical to compare the energy resolution of the measurements instead of fractional precision, and it is thus used to constrain the coefficient strength in SME [32].

Numerous experiments across different sectors have tested CPT symmetry, given that neither the physical system nor the precision scale at which CPT violation might occur

is currently known. Figure 1.1 shows several of these experiments giving the fractional measurement precision and energy resolution. For example, the mass difference of neutral K_0 and $\bar{K}_0$ mesons have been measured to a fractional precision of 8×10^{-19} by comparing decay channels of neutral and charged pions [33]. This constrains SME coefficients to $< 10^{-18}$ GeV. In the leptonic sector, pioneering Penning trap experiments have compared the electron and position g-factor with a fractional precision of 2 parts per trillion (p.p.t.) [34], corresponding to an energy resolution of $< 6 \times 10^{-25}$ GeV. Despite being conducted in 1987, this comparison remains one of the most stringent CPT tests in the leptonic sector to date. For the muon μ^- and antimuon μ^+, the $g - 2$ values where recently compared with a fractional precision of 0.2 p.p.m. [35] constraining SME coefficients to $< 2 \times 10^{-24}$.

In the baryonic sector, CPT tests with low-energetic antimatter are conducted at the unique Antimatter Factory (AMF) [36] at CERN. Here, 100 keV antiprotons are made available to six collaborations performing experiments using baryonic antimatter: AEGIS [37], ALPHA [38, 39], ASACUSA [40], BASE [41], GBAR [42] and PUMA [43]. AEGIS, GBAR and a part of the ALPHA collaboration are testing the gravitational behavior of antihydrogen [39]. The PUMA collaboration aims to use antiprotons as targets for scattering of neutron rich nuclei to investigate neutron skins [43]. For this, they plan to transport antiprotons from the AMF to CERN's radioactive ion beam facility ISOLDE.

The ASACUSA collaboration is set out to measure the ground state hyperfine splitting of antihydrogen in flight, which they have already demonstrated using hydrogen [44]. Another part of the ASACUSA collaboration performs high-resolution spectroscopy of exotic antiprotonic helium atoms [45].

The first milestone of the AMF physics program was the production of cold antihydrogen by the ATHENA and ATRAP collaborations [46, 47]. Building on the achievements of the ATHENA experiment, and after about ten years of development time [48], the ALPHA collaboration tests CPT symmetry to highest precision. In 2017, they reported on a measurement of the ground-state hyperfine splitting in antihydrogen, achieving a fractional resolution of 350 parts per million (p.p.m.) [49]. This was followed by a breakthrough achievement of the characterization of the 1S–2S transition with a fractional resolution of 2 parts per trillion (p.p.t.), corresponding to an absolute energy sensitivity of 2×10^{-20} GeV [50]. The recent demonstration of laser [51] and adiabatic cooling [52] of trapped antihydrogen promises an increased precision measurement in due time [53].

Contrary to the majority of the collaborations in the AMF, which investigate properties of antihydrogen, the BASE collaboration performs high-precision measurements on

the fundamental properties of single antiprotons, hence testing CPT-symmetry. This includes the determination of the proton-to-antiproton charge-to-mass ratio [54, 55], the determination of the proton and antiproton magnetic moments [56–58], and lifetime limits on the antiproton [59]. In 2017, BASE determined the antiproton magnetic moment on the parts per billion (p.p.b) level [56], improving the previous best result by more than a factor of 3000 [60] and reaching an energy resolution $< 2 \times 10^{-24}\,\mathrm{GeV}$. Most recently, BASE reported on a measurement of the proton-to-antiproton charge-to-mass ratio with a fractional precision of 16 p.p.t., corresponding to an energy resolution of $< 2 \times 10^{-27}\,\mathrm{GeV}$, which is the most precise test of CPT symmetry in the baryon sector to date. To further improve these limits, the BASE collaboration is currently implementing the transportable trap system BASE-STEP [61]. Our goal is to use this transportable trap system to move antiprotons out of the accelerator environment of the AMF and to inject them into dedicated precision experiments located in calm laboratory space. Very recently, we have demonstrated a first major milestone towards this goal, and have transported protons out of the AMF of CERN [62]. On the long term and based on this strategy, we are aiming at antiproton precision studies at 10 to 100-fold improved fractional resolution, compared to our current best results.

To date, none of the experiments mentioned above have yielded any evidence of CPT violation, while simultaneously providing tests of CPT invariance with improvements of million-fold in precision.

Outline of the thesis

This thesis presents the development, implementation, and characterization of critical upgrades to the advanced cryogenic Penning trap system used in the BASE (Baryon Antibaryon Symmetry Experiment) collaboration at CERN. These improvements are designed to enhance the precision in measuring the antiproton magnetic moment and to establish a new direct lower limit on the antiproton lifetime – key objectives in ongoing efforts to test the fundamental symmetries of nature, particularly CPT invariance.

The work begins with a discussion of the theoretical motivation underpinning CPT symmetry tests using antimatter. In this context, Penning trap experiments play a pivotal role, offering a unique environment to confine charged particles and allow their fundamental properties to be examined with extraordinary precision. A comprehensive overview of

Penning trap physics is presented in Chapter 2 followed by a technical presentation of the BASE experimental setup in Chapter 3. This includes a detailed account of the instrumentation and methodologies employed for high-precision measurements of the magnetic moments of both the proton and the antiproton.

A central focus of this thesis lies in the implementation of advanced g-factor measurement schemes. These techniques form the basis for determining the magnetic moment of single particles confined within a Penning trap, which requires meticulous control over particle motion and environmental conditions. In pursuit of this goal, a novel mode-cooling device was developed and characterized as part of this thesis. This innovation has significantly improved the thermal stability and signal-to-noise ratio of antiproton measurements. The results of this work, which demonstrate the device's impact on reducing motional energy and improving measurement precision, have been published in Physical Review Letters [63] and are summarized in Chapter 4.

Further contributions involve the BASE Reservoir Trap, a sophisticated system essential for the long-term storage and manipulation of antiprotons. Chapter 5 details the trap's configuration and operation, including the processes for catching, cooling, and maintaining a stable antiproton cloud over extended durations. Through the work conducted in this project, routine and reliable operation of the Reservoir trap was established, leading to an unprecedented reduction in antiproton consumption to as few as one particle per two months. This exceptional efficiency not only extends the feasibility of prolonged measurement campaigns but also opens new possibilities for experiments involving extremely rare antimatter species, such as antihydrogen molecular ions.

Among the most notable outcomes of this research is the successful demonstration of continuous antiproton trapping and monitoring for more than 560 days – a new world record for baryonic antimatter confinement. This achievement enables a more than fivefold improvement in the direct lower bound on the antiproton lifetime. Chapter 6 presents the methodologies used to verify the integrity of long-term storage and discusses the statistical framework that supports the new limit, marking a significant milestone in the precision study of antimatter.

The results presented in this work underscore the vital role of technical innovation in advancing the frontiers of experimental physics. The developed systems and procedures not only strengthen the capabilities of the BASE experiment but also lay the groundwork for future investigations of CPT symmetry and the fundamental structure of the Standard Model. As the BASE experiment continues to operate with the antiproton cloud caught

in October 2023, the contributions of this thesis remain integral to its ongoing and future successes.

Chapter 2

Theoretical background

2.1 The Penning trap

To carry out high-precision measurements of fundamental properties of charged particles, it is crucial to trap them and detect them non-destructively. However, according to Earnshaw's theorem [64], a stable equilibrium for a charged particle in space cannot be achieved using only electrostatic fields. This limitation led to two key developments in ion trapping: the use of oscillating electric fields, known as Paul traps [65], and the superposition of a static electric and magnetic field, resulting in the Penning trap, first realized experimentally by Hans Dehmelt in the 1950s [66] and later by others.

Penning traps have since become instrumental in numerous milestone experiments in the field of low-energy precision physics [46, 50, 56, 67–69] due to their conceptually pure structure and the ability to store individual ions for long periods, allowing detailed studies. The fundamentals of Penning traps and essential experiments have been reviewed among others in [70–75].

The following sections will explain the motion of a trapped particle and the systematic effects found in Penning traps, such as in the BASE experiment.

2.1.1 The ideal Penning trap

The concept of a Penning trap is based on the ideal assumption of a harmonic quadrupole potential Φ and a homogeneous magnetic field $\vec{B}$. This section describes the dynamics of a particle in a Penning trap and follows closely [70, 76].

In a homogeneous magnetic field $\vec{B}$, pointing in the axial z-direction, a particle with mass m and charge q experiences the Lorentz force $\vec{F_L}$ and starts oscillating with the

cyclotron frequency

$$\omega_{\mathrm{c}} = \frac{q}{m}B, \tag{2.1}$$

which scales with the strength of the magnetic field $B = |\vec{B}|$. For a particle with spin, the spin starts precessing around the magnetic field with the Larmor frequency

$$\omega_{\mathrm{L}} = \frac{g}{2}\frac{q}{m}B. \tag{2.2}$$

Adding the electric potential

$$\Phi(z,\rho) = C_2 V_{\mathrm{r}}\left(z^2 - \frac{\rho^2}{2}\right), \tag{2.3}$$

where C_2 is a characteristic trap parameter defined by the trap geometry, V_{r} denotes the trapping voltage, and $\rho^2 = x^2 + y^2$, modifies the Lorentz force $\vec{F_L}$ experienced by the particle

$$\vec{F_L} = q(-\nabla\Phi + \dot{\vec{r}} \times \vec{B}) \tag{2.4}$$

and leads to the equations of motion of the particle:

$$\begin{pmatrix} \ddot{x} - \dot{y}qB/m - qV_{\mathrm{r}}C_2/mx \\ \ddot{y} + \dot{x}qB/m - qV_{\mathrm{r}}C_2/my \\ \ddot{z} + 2qV_{\mathrm{r}}C_2/mz \end{pmatrix} = \begin{pmatrix} \ddot{x} - \dot{y}\omega_{\mathrm{c}} - (\omega_{\mathrm{z}}^2/2)x \\ \ddot{y} + \dot{x}\omega_{\mathrm{c}} - (\omega_{\mathrm{z}}^2/2)y \\ \ddot{z} + \omega_{\mathrm{z}}^2 z \end{pmatrix} = \begin{pmatrix} 0 \\ 0 \\ 0 \end{pmatrix}. \tag{2.5}$$

The motion in z-direction can be identified as the motion of a harmonic oscillator, and we define the oscillation frequency in the axial direction as

$$\omega_{\mathrm{z}} = \sqrt{\frac{2qV_{\mathrm{r}}C_2}{m}}. \tag{2.6}$$

To find a solution for the coupled radial modes in x- and y-direction, we introduce the complex variable $u = x + iy$ and get

$$\ddot{u} + i\omega_{\mathrm{c}}\dot{u} - \frac{\omega_{\mathrm{z}}^2}{2}u = 0. \tag{2.7}$$

Solving with the ansatz $u(t) = \exp(-i\omega t)$ leads us to

$$\omega^2 - \omega_{\mathrm{c}}\omega + \frac{\omega_{\mathrm{z}}^2}{2} = 0, \tag{2.8}$$

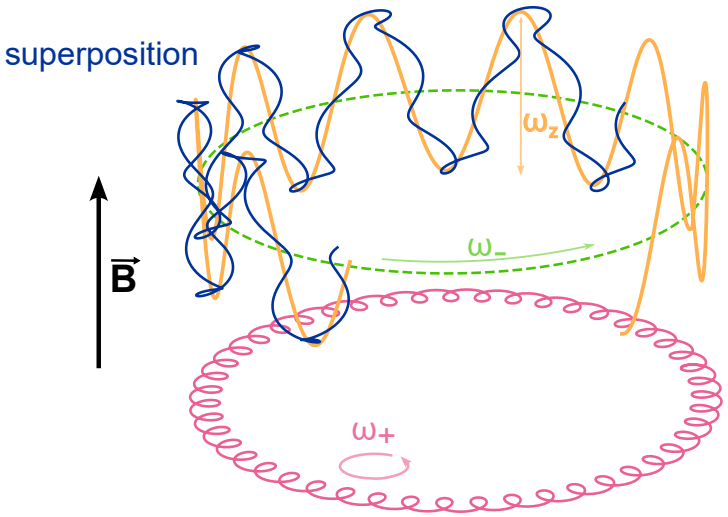

Figure 2.1: Trajectory of a negatively charged particle in a Penning trap (blue). The three eigenmotions ω_- (dashed green line), ω_z (yellow), and ω_+ (pink) superimpose into the trajectory of a particle in a Penning trap, depicted in blue. Both radial motions are projected in pink on the bottom.

which gives us for ω the two solutions

$$\omega_\pm = \frac{\omega_c}{2} \pm \sqrt{\left(\frac{\omega_c}{2}\right)^2 - \frac{\omega_z^2}{2}}. \tag{2.9}$$

ω_+ is called the modified cyclotron frequency and ω_- the magnetron frequency of the particle. Figure 2.1 shows the trajectory of a negatively charged particle in a Penning trap. It oscillates in z-direction, superimposed by two circular motions, the modified cyclotron and magnetron motion, in the x-y-plane. Typical proton/antiproton frequencies in BASE are $\nu_+ \approx 29.65$ MHz, $\nu_z \approx 636\,\text{kHz}$, and $\nu_- \approx 6800\,\text{Hz}$, following the hierarchy

$$\nu_+ \gg \nu_z \gg \nu_-. \tag{2.10}$$

Looking at Equation (2.9), the discriminant has to be real and larger than zero, so that the motion is stable. Therefore,

$$2\omega_z^2 < \omega_c^2 \tag{2.11}$$

is the condition for a stable motion of a particle in a Penning trap. If this criterion is not fulfilled, the electrostatic force pulling radially outwards is stronger than the magnetic confinement, resulting in particle loss. In our case, it is used, for example, for cleaning the

trap from unwanted ions, as the criterion is dependent on the q/m-ratio of the trapped ion, which is especially useful when the wanted species are (anti)protons (more details in Chapter 5.3).

The free cyclotron frequency ω_c is obtained by quadratically summing the three eigenfrequencies, following the Brown–Gabrielse invariance theorem [77]:

$$\omega_c^2 = \omega_+^2 + \omega_z^2 + \omega_-^2. \tag{2.12}$$

This theorem is especially important, as it is also valid under elliptical trap imperfections on misalignment of the electric and the magnetic field axis [70, 77].

An often-used estimate for the magnetron frequency is given by [70]

$$\omega_- \approx \frac{\omega_z^2}{2\omega_+}, \tag{2.13}$$

resulting from the fact that the magnetron frequency is much smaller than the cyclotron and axial frequency (see Equation (2.10)).

Each of the three eigenmodes has a related energy E_i. For the axial mode, the energy E_z is given by

$$E_z = \frac{1}{2} m\omega_z^2 z^2 = m\omega_z^2 \bar{z}^2, \tag{2.14}$$

where z is the maximum axial excitation and $\bar{z}$ the RMS amplitude. For the radial modes, the respective energy is given by their kinetic and potential energy. For the magnetron energy E_- the potential term prevails

$$E_- = \frac{1}{2} m\omega_-^2 \rho_-^2 - \frac{1}{4} m\omega_z^2 \rho_-^2 \approx -\frac{1}{4} m\omega_z^2 \rho_-^2, \tag{2.15}$$

and for the cyclotron energy E_+ the kinetic term is dominant

$$E_+ = \frac{1}{2} m\omega_+^2 \rho_+^2 - \frac{1}{4} m\omega_z^2 \rho_+^2 \approx \frac{1}{2} m\omega_+^2 \rho_+^2, \tag{2.16}$$

with ρ_i being the respective radii of the radial modes. Figure 2.2 depicts the energy levels in a Penning trap, here not drawn to scale and without considering the spin of the trapped particle. It should be noted that the energy of the magnetron mode E_- is negative and therefore metastable, as removing energy increases the magnetron radius ρ_-. An increasing magnetron radius would ultimately lead to particle loss when the particle

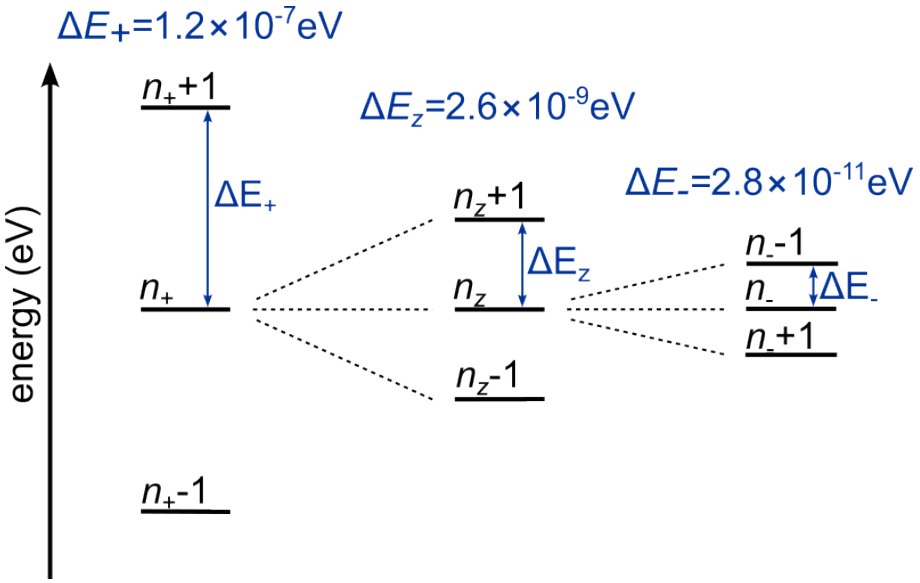

Figure 2.2: Energy levels of the trapped particle's eigenmotion in the BASE Precision trap, not drawn to scale. The metastable magnetron motion lowers the total energy with increasing quantum number n_-.

reaches the trap electrodes. Assuming radiation damping as the only loss mechanism, we can calculate the decay time [70]

$$\tau_- = \frac{1}{\gamma_-} = \left[\frac{1}{4\pi\varepsilon_0}\frac{4q^2}{3mc^3}\frac{\omega_-^3}{\omega_+ - \omega_-}\right]^{-1} \approx 1\times10^{22}\,\mathrm{s} \approx 3\times10^{14}\,\mathrm{yr}. \tag{2.17}$$

The decay time τ_- is therefore so long that it is not relevant on the timescales of our experiments.
When a particle is coupled to a thermal reservoir, the average mode energies E_i are related to the effective temperatures by

$$\langle E_z\rangle = k_\mathrm{B}T_z, \qquad \langle E_-\rangle = k_\mathrm{B}T_-, \qquad \langle E_+\rangle = k_\mathrm{B}T_+. \tag{2.18}$$

Although a temperature can only be assigned to an ensemble of particles, in this thesis, a particle's temperature refers to the effective temperature calculated from its energy eigenstates:

$$T_i = \frac{\langle E_i\rangle}{k_\mathrm{B}}. \tag{2.19}$$

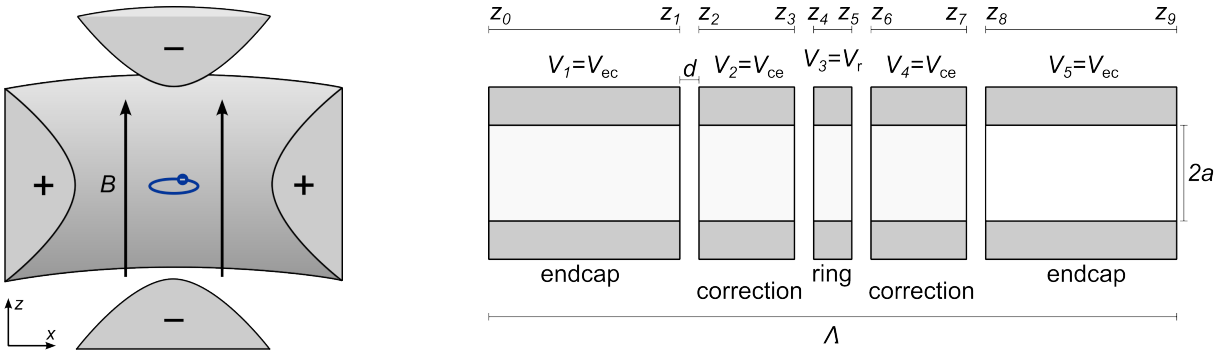

(a) Hyperbolic trap

(b) Cylindrical trap

Figure 2.3: a) Schematic drawing of a hyperbolic Penning trap. b) Schematic of a cylindrical Penning trap with five electrodes. The center electrode is the ring electrode where the trapping potential V_r is applied. The neighboring electrodes are the correction electrodes, enabling the increase of potential harmonicity. The outermost electrodes are the endcap electrodes. Compared to a) the improved trap access is shown for a Penning trap in cylindrical geometry compared to a hyperbolic Penning trap.

2.1.2 The real Penning trap

2.1.2.1 The cylindrical Penning trap

Up until now, we have discussed the behavior of a single particle in a perfect trap: we have considered an ideal electric quadrupole field and a perfectly homogeneous and stable magnetic field. However, this does not reflect the real experimental conditions. On the one hand, historically, hyperbolic-shaped electrodes were used to create an ideal quadrupole field (Figure 2.3 a)). Nowadays, mostly cylindrical Penning traps are in use [78]. They have the advantage of open end-caps, allowing laser access or loading particles via an accelerator. Moreover, cylindrical Penning traps can be stacked, resulting in multiple Penning traps in one experiment and allowing the transport of ions between the traps. Additionally, the manufacturing precision of cylindrical electrodes is much higher than that of hyperbolic electrodes. Figure 2.3 b)) shows a schematic of a cylindrical 5-pole trap. As the name suggests, it consists of five electrodes, which have different functions. In the center is the ring electrode, where the trapping potential V_r is applied. Adjoining it are the correction electrodes. Their function is to adjust the potential harmonicity. The outermost electrodes are called endcap electrodes, which are normally grounded but can be used to correct electric trap imperfections.

The potential of the trap can be analytically calculated by solving the Laplace equation in free space, which can be found in [79]. Here only the main points will be stated; for

more details, the reader is referred to [79].
The potential on axis can be expanded in the power of the coordinates z^j:

$$\Phi(0,z) = V_\mathrm{r} \sum_{j=0}^{n} C_j z^j, \tag{2.20}$$

where the coefficients for a five-pole trap are defined by [79]

$$C_j = \frac{1}{j!\Lambda V_\mathrm{r}} \sum_{n=1}^{\infty} \left[\frac{V_1 \cos(k_n z_0) - V_5 \cos(k_n \Lambda)}{k_n} + \sum_{i=2}^{5} \frac{V_i - V_{i-1}}{k_n^2 d} (\sin(k_n z_{2i}) - \sin(k_n z_{2i-1})) \right] \times \frac{(n\pi/\Lambda)^j}{I_0(k_n a)} \sin(\frac{\pi}{2}(n+j)). \tag{2.21}$$

In Equation (2.21) the geometry of the trap is reflected in the following variables: the trap length Λ, $k_n = n\pi/\Lambda$, the spacing between two electrodes d, and the inner radius of the electrodes a. z_{2i} gives the start coordinate of the $(i+1)$th electrode and z_{2i-1} the end coordinate of the ith electrode, I_0 describes the Bessel function of first kind. The applied voltages on the different electrodes are denoted by V_i. Going from the central electrode outwards: V_3 corresponds to the ring voltage V_r, V_2, and V_4 are the voltages applied on the correction electrodes. They are normally given by $V_{2/4} = V_\mathrm{r} \times \mathrm{TR}$, where TR is called the *tuning ratio*. The voltages on the endcap electrodes are described by V_1 and V_5 and are normally grounded. Assuming a symmetrical potential in z-direction, odd C_j coefficients disappear.

For grounded endcap-electrodes and voltages applied on the correction electrodes defined by $V_\mathrm{ce} = V_\mathrm{r} \times \mathrm{TR}$, the C_j coefficients can be expressed the following [79]:

$$C_j = D_j \times \mathrm{TR} + E_j, \tag{2.22}$$

where D_j and E_j are defined by the trap geometry. When designing a trap, the free parameters are the trap radius and the length of the ring and correction electrodes. These parameters can be chosen such that the axial frequency of the particle doesn't change when changing the voltages on the correction electrodes, i.e., changing the TR, so $D_2 = 0$. This is called *orthogonality*. Moreover, it is desirable to have both C_4 and C_6 tuned to zero, as they induce unwanted frequency shift (see Section 2.1.2.2), which is called a *compensated* Penning trap.

2.1.2.2 Trap anharmonicities and energy-dependent frequency shifts

The axial potential is described by Equation (2.20) with the coefficients C_j (Equation (2.21)), where higher-order terms characterize trap imperfections. Due to symmetry reasons, odd C_j coefficients vanish in an ideal experiment, but in reality, they can be present, caused by patch potentials, manufacturing imperfections, and current leaks. This can be compensated by applying offset voltages on the correction electrodes. Terms with even coefficients, however, induce systematic frequency shifts, which have to be considered. The equation of motion in axial direction is a generalized Duffing equation [79, 80]

$$\ddot{z} = -\frac{q}{m}\partial_z\left(V_\mathrm{r}\sum_{j=0}^{n} C_j z^j\right) = -\frac{2qC_2V_\mathrm{r}}{m}\left(z + \frac{2C_4}{C_2}z^3 + \frac{3C_6}{C_2}z^5 + \dots\right) = \omega_\mathrm{z}^2\left(z + \frac{2C_4}{C_2}z^3 + \dots\right). \tag{2.23}$$

Equivalent to the electric potential, the magnetic field can also be expanded in z-direction, with the coefficients B_j, which also introduce systematic frequency shifts in the eigenfrequencies of the particle.

$$B(0,z) = \sum_{j=0}^{\infty} B_j z^j. \tag{2.24}$$

The invariance theorem, fundamental for high-precision measurements in Penning traps, is strictly valid under the assumption of a perfectly homogeneous magnetic field and an ideal electrostatic quadrupole potential. It remains robust, however, with respect to a misalignment between the magnetic field and the trap's electrostatic axis, as well as to small elliptic distortions of the quadrupole potential. Any deviation beyond these tolerances – such as significant magnetic field inhomogeneities or anharmonicities in the trapping potential –introduces shifts in the measured cyclotron frequency of the trapped particle and results in systematic frequency errors.

To illustrate one such effect, consider the relativistic shift of the cyclotron frequency. Due to special relativity, the cyclotron frequency changes according to

$$\frac{\Delta\omega_\mathrm{c}}{\omega_\mathrm{c}} = -\frac{E_+}{mc^2}. \tag{2.25}$$

In the BASE experiment, an antiproton trapped with an energy of 1 eV would exhibit a frequency shift of about 10^{-9}, or approximately $\Delta\nu_\mathrm{c} = \Delta\omega_\mathrm{c}/2\pi \approx 30\,\mathrm{mHz}$, compared to a particle at rest. When aiming for sub-part-per-billion (p.p.b.) precision, it becomes

essential to account for all possible effects – both technical and physical – that can lead to frequency shifts.

These frequency shifts arise from two main categories: trap-related imperfections, like anharmonicities in the electrostatic potential and inhomogeneities in the magnetic field, and intrinsic physical effects, like relativistic frequency shifts and frequency shifts due to the particle's interaction with its image charge, which break the cylindrical symmetry of the trap.

All these effects cause energy-dependent deviations in the measured frequencies. These have been calculated in [70, 71, 81] and a summary is presented in [70, 82]:

$$\begin{pmatrix} \Delta\omega_+/\omega_+ \\ \Delta\omega_\mathrm{z}/\omega_\mathrm{z} \\ \Delta\omega_-/\omega_- \\ \Delta\omega_\mathrm{L}/\omega_\mathrm{L} \end{pmatrix} = (\mathcal{M}_{C4} + \mathcal{M}_{B2}) \begin{pmatrix} E_+ \\ E_\mathrm{z} \\ E_- \end{pmatrix} + \mathcal{M}_{C6} \begin{pmatrix} E_+^2 \\ E_\mathrm{z}^2 \\ E_-^2 \\ E_+E_\mathrm{z} \\ E_+E_- \\ E_\mathrm{z}E_- \end{pmatrix} + \dots \tag{2.26}$$

with the corresponding matrices given by

$$\mathcal{M}_{C4} = \frac{1}{qV_\mathrm{r}}\frac{C_4}{C_2^2}\begin{pmatrix} \frac{3}{4}\Omega^4 & -\frac{3}{2}\Omega^2 & -3\Omega^2 \\ -\frac{3}{2}\Omega^2 & \frac{3}{4} & 3 \\ -3\Omega^2 & 3 & 3 \\ 0 & 0 & 0 \end{pmatrix}, \quad \mathcal{M}_{B2} = \frac{1}{m\omega_\mathrm{z}^2}\frac{B_2}{B_0}\begin{pmatrix} -\Omega^2 & 1 & 2 \\ 1 & 0 & -1 \\ 2 & -1 & -2 \\ -\Omega^2 & 1 & 2 \end{pmatrix},$$

$$\mathcal{M}_{C6} = \frac{1}{q^2V_\mathrm{r}^2}\frac{C_6}{C_2^3}\begin{pmatrix} -\frac{15}{16}\Omega^6 & -\frac{45}{16}\Omega^2 & -\frac{45}{4}\Omega^2 & \frac{45}{8}\Omega^4 & \frac{45}{4}\Omega^4 & -\frac{45}{2}\Omega^2 \\ \frac{45}{16}\Omega^4 & \frac{15}{16} & \frac{45}{4} & -\frac{45}{8}\Omega^2 & -\frac{45}{2}\Omega^2 & \frac{45}{4} \\ \frac{45}{8}\Omega^4 & \frac{45}{8} & \frac{15}{2} & -\frac{45}{2}\Omega^2 & -\frac{45}{2}\Omega^2 & \frac{45}{2} \\ 0 & 0 & 0 & 0 & 0 & 0 \end{pmatrix}, \tag{2.27}$$

with $\Omega = \omega_\mathrm{z}/\omega_+$ and assuming the magnetron energy to be negative $E_- < 0$. It is noted that the higher-order electric imperfection does not affect the Larmor frequency.
Moreover, the linear magnetic field gradient B_1 also introduces shifts in the cyclotron frequency ω_+. The different equilibrium positions of the particle in the trap lead to

slightly different probed magnetic field [83]

$$\frac{\Delta\omega_+}{\omega_+} = -\frac{1}{m\omega_\mathrm{z}}\left(\frac{B_1}{B_0}\right)^2 (E_+ + |E_-|). \tag{2.28}$$

As mentioned above, there are also relativistic shifts [70], which arise without the presence of electric or magnetic inhomogeneities

$$\begin{pmatrix} \Delta\omega_+/\omega_+ \\ \Delta\omega_\mathrm{z}/\omega_\mathrm{z} \\ \Delta\omega_-/\omega_- \\ \Delta\omega_\mathrm{L}/\omega_\mathrm{L} \end{pmatrix} = -\frac{1}{mc^2} \begin{pmatrix} 1 & \frac{1}{2} & -\Omega^2 \\ \frac{1}{2} & \frac{3}{8} & -\frac{\Omega^2}{4} \\ -\Omega^2 & -\frac{\Omega^2}{4} & \frac{\Omega^4}{4} \\ \frac{9}{2} & \frac{1}{2} & -\Omega^2 \end{pmatrix} \begin{pmatrix} E_+ \\ E_\mathrm{z} \\ E_- \end{pmatrix}, \tag{2.29}$$

with the speed of light c.

Moreover, the oscillating trapped particle also induces image charges in the surrounding trap electrode. On the one hand, these are essential for particle detection (Section 2.2); on the other hand, they also generate an electric field acting back on the particle, causing a systematic frequency shift [84]:

$$\frac{\Delta\nu_\mathrm{c}}{\nu_\mathrm{c}} \approx \frac{m}{4\pi\varepsilon_0 B_0^2 a^3}, \tag{2.30}$$

where m is the particle mass, ε_0 the vacuum permittivity and a the trap radius. In the BASE Precision trap, this shift is $\approx -4 \times 10^{-11}$.

All of the above-listed frequency shifts influence the measurements conducted in BASE. Most of them depend on the energy/temperature of the different eigenmodes of the particle. Therefore, it is essential to reduce the energy in the radial modes to a minimum; the temperature of the axial mode is determined by the temperature of the detection system (see Section 2.2.1). In addition, the precise knowledge of the mode energies is crucial for the determination of the frequency shifts and the correction of the data.

Shifts induced by the electrostatic coefficients C_4 and C_6 are small by design of the trap and can, in the ideal case, be completely tuned out. For the compensation of higher order terms like C_8, additional correction electrodes have to be added [85]. The shifts induced by the magnetic field inhomogeneity B_2, on the other hand, add the highest or second-highest in systematic uncertainty for the respective measurement [55, 56]. Therefore, it is important to reduce the B_2 component of the magnetic field as much as possible

systematic effect	$\Delta\nu_c/\nu_c$ (p.p.t)
relativistic	35
image charge	44
B_1	18
B_2	340
B_1 optimum	6
B_2 optimum	< 1

Table 2.1: Typical systematic cyclotron frequency shifts $\Delta\nu_c/\nu_c$ in the BASE Precision trap. The B_1 and B_2 shift origin from the respective residual magnetic field inhomogeneities. Both components can be tuned using a superconducting shimming coil system at the position of the Precision trap. With this, both components can be minimized and the respective frequency shift are given as optimum value. For the optimum B_2 shift an upper limit is given, as the B_2 component can be fully tuned out within error bars.

for cyclotron frequency measurements, for example, by implementing a superconducting shimming coil system [86]. On the other hand, a high B_2 is crucial for the determination of the Larmor frequency, which will be discussed in greater detail in Section 2.3.

Typical frequency shifts in the BASE Precision trap induced by systematic effects are given in Table 2.1.

2.2 Particle detection and frequency measurements

2.2.1 Particle detector interaction

Originally described by Wineland and Dehmelt in 1975 [68], the widely used non-destructive detection method for Penning traps is summarized in [79] and reviewed in this section. For BASE, where exotic antiprotons are studied, such methods are essential for high-precision studies. They permit operation with particle consumption rates of approximately one particle every two months and uniquely enable continued experimentation during accelerator shutdown periods, which is essential for the high-precision studies reported in this thesis. Particles moving in a Penning trap induce image currents in the trap electrodes:

$$I_p = \frac{q}{D_{\text{eff}}}\dot{\rho}_i, \tag{2.31}$$

where q is the charge of the particle, D_{eff} the effective electrode distance, describing the strength of the coupling between particle and electrode, and the coordinate ρ_i, where i

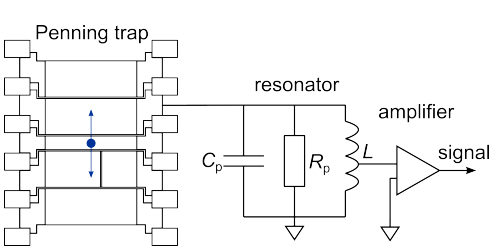

(a) Particle in trap with resonator

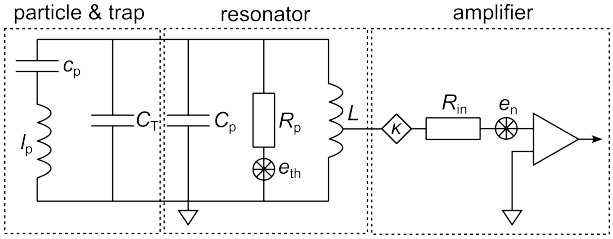

(b) Equivalent circuit particle in a trap with resonator

Figure 2.4: a) A particle oscillating in a Penning trap is inducing image currents in the trap electrodes. A resonant tank circuit is used to pick up the signal. In the next stage, the signal is getting amplified. b) Detailed equivalent circuit of a moving particle in a trap. The particle can be presented as a series LC-circuit. The parasitic capacitance of the trap C_T and the resonator C_{res} are in parallel to the particles equivalent circuit. The equivalent parallel resonator R_p has a voltage noise source e_{th}. The amplifier with input resistance R_{in} and the input voltage noise e_n is coupled to the resonator with the coupling factor κ.

can be one of the three eigenmodes z, +, −. These image currents are on the order of fA, so to be able to detect the signal, a large resistance is needed. This is realized with a coil with inductance L connected to one trap electrode, which compensates the parasitic capacitance C_p of the trap and appears like a parallel resistance R_p on resonance. This resonant circuit is also called *resonator* or *detector* within this thesis (see Figure 2.4 a)). The motion of the particle in the trap interacting with the resonator can be described as a damped harmonic oscillator

$$\ddot{z} + \gamma\dot{z} + \omega_\mathrm{z}^2 z = 0, \tag{2.32}$$

where γ is the damping constant of the system. Multiplying Equation (2.32) by $m\dot{z}$ and integrating it in the time domain gives

$$\frac{1}{2}m\dot{z}^2 + \frac{1}{2}m\omega_\mathrm{z}^2 z^2 = -\int m\gamma\dot{z}^2 dt. \tag{2.33}$$

The left-hand side of the equation gives us now the total energy of the particle, while the right-hand side reflects the loss due to dissipation with the detection system. This can be connected to the power P consumed by the resistance R_p when the image current I_p flows through it:

$$P = U_\mathrm{p} I_\mathrm{p} = R_\mathrm{p} I_\mathrm{p}^2 = m\gamma\dot{z}^2. \tag{2.34}$$

Utilizing Equation (2.31), we can express the damping constant by

$$\gamma = \frac{R_\mathrm{p}}{m}\left(\frac{q}{D_\mathrm{eff}}\right)^2 \tag{2.35}$$

and identifying the time constant τ of the particle-resonator interaction as

$$\tau = \frac{m}{R_\mathrm{p}}\left(\frac{D_\mathrm{eff}}{q}\right)^2, \tag{2.36}$$

also called *cooling time constant* in the context of resistive cooling of the particle through the detector.
Having another look at Equation (2.32), we can use Equation (2.31) and the damping constant γ to write the equation of motion in terms of current:

$$m\frac{D_\mathrm{eff}^2}{q^2}\dot{I}_\mathrm{p} + R_\mathrm{p}I_\mathrm{p} + \omega_\mathrm{z}^2 m\frac{D_\mathrm{eff}^2}{q^2}\int I_\mathrm{p}dt = 0. \tag{2.37}$$

Establishing $l_\mathrm{p} = m\frac{D_\mathrm{eff}^2}{q^2}$ and $c_\mathrm{p} = \frac{1}{m\omega_\mathrm{z}^2}\frac{q^2}{D_\mathrm{eff}^2}$, we can rewrite Equation (2.37) as

$$l_\mathrm{p}\dot{I}_\mathrm{p} + R_\mathrm{p}I_\mathrm{p} + \frac{1}{c_\mathrm{p}}\int I_\mathrm{p}dt = 0, \tag{2.38}$$

which represents the differential equation that describes the time dynamics of a series-tuned circuit. Such a circuit is also called a "notch" circuit because the impedance at its resonance frequency $\omega = 1/\sqrt{LC}$ vanishes and the signal goes directly to ground – it is shorting the signal at its resonance frequency [87], often also described as shorting the thermal noise floor. Figure 2.4 B shows an equivalent circuit of the particle-resonator system, substituting the particle by a series LC-circuit. The impedance of the particle Z_p is expressed by

$$Z_\mathrm{p}(\omega) = Z_{l_\mathrm{p}} + Z_{c_\mathrm{p}} = i\omega l_\mathrm{p} + \frac{1}{i\omega c_\mathrm{p}}. \tag{2.39}$$

Looking at Figure 2.4, the impedance of the resonator Z_R has also to be taken into account. Above we approximated $Z_\mathrm{R} \approx R_\mathrm{p}$, which is true when the axial frequency

equals the resonator frequency $\omega_z = \omega_R$. The full resonator impedance Z_R is

$$Z_R = \left(\frac{1}{R_p} + \frac{1}{i\omega L} + i\omega C\right)^{-1} \tag{2.40}$$

$$= \left(\frac{1}{R_p} + i\left(\frac{\omega_R^2 - \omega^2}{\omega\omega_R^2 L}\right)\right)^{-1}, \tag{2.41}$$

where $\omega_R = 1/\sqrt{LC}$ is the resonance frequency of the detector. Taking the real part gives us

$$\mathrm{Re}(Z_R) = \frac{R_p}{1 + R_p^2 \frac{(\omega_R^2-\omega)^2}{(\omega\omega_R^2 L)^2}} = \frac{R_p(\omega\omega_R^2 L)^2}{(\omega\omega_R^2 L)^2 + R_p^2(\omega_R^2 - \omega)^2}, \tag{2.42}$$

which is describing a pseudo-squared Lorentzian lineshape. Note that in the resonant case ($\omega = \omega_R$) the real part of the impedance is independent of ω and equals to the effective parallel resistance R_p. It can also be expressed by

$$R_p = Q\omega_R L, \tag{2.43}$$

where Q is called the *quality-factor* or simply *Q-value* of the resonator. It is defined as the resonance frequency ω_R divided by the full width at half maximum (FWHM) or in logarithmic power units the 3 dB-width $\Delta\omega$

$$Q = \frac{\omega_R}{\Delta\omega}. \tag{2.44}$$

In our experiment R_p is in the order of 100 MΩ - 300 MΩ [88] for axial and around 300 kΩ - 500 kΩ for the cyclotron resonators [89, 90], the loaded Q-value for the axial resonator is around 25000.

Using Kirchhoff's law, the total impedance of the particle-resonator system (as seen in Figure 2.4 b), is

$$Z_{tot} = \left(\frac{1}{Z_p} + \frac{1}{Z_R}\right)^{-1} = \left(\frac{1}{R_p} + \frac{1}{i\omega L} + i\omega C + \frac{1}{i\omega l_p + \frac{1}{i\omega c_p}}\right)^{-1}. \tag{2.45}$$

With the above-mentioned definitions of R_p, γ, l_p, c_p and the resonance frequency of the detector $\omega_R = 1/\sqrt{LC}$, the total impedance of the coupled particle-detector system can

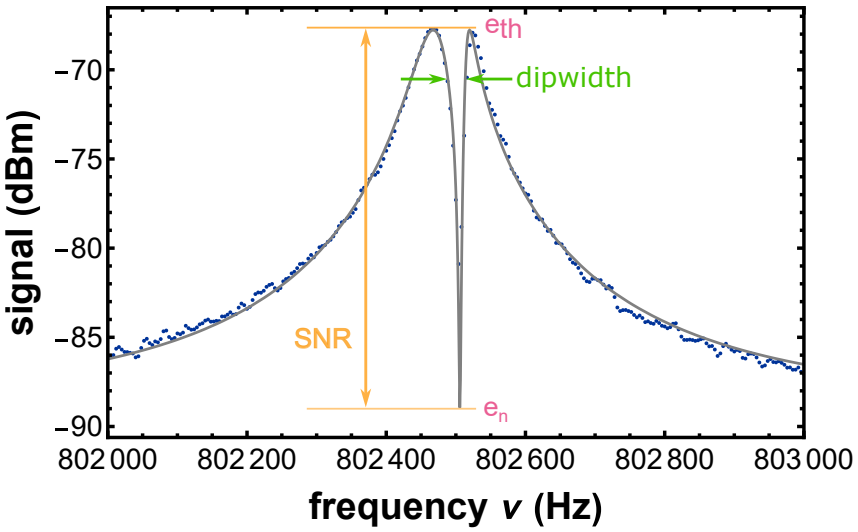

Figure 2.5: Example of a dip spectrum from the reservoir trap, with around 20 particles trapped. Seen here is the resonator with particles shorting the thermal noise floor resulting in a dip feature. The dip width $\delta\nu$ and the SNR are important characteristics for the dip frequency measurements.

be written as

$$Z_{\mathrm{tot}} = \frac{R_{\mathrm{p}}(\omega^2-\omega_{\mathrm{z}}^2)^2}{(\omega^2-\omega_{\mathrm{z}}^2)^2+\left[\frac{Q}{\omega\omega_{\mathrm{R}}}(\omega_{\mathrm{R}}^2-\omega^2)(\omega^2-\omega_{\mathrm{z}}^2)+\gamma\omega\right]^2} + \frac{i\left[\frac{QR_{\mathrm{p}}}{\omega\omega_{\mathrm{R}}}(\omega_{\mathrm{R}}^2-\omega^2)(\omega^2-\omega_{\mathrm{z}}^2)^2+R_{\mathrm{p}}\gamma\omega(\omega^2-\omega_{\mathrm{z}}^2)\right]}{(\omega^2-\omega_{\mathrm{z}}^2)^2+\left[\frac{Q}{\omega\omega_{\mathrm{R}}}(\omega_{\mathrm{R}}^2-\omega^2)(\omega^2-\omega_{\mathrm{z}}^2)+\gamma\omega\right]^2}. \tag{2.46}$$

The lineshape of the particle at resonance with the detector is given by the real part of the impedance of the total system:

$$\mathrm{Re}(Z_{\mathrm{tot}}) = \frac{R_{\mathrm{p}}(\omega^2-\omega_{\mathrm{z}}^2)^2}{(\omega^2-\omega_{\mathrm{z}}^2)^2+\left[\frac{Q}{\omega\omega_{\mathrm{R}}}(\omega_{\mathrm{R}}^2-\omega^2)(\omega^2-\omega_{\mathrm{z}}^2)+\gamma\omega\right]^2}. \tag{2.47}$$

Equation (2.47) visualizes again the behavior of a series LC- circuit: For frequencies $|\omega - \omega_{\mathrm{z}}| \gg 0$ the impedance is given by R_{p} and for $\omega = \omega_{\mathrm{z}}$ the real part of the impedance is zero. This gives us a so-called dip in the Lorentzian lineshape of the resonator spectrum at the particle frequency ω_{z}, which is displayed in Figure 2.5. The full width at

half maximum (FWHM) of the dip is

$$\delta\nu_z = \frac{1}{2\pi}\gamma = \frac{1}{2\pi}\frac{R_p}{m}\frac{q^2}{D_{eff}^2}. \tag{2.48}$$

It was shown, that this equation also holds for a small number N of particles confined in a trap [68]:

$$\delta\nu_z(N) = \frac{N}{2\pi}\gamma = \frac{N}{2\pi}\frac{R_p}{m}\frac{q^2}{D_{eff}^2}. \tag{2.49}$$

This relation is essential when monitoring the content of our Reservoir trap, normally containing in the order of $10 - 300$ (anti)protons (see Chapter 6).
The dip feature can not only be described by its width $\delta\nu_z$, but also by its "depth", the so-called *signal-to-noise ratio* (SNR), typically between 20 dB - 30 dB. A spectrum as in Figure 2.5 is obtained by measuring the Johnson-Nyquist noise e_{th} [91, 92] over the total impedance Z_{tot}. It is defined as

$$e_{th} = \sqrt{4k_B T \mathrm{Re}(Z) B}, \tag{2.50}$$

where k_B is Boltzmann's constant, T the temperature of the system, and B the bandwidth, which is the detection bandwidth of the input of the spectrum analyzer that records the spectrum. With $\mathrm{Re}(Z(\omega_z = \omega_R)) = 0$, the noise at the dip frequency should also vanish completely. In reality, this is not the case, since in order to record the small signals, an amplifier is coupled to the resonator system, therefore having an input voltage noise source e_n, as can be seen in Figure 2.4 b). This input noise raises the overall noise floor of the system, making it impossible for the signal to fully drop to zero. The SNR of the particle is hence defined as the thermal noise of the detection system e_{th} incoherently added to the input noise of the amplifier, in reference to the noise floor e_n added by the amplifier. It has to be noted, however, that the thermal noise of the resonator is reduced due to the coupling of the amplifier with the detection system, which is quantified by the coupling constant κ as defined in [88]. The signal-to-noise ratio is defined as:

$$\mathrm{SNR} = \sqrt{\frac{(e_{th}\kappa)^2 + e_n^2}{e_n^2}}, \tag{2.51}$$

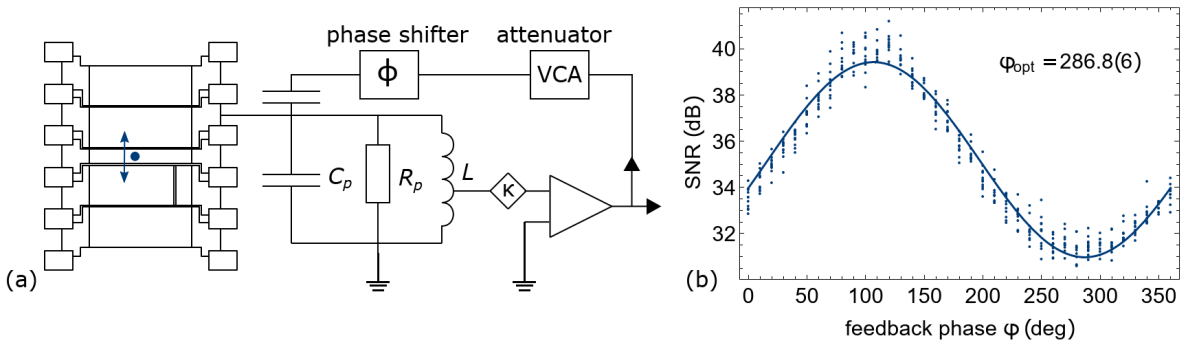

Figure 2.6: a) Schematic drawing of the feedback system. The detector signal is picked up, attenuated by the VCA, phase-shifted, and fed back to the pick-up electrode. The resonator consists of a resistance R_p, inductance L, and a parasitic capacitance C_p. κ is the inductive coupling factor between the resonator and the amplifier. b) SNR of the particle depending on the feedback phase. Maximum negative feedback is applied at φ_{opt}. Taken from [93].

and expressed in logarithmic power unit (dB), as we use in the laboratory:

$$\mathrm{SNR}_\mathrm{log} = \log\left(\frac{4k_\mathrm{B}TR_\mathrm{p}\kappa^2}{e_\mathrm{n}^2} + 1\right). \tag{2.52}$$

2.2.2 Active electronic feedback

Control of the temperature of the detection system employing active electronic feedback is crucial for advanced Penning trap systems that perform high-precision frequency measurements. On the one hand, the frequency scatter in the axial mode can be minimized by reducing the linewidth [94] of the particle dip, leading to a more precise frequency determination. This is essential, e.g., for the detection of single spin flips [95] as described in Section 2.3 and Chapter 4, without which the determination of the (anti)proton g-factor would not be possible. On the other hand, the energy of a particle in its respective mode E_i is determined by the detector's temperature T_z

$$E_i = \frac{\nu_i}{\nu_\mathrm{z}} T_\mathrm{z}, \tag{2.53}$$

assuming here that sideband-coupling (see in detail Section 2.2.3) is applied and the detector is oscillating at the axial frequency ν_z of the particle. From Equation (2.53) it is obvious, that the energy of the particle's eigenmodes E_i is reduced by reducing the temperature of the axial detection system leading to smaller systematic frequency shifts

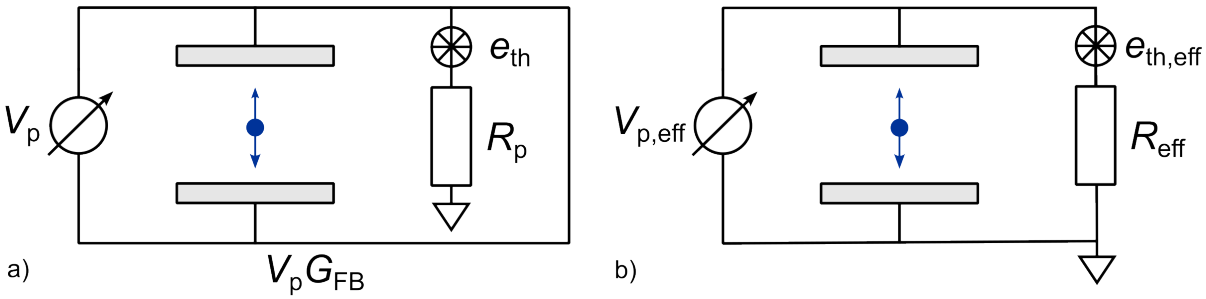

Figure 2.7: a) Schematic of a particle oscillating in a Penning trap with applied feedback. The signal of the detection system is fed back to the particle with a feedback gain G_{FB}, which modifies the applied voltage. b) Equivalent circuit to a) in the particle's view: Its motion can also be described by an effective parallel resistance R_{eff} and effective voltage $V_{\mathrm{p,eff}}$.

due to anharmonicities in the electrostatic and magnetic field and relativistic effects [70] (see Section 2.1.2.2). To minimize systematic shifts, negative active electronic feedback can be utilized and enables us, for example, to efficiently cool the magnetron mode of the trapped particle to an equivalent temperature lower than 10 mK. Moreover, it can be used to measure the temperature of the detection system T_{z}, which enters as one of the main systematic effects in the last antiproton g-factor measurement [56]. This makes the application of active electronic feedback cooling an essential part of measuring the proton and antiproton g-factor.

Figure 2.6 a) displays the electronic implementation of active electronic feedback. It can be applied by connecting a phase shifter and a voltage-controlled attenuator (VCA) to the detection system and feeding the phase-shifted signal back to the hot end of the detector. This leaves us with two tuneable parameters, the feedback gain G_{FB} and the feedback phase φ_{FB}. The feedback gain defines the strength of the feedback, which can be controlled by changing the control voltage of the VCA. The feedback phase φ_{FB} determines if positive or negative feedback is applied, which defines whether the detector is cooled or heated by its own signal. Figure 2.6 b) shows the change in SNR for changing feedback phase. Positive feedback is reached for the highest, and negative for the lowest SNR.
If the measured voltage drop $V_{\mathrm{p}} = I_{\mathrm{p}} R_{\mathrm{p}}$ is instantaneously fed back to the particle with the feedback gain G_{FB}, it influences the motion of the particle as in Figure 2.7 a). Figure 2.7 b) shows an equivalent representation for the particle. For it, the effect of feedback is the same as in Figure 2.7 a) with the effective resistance $R_{\mathrm{eff}}(T_{\mathrm{eff}})$ chosen to make the same potential variations V_{eff} as in Figure 2.7 a). So with

$$V_\mathrm{p} = I_\mathrm{p} R_\mathrm{p} \pm G_\mathrm{FB} I_\mathrm{p} R_\mathrm{p} \tag{2.54}$$

$$V_\mathrm{eff} = I_\mathrm{p} R_\mathrm{eff} \tag{2.55}$$

the effective resistance, which the particle sees when feedback is applied, is

$$R_\mathrm{eff} = R_\mathrm{p}(1 \pm G_\mathrm{FB}). \tag{2.56}$$

Making the same argument the effective temperature is

$$T_\mathrm{eff} = T_0(1 \pm G_\mathrm{FB}). \tag{2.57}$$

From Equation (2.48) we know that the dip width $\delta\nu_\mathrm{z}$ is changing with R_p

$$T_\mathrm{eff} = T_0 \frac{\delta\nu_\mathrm{z,FB}}{\delta\nu_\mathrm{z}}, \tag{2.58}$$

as well as the energy $E_\mathrm{z} = k_\mathrm{B} T_\mathrm{z}$ and the SNR. Figure 2.8 shows the effect of applied feedback on the lineshape of the resonator a) and the particle dip b), here for positive feedback. With increasing feedback strength, e.g. increasing VCA voltage, the Q-value of the resonator increases with increasing effective R_p c). In b) dip spectra for different feedback strengths are shown. It is visible, that the dip width and SNR increase with increasing positive feedback. The same in the reverse direction is visible for negative feedback.

2.2.3 Modecoupling and sideband technique

To measure the cyclotron and magnetron frequency of a particle, we use sideband-coupling [96] to couple one of the radial modes to the axial frequency. This is realized by irradiating a quadrupolar drive

$$\vec{E}_\mathrm{rf} = \mathrm{Re}(E_\mathrm{rf} \exp(i\omega_\mathrm{rf})(z\vec{e}_x + x\vec{e}_z) \tag{2.59}$$

at the frequency $\omega_\mathrm{rf} = \pm\omega_\pm \mp \omega_\mathrm{z}$ with the excitation amplitude E_rf into the trap. This transfers energy between the two modes with a Rabi frequency Ω_0

$$\Omega_0 = \frac{qE_\mathrm{rf}}{2m_p\sqrt{\omega_\pm \omega_\mathrm{z}}}. \tag{2.60}$$

In reality, we do not know the exact Rabi frequency, so we are irradiating a rf-frequency

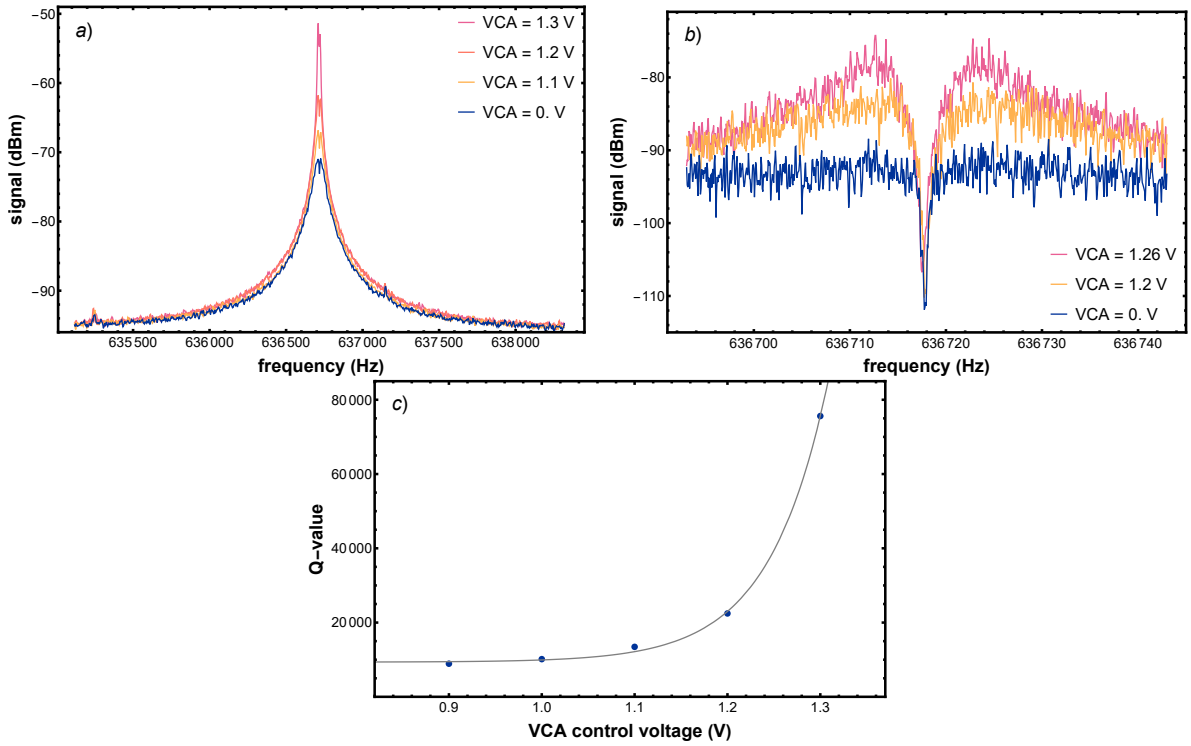

Figure 2.8: The effect of applied positive feedback on the resonator. The strength of the feedback increases with increasing VCA voltage. a) shows a broadband FFT spectrum of the resonator. b) the dip for different feedback strengths in a span of 50Hz. The stronger the feedback the larger the dip width. c) It is visible that the Q-value of the resonator is increasing with stronger positive feedback.

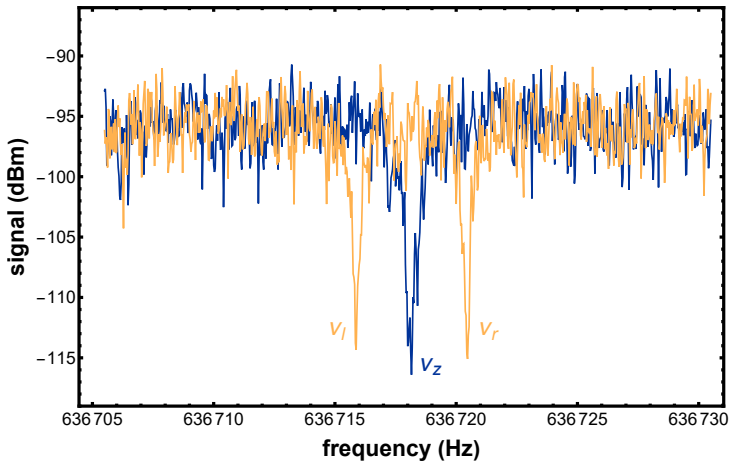

Figure 2.9: FFT spectra of a single dip (blue) and a double dip (yellow). The single dip corresponds to the axial frequency ν_z and the yellow dips to the left and right sideband with the frequencies ν_l and ν_r, respectively.

with a detuning δ: $\omega_{\mathrm{rf}} = \omega_{\mathrm{z}} \mp \omega_{\pm} + \delta$. This modifies the Rabi frequency to

$$\Omega' = \sqrt{\Omega_0^2 + \delta^2}. \tag{2.61}$$

Figure 2.9 shows the FFT spectrum without (blue) and during (yellow) irradiating the so-called sideband drive ω_{rf}. While the sideband drive is applied, a double dip emerges at the frequencies ω_l and ω_r for the left and right dip, respectively. For the cyclotron mode, these sidebands are at the frequencies

$$\omega_{l,+} = \omega_{\mathrm{z}} - \frac{\delta}{2} - \frac{\Omega'}{2} \quad \text{and} \quad \omega_{r,+} = \omega_{\mathrm{z}} - \frac{\delta}{2} + \frac{\Omega'}{2}, \tag{2.62}$$

and for the magnetron mode

$$\omega_{l,-} = \omega_{\mathrm{z}} + \frac{\delta}{2} - \frac{\Omega'}{2} \quad \text{and} \quad \omega_{r,-} = \omega_{\mathrm{z}} + \frac{\delta}{2} + \frac{\Omega'}{2}. \tag{2.63}$$

With the help of an independent measurement of ω_{z}, the radial frequencies $\omega_{\pm}$ can be calculated and the detuning cancels out. For the cyclotron frequency, this leads to

$$\omega_+ = \omega_{\mathrm{rf}} + \omega_l + \omega_r - \omega_{\mathrm{z}}, \tag{2.64}$$

and for the magnetron frequency to

$$\omega_{-} = \omega_{\mathrm{rf}} - \omega_l - \omega_r + \omega_{\mathrm{z}}. \tag{2.65}$$

The sideband technique is not only used for the determination of the radial frequencies but also to cool the radial modes. During the coupling, the axial mode is continuously thermalized by the detection system and exchanges energy with the coupled mode. The radial mode is sampling a Boltzmann distribution defined by the temperature T_z of the axial detection system with the mean energy of the modes

$$\langle E_{\pm} \rangle = \frac{\omega_{\pm}}{\omega_{\mathrm{z}}} k_{\mathrm{B}} T_z. \tag{2.66}$$

This process is from here on also referred to as *sideband-cooling*. Important to note is, that by measuring the cyclotron frequency using the sideband technique, the particle also thermalizes with the axial detection system, and the cyclotron energy is determined by Equation (2.66), defining systematic shifts of the particle (see Chapter 2.1.2.2). By applying feedback cooling (Chapter 2.2.2), the temperature of the detector can be reduced and with it the mode energies of the particle.

2.3 The continuous Stern-Gerlach effect

When a particle with spin is in a magnetic field, the spin starts precessing around the magnetic field with the Larmor frequency (Equation (2.2)). This can be expressed as

$$\frac{g}{2} = \frac{\omega_{\mathrm{L}}}{\omega_{\mathrm{c}}}, \tag{2.67}$$

and the g-factor is reminisced in the magnetic moment

$$\vec{\mu} = g \frac{q}{2m} \vec{S}. \tag{2.68}$$

So measuring the Larmor and free cyclotron frequency gives us access to the (anti)proton magnetic moment. The cyclotron frequency can be determined by measuring the three eigenfrequencies via image current detection and deploying the invariance theorem (Equation (2.12)). The Larmor frequency on the other hand, does not induce image currents (Section 2.2.1), so a different method for its determination has to be used, the *continuous*

Stern-Gerlach effect [97]. Here, a large magnetic inhomogeneity is introduced to the magnetic field in the Penning trap, which is also called a *magnetic bottle*. This couples the magnetic moment of the trapped particle to the axial motion, which results in a frequency shift $\Delta\omega_z$. This frequency shift is dependent on the magnetic moment and thus also on the spin state. The Larmor frequency is determined by irradiating a rf-drive around the expected Larmor frequency and the corresponding spin-flip probability is detected. From the resonance curve of the spin-flip probability for different drive frequencies, the Larmor frequency can be extracted.

The magnetic field with a quadratic inhomogeneity of the strength B_2 has the following form

$$\vec{B}(z,\rho) = B_0\vec{e_z} + B_2\left(\left(z^2 - \frac{\rho}{2}\right)\vec{e_z} + \rho z\vec{e_\rho}\right). \tag{2.69}$$

The coupling between the magnetic moment and the magnetic field with the potential energy $E_B = -\vec{\mu}\cdot\vec{B}$ leads to an additional force in the axial direction, resulting in the equation of motion:

$$\begin{aligned}\ddot{z} &= -\frac{q}{m}\frac{\partial\Phi_E(z,\rho)}{\partial z} - \frac{1}{m}\frac{\partial E_B(z,\rho)}{\partial z}\\ \ddot{z} &= -\left(\frac{2qC_2V_r}{m} + \frac{2\mu_z B_2}{m}\right)z,\end{aligned} \tag{2.70}$$

where $\Phi_E(z,\rho)$ is the electric potential (Equation (2.3)). From this, the axial frequency is extracted

$$\omega_z = \omega_{z,0}\sqrt{1 \pm \frac{2\mu_z B_2}{m\omega_{z,0}^2}} \approx \omega_{z,0} \pm \frac{\mu_z B_2}{m\omega_{z,0}}, \tag{2.71}$$

where

$$\Delta\omega_{z,SF} = \frac{2\mu_z B_2}{m\omega_z} \tag{2.72}$$

is the axial frequency difference between the two spin states. $\omega_{z,0}$ denotes the axial frequency without any inhomogeneities, determined purely by the quadrupole potential Φ_E.

Figure 2.10 shows the implementation and the effect of the continuous Stern-Gerlach effect. In a) the field lines of the magnetic bottle are shown, with the corresponding magnetic field in axial direction along the trap electrodes. Figure 2.10 b) denotes the changed electric potential due to the influence of the spin magnetic moment.
The magnetic moment $\vec{\mu}$ is not only composed of the spin magnetic moment $\vec{\mu}_S$, but also

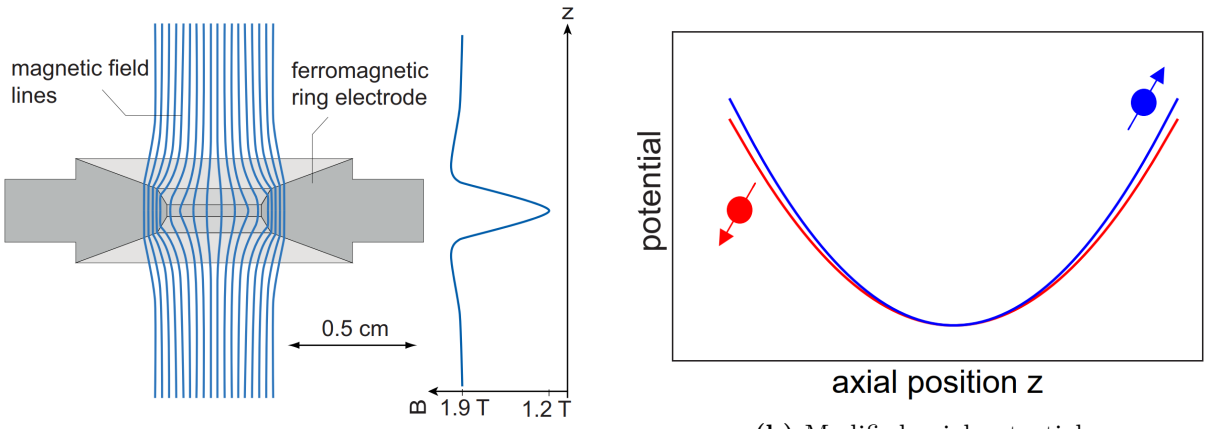

(a) Magnetic bottle

(b) Modified axial potential

Figure 2.10: a) Ferromagnetic ring electrode with the corresponding magnetic field lines and magnetic field in axial direction. b) The axial potential modified by the addition of the magnetic bottle for spin-up and spin-down particles. Adapted from [41].

by the radial magnetic moments $\vec{\mu}_+, \vec{\mu}_-$

$$\vec{\mu}_= \vec{\mu}_S + \vec{\mu}_+ + \vec{\mu}_-. \tag{2.73}$$

The frequency shift $\Delta\omega_{z,SF}$ can also be denoted with the respective quantum numbers of the eigenmodes [98]:

$$\Delta\omega_z \approx \frac{h\omega_+}{m\omega_z}\frac{B_2}{B_0}\left(\left(n_+ + \frac{1}{2}\right) + \frac{\omega_-}{\omega_+}\left(n_- + \frac{1}{2}\right) + \frac{g}{2}m_s\right), \tag{2.74}$$

with the spin quantum number $m_s = \pm\frac{1}{2}$.

Utilizing the continuous Stern-Gerlach effect the magnetic moment of the electron and position were determined in 1987 [69]. For protons, the first measurement of spin transitions [98] was conducted in 2011, also by applying the continuous Stern-Gerlach effect. The determination of spin transitions for (anti)protons is particularly difficult because μ_p/m_p is a factor 10^{-6} smaller for protons than electrons. For this reason, a very large magnetic bottle has to be implemented in the trap setup to be able to resolve the axial frequency shift induced by a spin transition $\Delta\omega_{z,SF}$. For BASE the implemented magnetic bottle has a strength of $B_2 \approx 266\,\frac{\mathrm{kT}}{\mathrm{m}^2}$, which induces a frequency shift of $\Delta\omega_{z,SF} \approx 173\,\mathrm{mHz}$ (see Chapter 4.2.1).

Chapter 3

Experimental setup

3.1 The Antimatter factory

Currently, the only place on earth where low-energy antiprotons can be provided is at CERN, in the Antimatter Factory (AMF). Figure 3.1 shows the CERN accelerator complex, with the well-known Large Hadron Collider (LHC) and its pre-accelerators. At CERN, not only high-energy physics [8, 9, 99, 100] but also low-energy physics is investigated. For example, using rare-isotope beams at ISOLDE [101, 102] and inspecting the properties of antimatter in the AMF [103, 104].

The purpose of the AMF is to produce antiprotons and to slow them down to low energies ($< 6\,\mathrm{MeV}$), enabling experiments to test fundamental symmetries with low-energy antiprotons. In the AMF, antiprotons are initially produced through collisions of high-energetic protons ($E = 26\,\mathrm{GeV}$) from CERN's Proton Synchrotron (PS) with an iridium target, resulting in interactions with the protons of the target [103, 106]. Following

$$p(\mathrm{beam}) + p(\mathrm{Ir\text{-}target}) \rightarrow p + p + p + \overline{p} \tag{3.1}$$

antiprotons are produced. The produced antiprotons have an energy of $E \approx 3.6\,\mathrm{GeV}$, which is too high to capture them in a Penning trap. Therefore, they are subsequently injected into the Antiproton Decelerator (AD) [107, 108], where they undergo multiple stages of deceleration interleaved with stochastic and electron cooling and leave the AD with an energy of $E \approx 5.3\,\mathrm{MeV}$ [103]. Since 2021, the new Extra Low Energy Antiproton storage ring (ELENA) [36] has been supplying the experiments with antiprotons. It decreases the energy of the antiprotons even further to $E \approx 100\,\mathrm{keV}$ and is able to provide antiprotons to four experiments at the same time, compared to just one experiment with

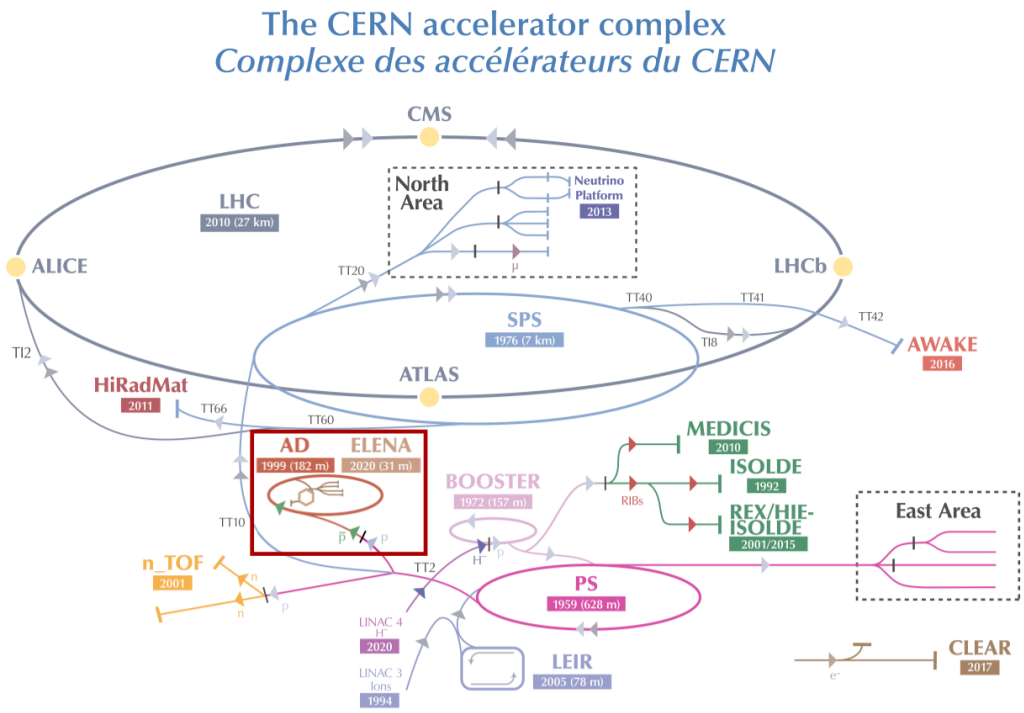

Figure 3.1: The CERN accelerator complex with a focus on antiproton production and deceleration in the Antimatter Factory (AMF) (red box). H^--ions are being accelerated in the linear accelerator LINAC 4 (purple). Then, they are stripped of their electrons and continue to be accelerated in the BOOSTER as protons (light purple). The protons enter the next acceleration stage in the Proton Synchrotron (PS) (pink), reaching energies of $E = 26\,\text{GeV}$. The Proton Synchrotron supplies various areas at CERN with protons, such as the East Area, the AMF, and the next larger accelerator SPS, which then supplies beam to the LHC. In the AMF, proton bunches are shot onto an iridium target for antiproton production. Antiprotons resulting from these collisions still have an energy of $E \approx 3.6\,\text{GeV}$. They are guided to the Antiproton Decelerator (AD), where their energy is reduced to $E \approx 5.3\,\text{MeV}$, and afterward, they progress to the Extra Low Energy Antiproton ring (ELENA). Here, the energy of the antiprotons is reduced further to $E \approx 100\,\text{keV}$, and then the beam is distributed to the experiments. Adapted from [105].

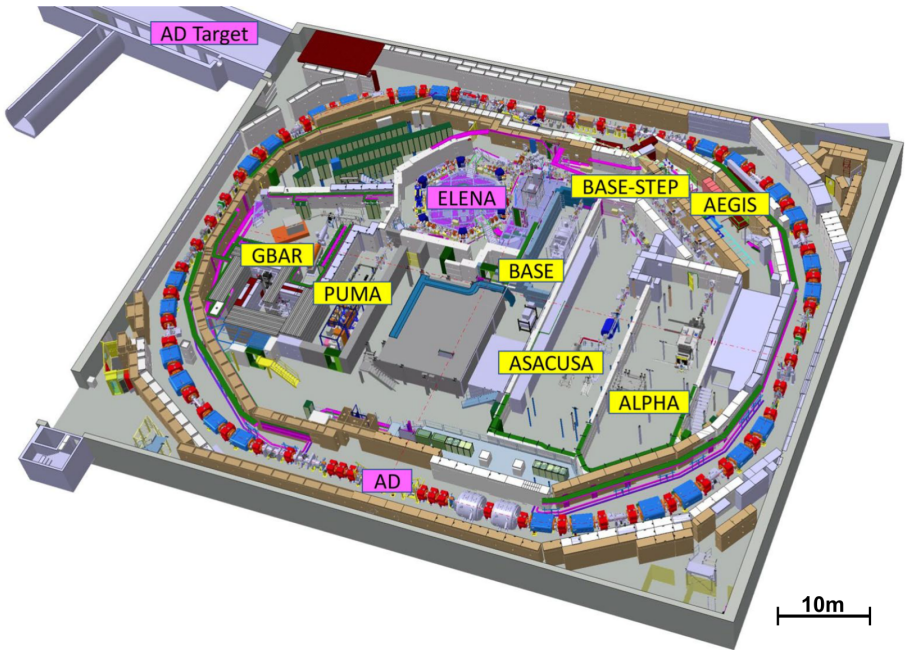

Figure 3.2: Overview of the AMF facility located at CERN. Adapted from [104].

the AD alone. Moreover, the transmission efficiency through an additional degrader (Section 3.2.3) of a 5.3 MeV beam - like in the AD - is less than 2.5 ‰, whereas for, a 100 keV antiproton beam, it is increased to 20 % [109], when a thinner, energy-matched degrader is employed. As a result, ELENA delivers almost two orders of magnitude more antiprotons to the users using the same pre-accelerator infrastructure, which is especially important for antihydrogen production [38].

Figure 3.2 shows the interior of the AMF. Antiprotons are generated in the AD target area, highlighted on the top left. From there, they are injected into the AD, which is installed along the inner perimeter of the AMF and encircles ELENA and the experimental zones. Currently, six collaborations are permanently located in the AMF: AEGIS [110], ALPHA [109], ASACUSA [45, 111], BASE [41], GBAR [42], and PUMA [43]. Among these, AEGIS, ALPHA, and GBAR are set to investigate the gravitational behavior of antihydrogen. Both AEGIS and GBAR have recently reported successful production of antihydrogen [110, 112], while ALPHA has already successfully performed the first gravitational measurements with antihydrogen [39]. In addition, the ALPHA collaboration conducts precision laser spectroscopy on the 1S-2S and 1S-2P transitions in antihydrogen [50, 113]. The ASACUSA collaboration aims to use an antihydrogen beam [111] for studies of the hydrogen-antihydrogen ground state hyperfine splitting [114] and also in-

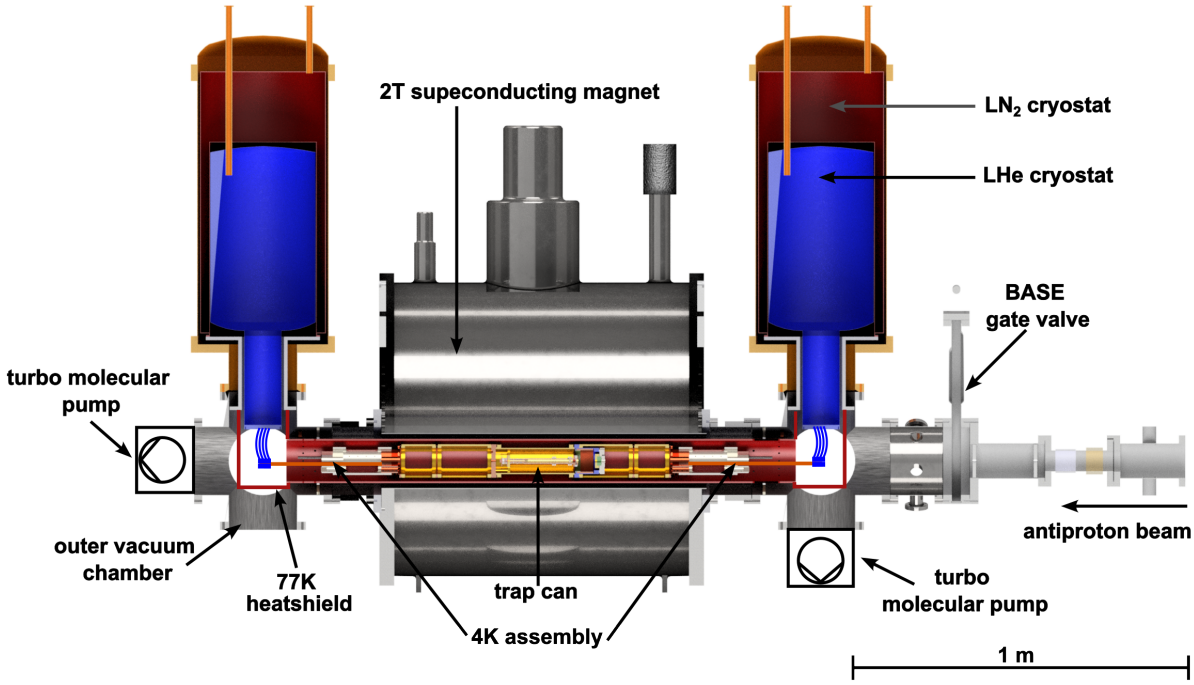

Figure 3.3: Section view of the BASE apparatus. In the center is the superconducting magnet, providing a 2 T magnetic field. Inside the warm bore of the magnet is the cryogenic assembly cooled to 4 K by the refrigeration system consisting of two cryostats, each having an LN_2 and LHe tank.

vestigates exotic antiprotonic helium for fundamental physics studies [45]. BASE tests fundamental symmetries by performing high-precision measurements of the proton and antiproton charge-to-mass ratios [55] and magnetic moments [56, 57] and aims to transport antiprotons outside the AMF (BASE-STEP) in order to supply an off-line precision experiment [61]. The PUMA collaboration also pursues the transport of antiprotons. They aim to transport antiprotons to CERN's isotope facility, ISOLDE, and to investigate the interaction and annihilation of antiprotons with radionuclides [43].

3.2 The BASE apparatus

3.2.1 Vacuum and cryogenic setup

The BASE experiment is located centrally inside the AMF, as is shown in Figure 3.2. Figure 3.3 shows a section view of the BASE apparatus. The main visible features are

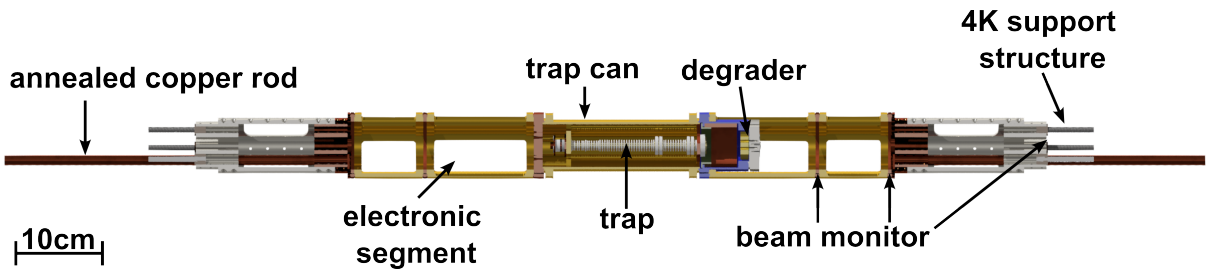

Figure 3.4: View of the cryogenic assembly. In the center is the trap stack, which is enclosed by the trap can. Together with the degrader, it forms a separate vacuum chamber. Downstream of the trap can is the so-called electronics segment hosting the axial detection system, filterboards, and all electrical connections necessary to operate the Penning traps. Upstream of the trap can, beam monitors are located. They are used to detect the injected antiproton beam, which helps with beam steering. The cryogenic assembly is on both sides flanked by the 4K support structure and a protruding rod. The rod is made of annealed copper to facilitate good heat transfer between the trap stage and the LHe cryostats.

a warm-bore superconducting magnet, housing the cryogenic stage including the Penning traps, detection systems [88], electronics [41] as well as a degrader [115] and beam monitors, and two cryostats supplying the refrigeration for the cryogenic stage.

The refrigeration system has two stages to reduce the heat load. Coming from room temperature (300 K), the first stage is a 77 K stage cooled by liquid nitrogen (LN_2), depicted in red in Figure 3.3, followed by a second stage cooled to 4 K with the help of liquid helium (LHe), shown in blue. The cryoliquids are stored in the two cryostats, both containing 35 l vessels of LN_2 and LHe each.

For the 77 K stage, aluminum boxes are screwed to the LN_2 cryostat, with interfaces for the electronic connections coming from the Penning traps and the detection systems. The two cryostats are connected with an aluminum tube inside the bore of the superconducting magnet. It is connected to the boxes via copper threads and rests on the double-crosses. The entire 77 K stage is wrapped with superinsulation foil to further reduce the heat load.

Inside the 77 K stage is the 4 K stage, cooled by the LHe inside the respective vessels. Figure 3.4 shows a drawing of the 4 K cryogenic assembly. At both ends of the assembly, an annealed copper rod is screwed to the bottom of the support structure. These rods are used for heat transfer between the LHe cryostat and the 4 K assembly. For this, they are clamped with a copper piece to the LHe-cryostat's cold fingers (OFHC copper braids) to absorb thermal contraction.

The 4 K assembly is mechanically secured to the 77 K heat shield with the help of Kevlar strings [93]. Figure 3.5 a) shows a photograph of the 4 K support structure and b) mounted

(a) Photograph of the 4 K support structure with three PTFE encased brass rods

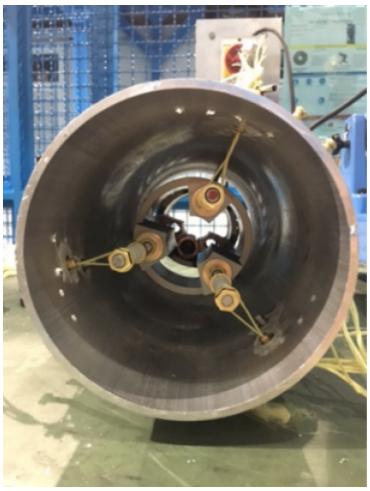

(b) 4 K support structure inside the 77 K shield supported by Kevlar strings.

Figure 3.5: Photographs of the 4 K support structure. a) shows the support structure with the three PTFE-encased brass rods where the Kevlar strings are attached. b) the support structure mounted inside the 77 K heatshield using the Kevlar strings. Photographs taken from [93].

inside the 77 K heatshield. Kevlar strings are placed around the three protruding rods housed in PTFE, placed within 120° of each other, and are guided outside the heatshield via hollow brass screws placed inside the heatshield. This minimizes, on the one hand, the direct contact of the 4 K stage with the 77 K stage. On the other hand, the three contact points enable the angular alignment of the 4 K assembly within the 77 K heatshield to a precision of 10 μm.

In the center of the 4 K assembly (Figure 3.4) is the trap stack, which is enclosed by the trap can. Together with the degrader, it forms a separate vacuum chamber. This vacuum chamber is prepumped to a pressure $p < 10^{-8}$ mbar and sealed by cold-welding a pinch-off tube. When cooled down to cryogenic temperatures, it can reach pressures $< 10^{-18}$ mbar, which can be determined by the storage time of the trapped antiprotons (see Chapter 6). Downstream of the trap can is the so-called electronics segment hosting the axial detection system [88] (Section 3.2.6) and filterboards [41] as well as all electrical connections necessary to operate the Penning traps (Section 3.2.4). Upstream of the trap can, beam monitors equipped with four-sector Faraday cups are installed. They monitor the injected antiproton beam, helping with beam steering (see Section 3.2.2).

Overall we reach temperatures of down to 5.2(1) K at the trap stage. The standing

time of the cryostats is about 60 hours, making it necessary to fill the experiment with cryoliquids every 2-3 days.

The following sections describe the components of the 4 K stage in more detail.

3.2.2 Beam monitors

The previously developed beam steering algorithm proved ineffective with the reduced ELENA beam energy of 100 keV. Consequently, it was decided to upgrade the diagnostics for beam steering. For this purpose, four new beam monitors were designed and built by Gilbertas Umbrazunas (PhD Student, ETH Zürich).

Figure 3.4 shows the position of three beam monitors on the 4 K stage. Another beam monitor is placed at 77 K attached to the 77 K heatshield box on the upstream side (Section 3.2.1).

The working principle of the beam monitors corresponds to the one previously installed in BASE [41], with the difference that all readout electronics are now at room-temperature compared to 4 K before. The beam monitor is a circular plate with four segments functioning as Faraday cups and an aperture in the middle. Figure 3.6 shows pictures of the different beam monitor designs. The first beam monitor on the 77 K stage is the largest and has an aperture of 19 mm to allow a wider spread beam further downstream before it gets more suppressed by the magnetic field of the BASE magnet. The aperture of the following beam monitors is 9 mm. BM2-4 are mounted on the trap stack on the 4 K stage. This resulted in some constraints in the shape of BM2, which made it necessary to crop part of the active area on segments 2 and 3, as can be seen in Figure 3.6 b). Compared to the old beam monitor, the new ones have their signal amplifiers outside the vacuum system, making them easily accessible. Moreover, it also reduces the heat load on the system because previously, it was necessary to heat the old beam monitor during operation, as the amplifier electronics were not functional at 4 K. The amplifiers are located upstream of the beam monitors in aluminum boxes at room temperature with feedthrough flanges (see also in Figure 5.2 labeled BM box). The amplifier consists of an inverting amplifier/integrator circuit with an additional video buffer amplifier to reduce noise caused by the impedance mismatch of the long amplifier-to-oscilloscope distance [116]. In total, 16 channels of the four beam monitors are read out by four oscilloscopes (Keysight DSOX1204G 200 MHz). Incident particles hit the Faraday cups of the beam monitors and create a sharp drop in the amplified signal that increases again over time.

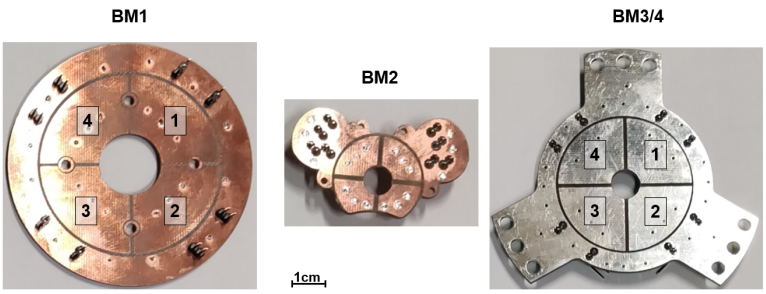

(a) Different BM design

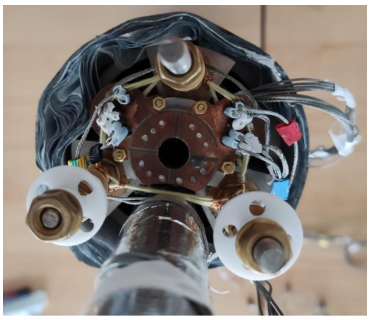

(b) BM2 implemented in the trap stack

Figure 3.6: a) PCBs of the different BM designs necessary for the different positions. The four Faraday cups are labeled with their respective channel number used for readout. b) Implementation of BM2 in the trap stack, where the space limitation for the shape of the beam monitor is visible. Segments 2 & 3 are slightly cropped due to the annealed copper rod used to thermalize the tap system to 4 K.

The amplitude of this drop corresponds to the incident number of antiprotons on the plate, enabling us to determine the fraction of antiprotons hitting one segment of a beam monitor. This knowledge is essential to steer the beam through the degrader and into the Reservoir trap (see Section 3.2.4 & Chapter 5) without annihilating upstream on other elements of the beamline.

3.2.3 Degrader

As mentioned above, the addition of ELENA made it necessary to adjust the BASE apparatus [41] to the lower antiproton energy, which was reduced from 5.3 MeV to 100 keV. This is still too much energy to catch antiprotons in a Penning trap, and therefore, a setup to decrease the antiprotons' energy further is needed. At BASE this is done by using a degrader foil. This section describes the new degrader setup implemented in BASE, summarizing the publication [115].

The degrader setup has two primary purposes: Firstly, as a vacuum window separating the extreme high vacuum (XHV) inside the trap can from the outer vacuum surrounding the trap ($< 10^{-7}$ mbar), and secondly to decrease the antiproton energy from 100 keV to below 5 keV to permit antiproton catching. Figure 3.7 shows the degrader setup and the integrated in the BASE trap can, the vacuum chamber surrounding the trap stack. The trap can is closed by the degrader flange (silver), which also supports the degrader foil. The current degrader window is a 1700 nm thick Mylar foil vaporized on both sides with a

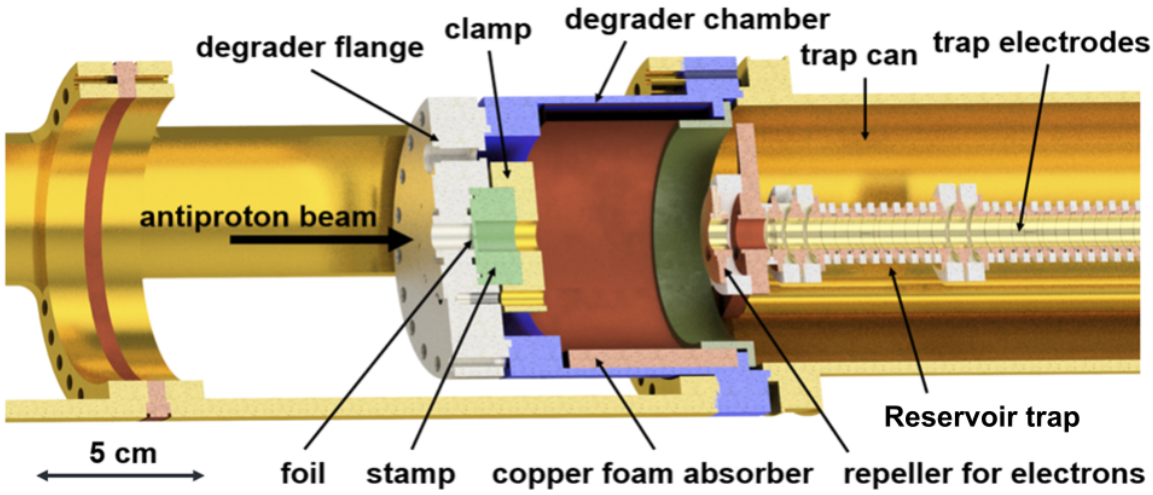

Figure 3.7: Scheme of the degrader setup implemented in the BASE experiment. Adapted from [115].

30 nm thick aluminum layer. The vacuum window is glued using a thin layer of Apiezon N grease [117] on a stamp (green) with seven transmission channels (holes with a diameter of 1 mm) placed in the corners of a regular hexagon with a side length of 1.5 mm. This gives a geometrical acceptance of 17% of the ELENA beam. Between the foil and the stamp, the vacuum is sealed using indium. To protect the degrader foil from unevenness in the indium seal, a Kapton ring is placed between them, covering the area where the foil would touch the degrader flange.
The degrader foil and the stamp are held by a clamp (yellow), which is screwed to the degrader flange and ensures even pressure distribution of the used indium seal, which is placed between the degrader flange and the foil.
The rest of the degrader chamber is filled with copper foam, which increases the surface area in the trap chamber by a factor of 2.5, which is utilized for better cryopumping in the trap vacuum.

The complete degrader setup has an acceptance of 2.5% of the antiproton beam when applying a catching potential of 5 kV [115].

3.2.4 BASE trap stack

The BASE trap stack consists of four main cylindrical Penning traps [78], designed in an orthogonal and compensated way (see Chapter 2.1.2.1): the Reservoir trap (RT), the Precision trap (PT), the Analysis trap (AT) and the Cooling trap (CT).

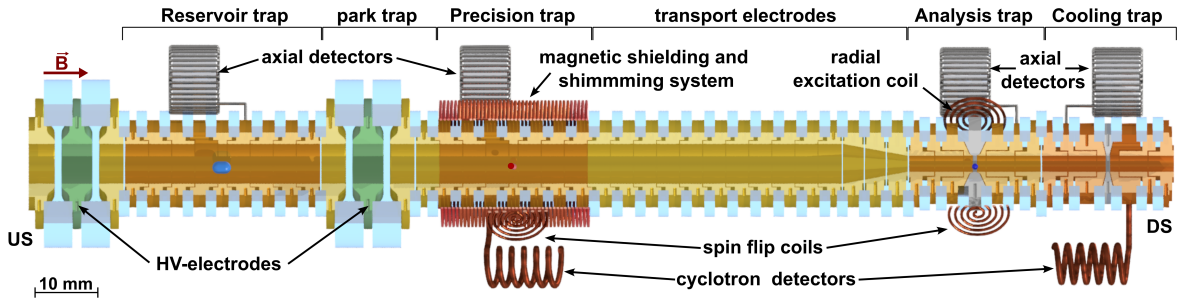

Figure 3.8: BASE trap stack with the four purpose Penning traps as implemented since autumn 2022.

All electrodes are made of high-purity oxygen free copper (OFHC), except for the ferromagnetic ring electrodes of the AT and CT. All trap electrodes are first coated with an inner layer of 6 μm silver (RT and PT) or nickel (AT and CT) and an outer layer of 8 μm gold, and are separated and insulated by sapphire rings.

Figure 3.8 depicts the trap stack. The RT and PT are built in the same way: they have an inner radius of 9 mm, the central ring electrode has a length of 1.34 mm, and the correction electrodes of 3.56 mm. Compared to this, the AT and CT have a smaller inner diameter of 3.6 mm. Therefore, the traps are also referred to as big and small traps, respectively. Besides the four traps described below, the trap stack includes two high-voltage (HV) electrodes (green) enclosing the RT. They are required to catch antiprotons, which is discussed in more detail in Chapter 5.2.

Between the PT and the AT lies the so-called transport section, used to transport particles between the two traps. It has two functions: It contains electrodes with an inner diameter shaped like a funnel connecting the electrodes of the traps with a larger inner diameter (RT & PT) with the ones having a smaller one (AT & CT). Secondly, it increases the distance between the big traps (RT & PT) and the ferromagnetic ring electrodes of the small traps (AT & CT), which create magnetic field inhomogeneities. This is important as field inhomogeneities induce systematic frequency shifts (see Chapter 2.1.2.2). The increased spacing reduces the influence of these inhomogeneous components at the location of the PT, where a highly homogeneous magnetic field is essential.

Reservoir trap

The RT [118] is the most upstream trap, enclosed by the HV-electrodes. It is used for catching and storing of protons, antiprotons, and H^--ions and for extracting a single

particle to the precision measurement traps. The RT is vital for the execution of precision measurements, as it allows us to conduct measurement campaigns outside the beam schedule, when the presence of disruptive noise sources is reduced [119]. A detailed description of the RT, and the catching, cleaning, and maintenance procedures can be found in Chapter 5. The content of the RT is continuously monitored via an axial resonator [88] with a resonance frequency of $\nu_{\text{res}} \approx 802\,\text{kHz}$ to monitor the particle count by the dip width (Chapter 2.2), letting us estimate a direct lower limit of the antiproton lifetime, as presented in Chapter 6.

Precision trap

The PT is used to determine the free cyclotron frequency of the trapped particle and is located downstream of the Reservoir trap, in the most homogeneous region of the superconducting magnet to minimize systematic effects on the frequency measurements (see Chapter 2.1.2.2).
The Precision trap is equipped with a tunable axial [88] and cyclotron detection system [89, 90]. The axial detector resonates at a frequency of $\nu_{\text{res}} \approx 637\,\text{kHz}$, and has a feedback loop (Chapter 2.2.2). The cyclotron resonator with a resonance frequency $\nu_{\text{res}} \approx 29.645\,\text{MHz}$ can be used to cool the particle's cyclotron mode resistively and detect the particle's modified cyclotron frequency. If the particle-detector interaction is not desirable, it can be tuned nearly 4 MHz away from the particle's cyclotron frequency [90]. To compensate magnetic field inhomogeneities and fluctuations, a shimming [86] and shielding system [119, 120] is located around the PT with a shielding factor > 50. Utilizing the shim coils the quadratic magnetic field gradient B_2 can be tuned in a range of $\pm 500\,\text{mT/m}^2$ and the linear gradient B_1 between 10 mT/m and 24 mT/m. Additionally, a coil is located next to the PT in order to drive spin transitions of the stored particle.

Analysis trap

The AT is used for spin state detection [95, 98]. It is located downstream of the elongated transport section, separating the AT and PT trap centers by 74 mm. The transport section ends with a funnel due to the smaller inner diameter of the Analysis trap of 3.6 mm. It is equipped with a feedback-cooled [121] axial detection system with a resonance frequency of $\nu_{\text{res}} \approx 658\,\text{kHz}$ [88].
The spin state detection utilizes the continuous Stern-Gerlach effect (Chapter 2.3). For

this, a large magnetic bottle is needed, which is provided by a ferromagnetic ring electrode made out of VACOFLUX 50, resulting in quadratic magnetic field inhomogeneity in the AT of $B_2 = 266(8)\,\mathrm{kT/m^2}$. Although the magnetic bottle enables us to detect a spin transition, it also introduces axial frequency shifts with a change in radial energy, especially in the cyclotron mode [122]. For this reason, the AT is not equipped with a cyclotron detector, and frequency detection of the radial modes is not possible via sideband-cooling (see Chapter 2.2.3). Nonetheless, the magnetron and cyclotron frequency can be determined by monitoring the axial frequency shift while irradiating an appropriate drive. For this, a radial excitation coil is placed next to the AT. To reduce the residual heating due to electronic noise [122], the radial and spin-flip coil are bandpass filtered, and, if not used, grounded via cryogenic switches [123].

Cooling trap

The CT is a trap dedicated to minimizing the cooling time of the cyclotron mode of a particle, thus increasing sampling statistics of a g-factor measurement (see Chapter 4.1). For this purpose, it has a cyclotron resonator with a resonance frequency of $\nu_{\mathrm{res}} \approx 28.632\,\mathrm{MHz}$ with a tunability of 4.5 MHz, and a small inner diameter of 3.6 mm. This reduces the effective electrode distance D_{eff} of the trap to 4.8 mm compared to 21.5 mm for the pick-up of the cyclotron detection signal in the PT. As the cooling time $\tau_{\mathrm{cool}} \propto D_{\mathrm{eff}}^2$ (see Chapter 2.2), the cooling time is reduced by a factor of ≈ 20. Additionally, the ring electrode is made out of ferromagnetic nickel, resulting in a magnetic bottle with a strength of $B_2 = 42\,\mathrm{kT/m^2}$. An axial detection system is implemented, which should be able to detect the cyclotron energy of the to be cooled particle through the axial frequency shift. For experimental reasons, the AT detection system is used to determine the cyclotron energy of the particle. A detailed description of this improved cooling technique is presented in Chapter 4.

3.2.5 Electronics and wiring

This section gives a brief overview of the electric connections in the BASE experiment. An exemplary detailed description of the different connections for the RT can be found in Chapter 5.1.

Figure 3.9 [90] gives an overview of all electric connections from the BASE trap stack to the corresponding frequency generators (FG), power supplies (PS), and signal analyzers

(FFT), as well as the connected detection systems, filter stages, and excitation lines.

The trap electrodes are biased (black) by the ultra-stable precision power supply UM 1-14 from Stahl Electronics [124]. All DC-biasing lines are typically filtered by four RC low-pass filters, on each cryostage one, with a cut-off frequency of about 30 Hz. Special lines are depicted in different colors in Figure 3.9, for a more detailed description of the various lines the reader is referred to Chapter 5.1.
To excite the particles' eigenfrequencies, excitation lines connect frequency generators to the trap electrodes (green). The radial excitation line is attached to a segmented electrode to generate a quadrupole field coupling the respective radial mode to the axial mode (Chapter 2.2.3) [96]. Two spin-flip coils (yellow) are placed next to the PT and AT to irradiate a radio-frequency drive for spin manipulation.
To detect the axial frequency of the trapped particles, each trap is equipped with an axial resonator [88]. The amplified particle signal (red) is read out by a Stanford Research System spectrum analyzer (SR 780) [125], where the amplifier biasing is marked in blue. To utilize active electronic feedback (Chapter 2.2.2), feedback loops (orange) are installed in the PT and AT axial detection systems.
Additionally, cyclotron detectors are connected to the PT and CT and are depicted in purple. More details on the resonators can be found in Section 3.2.6.
Last but not least, the HV-electrodes are used for catching antiprotons (see Chapter 5) and are biased through a wire inside a grounded stainless steel tube, to avoid sparking and crosstalk with the rest of the apparatus. They are tested to supply voltages up to 4.5 kV, and for catching typically voltages up to 2 kV are applied.

To reduce noise and with this unwanted heating of the trapped particles, all unused lines are typically grounded via relays or a switch matrix [126].

3.2.6 Detection systems

The measurement of the eigenfrequencies of the trapped particle relies on the detection of image currents induced in the trap electrodes (see Chapter 2.2.1). In the BASE experiment, this is facilitated by highly sensitive resonators [88–90]. As mentioned in Section 3.2.4, each trap has one axial detection system, and two cyclotron resonators are connected to the PT and CT.

The axial coils have a toroidal design and consist of three layers of 75 μm PTFE insulated superconducting NbTi wire wound on PTFE cores. The coils are placed inside

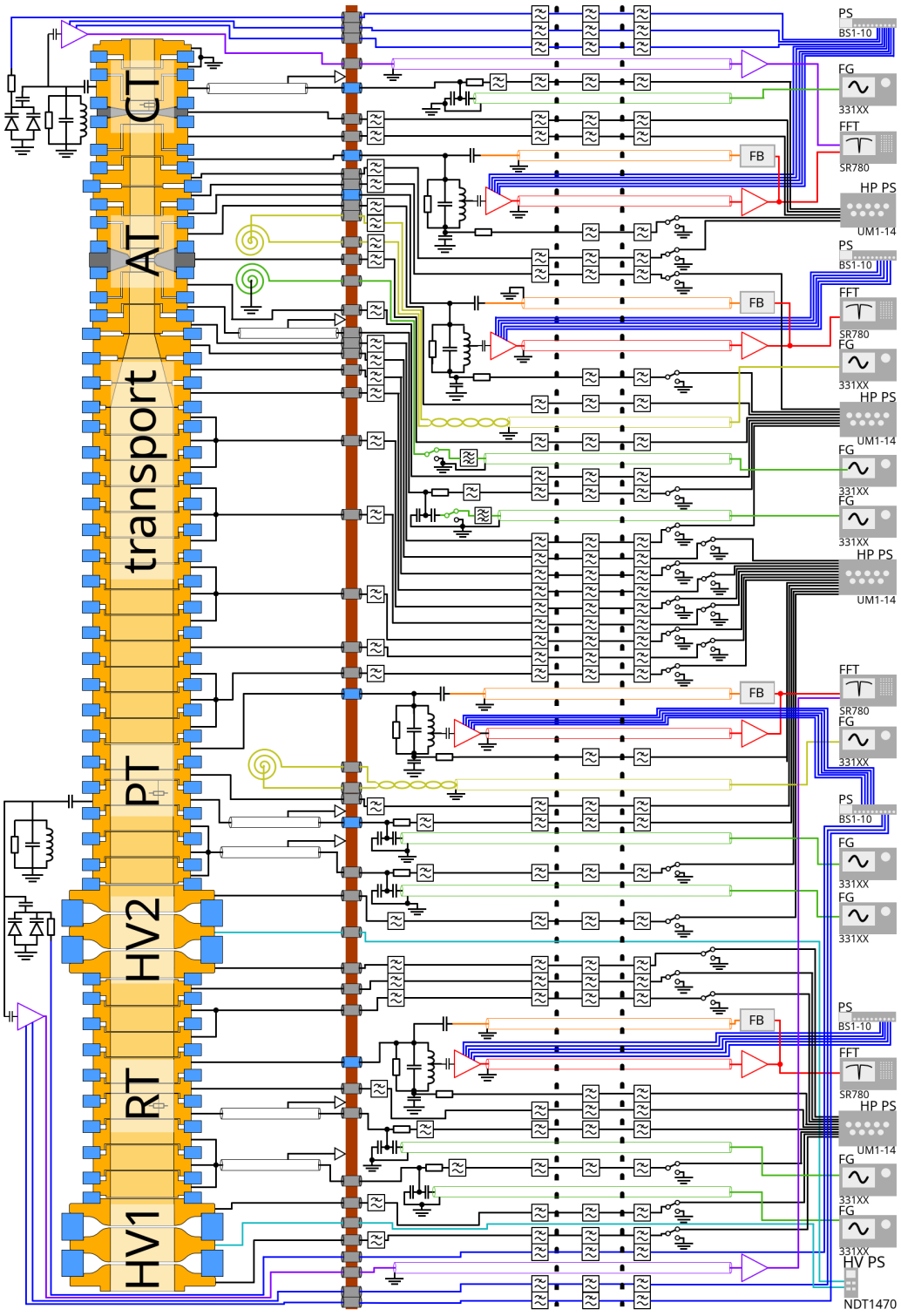

Figure 3.9: Electric connections in the BASE experiment, for details see text. Taken from [90].

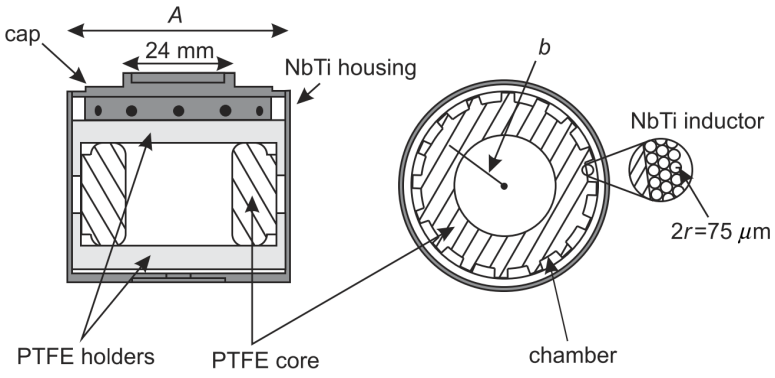

(a) Sketches of the axial resonator design

(b) Photo of the CT cyclotron detector

Figure 3.10: a) Sketch of the axial resonators. PTFE-insulated NbTi wire is wound in a toroidal design around a PTFE core, which is placed inside a NbTi housing and stabilized with PTFE holders. The outer diameter A of the housing is either 41 mm or 48 mm, and the radius of the central axis of the toroid b is either 13 mm or 15.75 mm for the big and small traps, respectively. Taken from [88]. b) Photograph of the CT cyclotron detector. The cyclotron detectors are solenoids wound out of 1 mm annealed copper wires soldered directly to the bottom plate of their copper housing. Taken from [90].

cylindrical NbTi housings and wound on PTFE holders. Figure 3.10 a) shows sketches of the design of the axial resonators [88]. The outer diameter of the housing A is given by geometrical constraints and is 41 mm and 48 mm for the big (RT & PT) and small traps (AT & CT), respectively, and the radius of the central axis of the toroid b is either 13 mm or 15.75 mm [127]. The four axial resonators are placed in the electronics segment of the 4 K stage of the apparatus (Figure 3.4). An overview of the different detector parameters during operation of the experiment can be found in Table 3.1.

The utilized cyclotron detectors were designed and commissioned in the PhD work of Markus Fleck [90]. They are solenoids made of 1 mm annealed copper wire and placed inside an OFHC copper housing. To minimize parasitic capacitance and electromagnetic interference, the wire length to the trap electrode was reduced by placing both cyclotron detectors directly next to the trap stack, inside the trap can. This contrasts with the 2016/2017 run, during which the detectors were located in the electronics segment alongside the axial resonators [41, 56]. The location inside the trap can also provides additional shielding, resulting in an overall lower detector temperature (see Chapter 4.2). The cyclotron detectors include a varactor, resulting in a tuning range of the resonance frequency

detector	ν_{res}	Q-value	R_{p}	L
RT axial	802 kHz	10 600	76.6 MΩ	1.43 mH
PT axial	637 kHz	10 400	71 MΩ	1.71 mH
AT axial	658 kHz	21 500	195 MΩ	2.19 mH
CT axial	620 kHz	21 500	183 ,MΩ	2.19 mH
PT cyclotron	29.645 MHz	1 400	412 kΩ	1.58 μH
CT cyclotron	28.632 MHz	1 050	340 kΩ	1.73 μH

Table 3.1: Overview of the different resonators implemented in BASE with their resonance frequency ν_{res}, their Q-value, parallel resistance R_{p}, and inductance L.

of $\approx$ 4 MHz. Parameters of the implemented cyclotron detectors are shown in Table 3.1.

3.2.7 Electron gun

An electron gun is installed as the most downstream part of the trap stack and fulfills two purposes: It is used to load electrons into the RT to sympathetically cool antiprotons, and to generate protons, which can be used for the commissioning of the experiment. Electrons are emitted from a tungsten wire using field emission induced by tunneling.

In Figure 3.11 a scheme of the electron gun assembly is shown. It consists of three electrodes and a sharp field emission point (FEP) made of tungsten wire. Outermost of the assembly is the base-electrode, in which the FEP is screwed. It is negatively biased, typically at -45 V, and defines the energy of the electrons emitted by the FEP. Directly adjacent to the tip of the FEP is a HV-electrode, typically biased to $\approx$ 1250 V. The potential difference between the FEP and the HV-electrode pulls electrons from the FEP, resulting in an electron beam. Changing the HV adjusts the intensity of the beam of $\approx$ 130 nA. Closest to the trap stack is a grounded shield electrode. On the opposite side of the trap stack, in upstream direction, is a copper mesh (see also Figure 5.3), which is used as a target for the electron beam. On the one hand, the current from the absorbed electrons is measured and used as a diagnostic tool. On the other hand, it is used as a target for generating protons due to molecular hydrogen dissociation when interacting with the electron beam.

Another important field of application is the usage of electrons to cool antiprotons after catching [128]. Electron cooling in this context means cooling antiprotons sympathetically with colder electrons. Particles trapped in a magnetic field lose energy by cyclotron

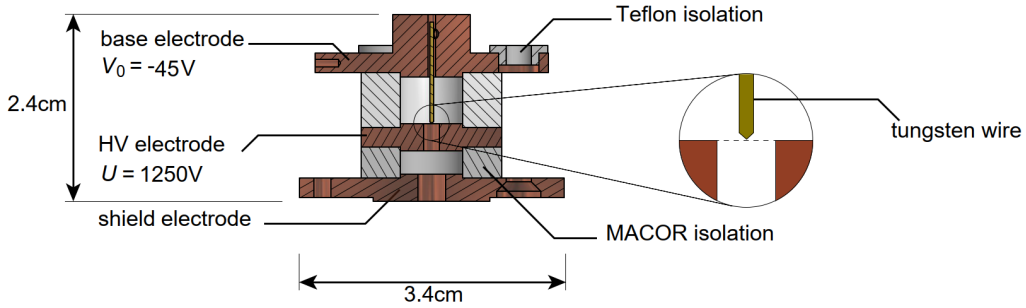

Figure 3.11: Schematic of the electron gun. Adapted from [130].

radiation, with the cooling time constant [129]

$$\tau_{\mathrm{rad}} \propto \frac{m^3 c^3}{q^4 B^2}. \tag{3.2}$$

As electrons are ≈ 2000 times lighter than the antiprotons, they lose energy much faster in the form of cyclotron radiation than antiprotons and can then sympathetically cool them. The colder antiprotons are subsequently cooled further resistively via the interaction with the detection system.

When loaded, electrons can be detected as a shift in the resonance frequency of the axial resonator [68, 131]. The theoretical induced frequency shift after loading N_e electrons is [132]

$$\Delta\nu = 0.004556 + 0.000079 \times N_e. \tag{3.3}$$

To sympathetically cool antiprotons, we normally load in the order of 6.3×10^6 electrons, corresponding to a resonator shift of $\approx 500\,\mathrm{Hz}$.

Chapter 4

The Cooling trap and its relevance for the g-factor measurement

After CERN's Long Shutdown 2 (LS2) the goal of the BASE experiment is the improved (more precise) measurement of the antiproton magnetic moment [56]. In 2016/2017 the magnetic moment of the antiproton was measured to a precision of 1.7 p.p.b. [56, 58]. Overall, the statistical uncertainty of the measurement is the dominant uncertainty, therefore one way to improve the precision of the next g-factor measurement is an improved sampling rate. This is necessary since BASE can only perform high-precision measurements during CERN's YETS (Year End Technical Stop), typically lasting for about three months.

This Chapter first reviews the principle of a high-precision g-factor measurement in a Penning trap and then outlines the newly implemented Cooling trap and its significance for an improved g-factor measurement of the antiproton, which was first published in Phys. Rev. Lett., with contributions of the author of this thesis [63].

4.1 The g-factor measurement

As mentioned earlier (Chapter 2.3), the g-factor of a proton/antiproton in a Penning trap is determined by measuring two frequencies: the cyclotron frequency ν_c and the Larmor frequency ν_L:

$$\frac{g}{2} = \frac{\nu_L}{\nu_c}. \tag{4.1}$$

The cyclotron frequency ν_c of a particle in a Penning trap can be determined by measuring its three eigenfrequencies ν_+, ν_z and ν_- using image current detection and sideband coupling techniques and applying the invariance theorem (Equation (2.12)) [70, 77]. The Larmor frequency ν_L on the other hand can not be measured directly, as the Larmor precession does not induce image currents. Therefore, the continuous Stern-Gerlach effect (see Chapter 2.3) is used to couple the spin magnetic moment to the axial frequency ν_z by introducing a magnetic bottle with a quadratic field inhomogeneity of $B(z) = B_0 + B_2 z^2$. This results in a shift of the axial frequency depending on the orientation of the spin. However, the magnetic bottle does not only couple the spin magnetic moment to the axial potential but also the orbital (magnetron and cyclotron) magnetic moments. The resulting shift of the axial frequency can thus be expressed using the cyclotron n_+, magnetron n_-, and spin m_s quantum numbers [70]

$$\Delta\nu_z = \frac{h\nu_+}{4\pi^2 m\nu_z}\frac{B_2}{B_0}\left(\left(n_+ + \frac{1}{2}\right) + \frac{\nu_-}{\nu_+}\left(n_- + \frac{1}{2}\right) + \frac{g}{2}m_s\right). \tag{4.2}$$

Having a closer look at Equation (4.2), we can make the following observations at typical experimental parameters in BASE: a) the axial frequency shift induced by a spin transition at a $B_2 = 266(8)\,\mathrm{kT/m^2}$ is $\Delta\nu_{z,\mathrm{SF}} = 173(5)\,\mathrm{mHz}$ with $B_{0,\mathrm{AT}} = 1.21\,\mathrm{T}$. b) One cyclotron quantum jump induces an axial frequency shift of $\Delta\nu_{z,+} = 62(2)\,\mathrm{mHz}$ and c) an axial frequency shift by a magnetron quantum jump is suppressed by the factor $\nu_+/\nu_- \approx 1500$ and therefore negligible. This highlights, that it is crucial to suppress energy changes in the modified cyclotron mode as already three cyclotron quantum jumps make a spin-flip detection impossible.

When measuring the g-factor with the highest precision the following issue arises: In order to resolve the frequency difference between the two spin-states, a high magnetic inhomogeneity B_2 is needed (Equation (4.2)), but as explained in Chapter 2.1.2.2, a high B_2 results in systematic frequency shifts in all eigenfrequencies of the particle, consequently limiting the precision of a measurement performed in one trap with a superimposed magnetic bottle to a relative precision of 10^{-6} [98, 133]. This issue can be decoupled using two traps: one to determine the spin-state of the particle, the so-called Analysis trap (AT), and one where the cyclotron frequency of the particle is determined, which is named Precision trap (PT). This so-called double-trap scheme [134] was among others used for an improved proton magnetic moment measurement, which reached a fractional resolution of 300 p.p.t. [57, 135].

The next sections will first discuss how to determine the spin-state of a particle [95] before laying out the measurement scheme of the double-trap method in detail [57, 134]. Next, a short discussion of the two-particle method follows [56], which allows for much faster g-factor measurements, a crucial benefit in the limited measurement time available in an accelerator hall.

4.1.1 Spin-state analysis

When measuring the g-factor of a particle using two different traps [56, 135], the PT is used to determine the g-factor resonance. This is done by measuring the eigenfrequencies of the particle to determine its cyclotron frequency ν_c and by measuring the spin-flip probability P_{SF} depending on the applied rf-drive. For the high-resolution of the cyclotron frequency, an as homogeneous magnetic field as possible is desirable, thus it is not possible to determine directly in the PT if the particle's spin flipped after the irradiation of the radio-frequency drive. Therefore, is necessary to know the spin-state of the particle before applying the so-called spin-flip drive in the PT, and afterward as well. For this purpose, the particle is transported in the AT, which has a strong magnetic bottle B_2, to determine the spin-state. The following describes the spin-state read-out in the AT, as discussed in detail in [95]. The complete g-factor measurement schemes are then described in Section 4.1.2 and Section 4.1.3.

The spin-state read-out in the AT relies on the unambiguous detection of driven spin-flips itself. As mentioned above, a flip of spin shifts the axial frequency of the particle by $\Delta\nu_{z,SF} \approx 173\,\text{mHz}$. Following Equation (4.2) also cyclotron transitions can lead to a significant frequency shift compared to a spin transition. To detect the spin-state, first, the axial frequency is measured $\nu_{z,AT,1}$. Then an incoherent radio-frequency drive at the Larmor frequency is applied, which flips the spin with a probability $P_{SF} \approx 50\%$ [133]. Afterwards the axial frequency is measured again $\nu_{z,AT,2}$. If the frequency shift $\Delta_{\nu_z} = \nu_{z,AT,2} - \nu_{z,AT,1}$ between the two measurements is close to zero, no spin-flip occurred. In case a spin-flip happened, we would expect a frequency shift of about $\Delta\nu_{z,SF}$ in an ideal experimental setup.

In reality, background frequency fluctuations Ξ_{BG}, dominated by cyclotron random-walk noise and white-noise induced by the FFT measurement of the axial frequency [122], result in an overall axial frequency scatter. As the cyclotron transition rate ζ_+ increases with increasing cyclotron energy E_+ of the particle, it is important to reduce E_+ in order

to decrease the background scatter Ξ_{BG}. The transition rate ζ_+ can be estimated by first-order transitions in a noise driven quantum mechanical oscillator with a noise spectral density of the electric field S_E at the modified cyclotron frequency ν_+ [122]:

$$\zeta_+ = \frac{q^2 n_+}{4\pi m h \nu_+} S_E(\nu_+), \tag{4.3}$$

and scales linear with the cyclotron quantum number $n_+ \propto E_+$. To reduce the cyclotron transition rate it is therefore important to have a particle with an as low as possible cyclotron energy E_+ in order to resolve spin-flips imposed on the axial frequency.

Accounting for these background fluctuations, multiple frequency shifts Δ_{ν_z} can be approximated as a normal distribution $h(\mu, \sigma)$, with the mean value $\mu = 0$ and the standard deviation $\sigma = \Xi_{\mathrm{BG}}$. Therefore, the probability of observing a frequency shift $\Delta_{\nu_\mathrm{z}} = \nu_{\mathrm{z,AT,2}} - \nu_{\mathrm{z,AT,1}}$ with an rf-drive applied in between the measurements is given by the probability density function [95]

$$\begin{aligned} p(\Delta\nu_\mathrm{z}) = &(1 - P_{\mathrm{SF}})\, h_0(0, \Xi_{\mathrm{BG}}) \\ &+ P_{\mathrm{SF}}\, p_\uparrow\, h_-(-\Delta\nu_{\mathrm{z,SF}}, \Xi_{\mathrm{BG}}) \\ &+ P_{\mathrm{SF}}\, (1 - p_\uparrow)\, h_+(\Delta\nu_{\mathrm{z,SF}}, \Xi_{\mathrm{BG}}), \end{aligned} \tag{4.4}$$

where $p_\uparrow$ is the probability, that the particle is initially in the spin-up ($|\uparrow\rangle$) state, and P_{SF} the spin-flip probability. Figure 4.1 depicts axial frequency shifts Δ_{ν_z} in the AT to identify the spin-state of the particle during the 2016 run [95]. Three Gaussian distributions are visible, where the central one corresponds to the case when no spin-flip occurred between the two axial frequency measurements. This is reflected in the first line of Equation (4.4) and in the red distribution in Figure 4.1. The green (h_-) and blue (h_+) distributions correspond to the case when the spin of the particle flipped, for the antiproton from up to down (green, second line Equation (4.4)) and down to up (blue, third line Equation (4.4)), respectively. Using a maximum likelihood analysis and setting the the probability that the antiproton is initially in the spin-up state $p_\uparrow = 0.5$, the background fluctuation $\Xi_{\mathrm{BG}} = 48.1(1.9)\,\mathrm{mHz}$, the spin-flip probability $P_{\mathrm{SF}} = 47.3(2.3)\%$, and the spin-flip frequency shift $\Delta\nu_{\mathrm{z,SF}} = 166(4)\,\mathrm{mHz}$ can be extracted [95].

To identify which spin-state the particle was originally in, we can use a threshold method. Here, the measured frequency shift Δ_{ν_z} has to be assigned to one of the sub-distributions in Equation (4.4). For this, we introduce a threshold frequency shift Δ_{th}

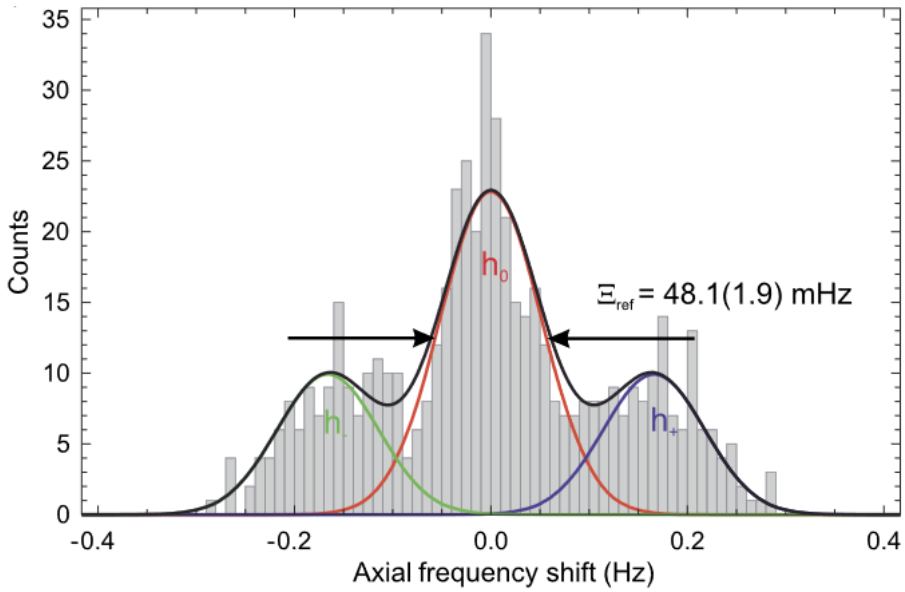

Figure 4.1: Histogram of the axial frequency shifts, with three sub-distributions visible. The green and blue distributions correspond to a spin-flip event, from $|\uparrow\rangle \rightarrow |\downarrow\rangle$ and $|\downarrow\rangle \rightarrow |\uparrow\rangle$, respectively. The central sub-histogram (red) shows events where no spin-flip occurred, from which the background axial scatter can be determined, in this case 48.1(1.9) mHz. Taken from [95].

and can assign the axial frequency shift Δ_{ν_z} in the measurement sequence as follows:

- $\Delta_{\nu_z} < -\Delta_{\text{th}}$: If an axial jump smaller than $-\Delta_{\text{th}}$ is observed, it is identified as a transition to the spin-down state, therefore the particle was initially in the spin-up state.

- $|\Delta_{\nu_z}| < \Delta_{\text{th}}$: In case the absolute value of the frequency shift is smaller than the threshold value Δ_{th}, no spin transition has occurred and no initial spin-state can be assigned. Only after a frequency shift larger than Δ_{th} an initial spin-state is identified.

- $\Delta_{\nu_z} > \Delta_{\text{th}}$: If an axial jump larger than Δ_{th} is observed, it is identified as a transition to the spin-up state, therefore the particle was initially in the spin-down state.

As can be seen in Figure 4.1, the three distributions can overlap if the background scatter is large enough, and therefore result in wrong spin-state identification. The error rate E_{th}, i.e. the probability to assign a single frequency shift $\Delta\nu_z$ for a given threshold Δ_{th}

incorrectly, is expressed as the integral over the overlapping distributions in Figure 4.1. By choosing an optimum threshold $\Delta_{\mathrm{th,opt}}$ the error rate E_{th} can be minimized [95]

$$\Delta_{\mathrm{th,opt}} = \frac{\Delta\nu_{\mathrm{z,SF}}}{2}\left(1 + \frac{2\Xi_{\mathrm{BG}}^2}{\Delta\nu_{\mathrm{z,SF}}^2}\ln(2/P_{\mathrm{SF}} - 2)\right), \tag{4.5}$$

and yields for the data presented in Figure 4.1 an optimum threshold $\Delta_{\mathrm{th,opt}} = 94\,\mathrm{mHz}$ resulting in $E_{\mathrm{th}} = 5.8\%$ [95].

In the two-trap g-factor measurement [56, 57, 134] the spin-state of the particle has to be known before the particle undergoes an interaction with the Larmor-drive in the PT, namely the spin-state has to be initialized. When increasing the threshold Δ_{th}, the initialization error rate E_i can in principle be reduced as much as needed. However, when the threshold is set too high, the probability of observing a spin-flip decreases leading to an increase in the time required to identify a spin-flip. In case it would be set too low, it adds an artificial background on the g-factor resonance. This has to be considered when choosing an initialization threshold $\Delta_{\mathrm{th},i}$. For a background scatter $\Xi_{\mathrm{BG}} \approx 48\,\mathrm{mHz}$ an initialization threshold of $\Delta_{\mathrm{th},i} = 190\,\mathrm{mHz}$ is chosen resulting in an initialization error rate $E_i < 0.1\%$ [95]. It should be noted that, for a small background scatter $\Xi_{\mathrm{BG}} \leq \Delta\nu_{\mathrm{z,SF}}/3$, which are the usual conditions in BASE, the mean error rate E_s is optimized for $\Delta_{\mathrm{th}} \approx \Delta\nu_{\mathrm{z,SF}}/2$ [95], as can be seen in the well separated spin-flip distributions in Section 4.2.3, Figure 4.12.

4.1.2 Double-trap method

When performing a double-trap g-factor measurement the first step is to cool the particle's cyclotron mode in order to guarantee a good spin-state initialization (Section 4.1.1). To this end, the particle interacts with the cyclotron detector in the PT, resistively cooling its cyclotron mode. Then the particle is moved to the AT and the cyclotron temperature $T_+ = E_+/k_{\mathrm{B}}$ is evaluated by measuring the particle's axial frequency, typically $T_+ < 200\,\mathrm{mK}$ [122, 136]. This is repeated multiple times until a cold enough particle is prepared. A more detailed description of the (upgraded) procedure can be found in Section 4.2.2.

In the next step, the spin-state is read out in the AT as described above. The axial frequency is measured interleaved with the irradiation of a Larmor drive to induce a spin-flip. This is repeated until an axial frequency shift $|\Delta_{\nu_z}|$ larger than a threshold frequency $\Delta_{\mathrm{th},i}$ is observed, and hence the spin-state is identified. Then the particle

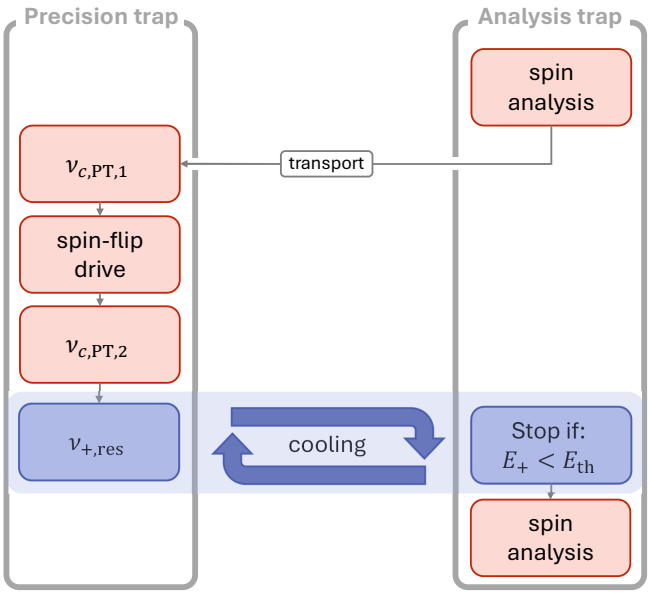

Figure 4.2: Measurement scheme for the g-factor using the double-trap method. First, the cyclotron-cold particle is in the Analysis trap and undergoes a spin-state initialization. Subsequently, it is moved to the Precision trap, where it samples the magnetic field. Then, a Larmor-drive is applied, which could lead to a spin-flip of the particle. Next, the cyclotron frequency is measured again. Due to the cyclotron frequency measurements, the cyclotron energy of the particle is too high to resolve its spin-state. Therefore, the particle's cyclotron-mode is sub-thermally cooled. To this end, the particle is shuttled between the Precision trap and the Analysis trap. Once the particle's cyclotron energy E_+ is below a set threshold E_{th}, it stays in the Analysis trap where a spin analysis is performed. This last step also marks the first one in the next cycle, beginning from the top.

is moved to the PT and its free cyclotron frequency $\nu_{\mathrm{c,PT,1}}$ is determined by sideband coupling the modified cyclotron to the axial mode [96] (see Chapter 2.2.3). Next, a spin-flip drive $\nu_{\mathrm{rf,PT}}$ around the calculated Larmor frequency $\nu_{\mathrm{L,PT}}$ is irradiated and the free cyclotron frequency is measured again $\nu_{\mathrm{c,PT,2}}$. This is done in order to interpolate the true value of the cyclotron frequency at the time of the Larmor-drive $\nu_{\mathrm{rf,PT}}$ irradiation, compensating for magnetic field fluctuations [93]. The measurement of the cyclotron frequency using sideband coupling, however, increases the cyclotron temperature of the particle to $T_+ = \frac{\nu_+}{\nu_z} T_z \approx 300K$ (Chapter 2.2.3). For this reason, the particle's cyclotron mode has to be cooled again before the readout of the spin-state. This measurement scheme is outlined in Figure 4.2 [57].

This measurement scheme enables us to determine the probability of a spin-flip occur-

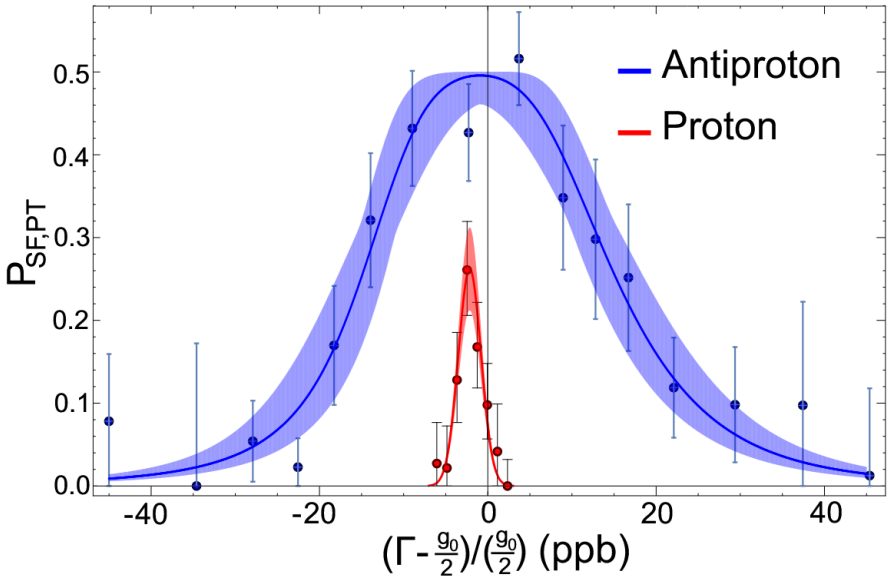

Figure 4.3: Resonance curves of the spin-flip probability P_{SF} as a function of the frequency ratio $\Gamma = \nu_{\mathrm{L}}/\nu_{\mathrm{c}}$. The red one depicts the resonance curve of the proton [57] and the blue one of the antiproton [56]. Both measurements are referenced to the 2014 proton magnetic moment measurement conducted by BASE [135]. Taken from [58].

ring at a given spin-flip drive $\nu_{\mathrm{rf,PT}}$ frequency. The spin-flip probability P_{SF} is assigned to the corresponding frequency ratio of the measured frequencies $\frac{\nu_{\mathrm{rf,PT}}}{\nu_{\mathrm{c,PT}}} = \frac{g}{2}$, and so a resonance curve of the g-factor is generated and a value for the g-factor can be extracted using a likelihood fit algorithm. The resonance curves from the 2017 measurements are shown in Figure 4.3 [58], where the 0.3 p.p.b. proton result is plotted in red [57], and the 1.7 p.p.b. antiproton result in blue [56]. The latter was obtained using the two-particle technique described in Section 4.1.3. It should be noted that the g-factor measurement of the proton using the double-trap technique took several months [57], whereas the antiproton resonance curve was sampled in only one month. The sampling time restriction arises from the downtime time of the decelerator during CERN's YETS, which is typically three months long. Only during this period, the g-factor resonance can be sampled, and systematic measurements sensitive to magnetic field changes can be studied. For this reason, the resonance was saturated on purpose in order to ensure good contrast between resonant and off-resonant spin-flip drive in the PT $\nu_{\mathrm{rf,PT}}$.

4.1.3 The two-particle method

As outlined above, one main limitation of the double-trap measurement scheme [57, 135] is the sampling statistics imposed by the long cooling time of the cyclotron mode in order to read out the spin-state of the particle. An idea to reduce this is to sample the g-factor resonance with two particles instead of one, first introduced by Stefan Ulmer in the 2017 antiproton magnetic moment measurement [56]. One particle, the so-called Larmor-particle has a low cyclotron temperature $T_+ = E_+/k_\mathrm{B}$ and is used for the spin-state analysis. The other particle is used to sample the cyclotron frequency before and after the Larmor drive $\nu_{\mathrm{rf,PT}}$ is applied in the PT, therefore called Cyclotron-particle. With this the cyclotron-mode cooling can be omitted in every step of the measurement and is only necessary once the Larmor-particle accumulates too much cyclotron energy for an efficient spin-state detection, typically the particle is cooled to $T_+ \approx 50\,\mathrm{mK}$ [56]. The mean heating rate of one measurement cycle corresponds to 17 mK, making a re-cooling of the Larmor-particle necessary after about 75 cycles [56].

The measurement principle is the same as outlined in Section 4.1, but instead of one particle, two-particles are extracted from the Reservoir trap. As a first step, the Larmor-particle is resistively cooled to cyclotron temperatures $T_+ < 200\,\mathrm{mK}$ in order to allow single spin-state detection with high fidelity [95]. This is done by interaction of the particle with the cyclotron detector in the PT. During the cooling procedure the Cyclotron-particle is stored in a Park trap located upstream of the PT. In the BASE trap stack (Chapter 3.2.4), one electrode is used as the Park trap, typically HVS.

Once the Larmor-particle is sufficiently cold it is stored in the AT and the Cyclotron-particle is transported to the PT and one measurement cycle can start as outlined in Figure 4.4. First the spin-state of the Larmor-particle is identified in the Analysis trap, which typically takes 25 minutes. Then the cyclotron frequency is sampled in the PT $\nu_{\mathrm{c,PT,1}}$ with the Cyclotron-particle. The cyclotron frequency is determined using the sideband-method (see Chapter 2.2.3) and with this, the cyclotron temperature of the particle is increased to $T_+ = \frac{\nu_+}{\nu_\mathrm{z}} T_\mathrm{z} \approx 300\,\mathrm{K}$. Then the particles are transported: the Cyclotron-particle is shuttled from the PT to the Park trap and the Larmor-particle from the AT to the PT. Next, a radio-frequency drive is applied in the Precision trap $\nu_{\mathrm{rf,PT}}$ in order to flip the spin of the Larmor-particle. It is important to note that the cyclotron detector of the PT is detuned by 800 kHz so that the cyclotron mode of the Larmor-particle is not heated. Nevertheless, in order to avoid an increase in cyclotron energy

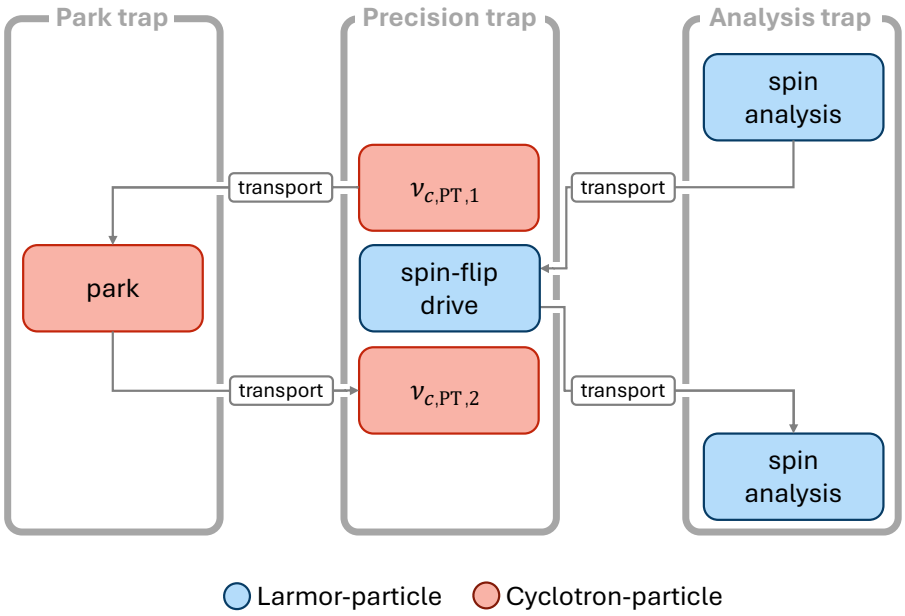

Figure 4.4: Two-particle method measurement scheme. First, the cyclotron-cold Larmor-particle (blue) is in the Analysis trap, where its spin-state is initialized. Next, the hot Cyclotron-particle (red) samples the magnetic field in the Precision trap. Subsequently, both particles are transported at the same time: The Cyclotron-particle into the Park trap and the Larmor-particle into the Precision trap. While the the Cyclotron-particle rests in the Park trap, the Larmor-particle experiences a spin-flip drive in the Precision trap. Then, both particles are transported back to their original positions. Next, the Cyclotron-particle again samples the magnetic field in the Precision trap and afterwards the spin-state of the Larmor-particle is re-analyzed in the Analysis trap. This last step also marks the first one in the next cycle, beginning from the top.

of the Larmor-particle, it is parked as short as possible in the PT and then transported back to the AT [56]. While the Larmor-particle is moved back to the AT, the Cyclotron-particle is transported from the Park trap to the PT and the cyclotron frequency $\nu_{\mathrm{c,PT,2}}$ is measured again. Afterward, the cycle starts again with a spin-state analysis in order to identify if the applied rf-drive in the PT has flipped the spin of the Larmor-particle, and initializes the spin for the next cycle.

With this newly developed measurement scheme, it was possible to determine the antiproton magnetic moment with a fractional precision of 1.7 p.p.b. [58]. Compared to the double-trap method, where only one particle is used for the measurement, the usage of two particles induces some new systematics shift on the g-factor. As the Cyclotron-particle has a much higher temperature $T_{+,\mathrm{C}}$ than the Larmor-particle $T_{+,\mathrm{L}}$, the resulting

temperature difference of $\Delta T_+ = T_{+,\mathrm{C}} - T_{+,\mathrm{L}} \approx 356(27)\,\mathrm{K}$ leads to a g-factor shift within the residual magnetic field gradients present in the PT of $B_{1,\mathrm{PT}} = 71.2(4)\,\mathrm{mT/m}$ and $B_{2,\mathrm{PT}} = 2.7(3)\,\mathrm{mT/m^2}$. The imposed shift is $(\Delta g/g)_{B_1} = 0.22(2)\,\mathrm{p.p.b.}$ and $(\Delta g/g)_{B_2} = 0.11(1)\,\mathrm{p.p.b.}$, respectively [56]. The dominant systematic uncertainty stems from a possible temperature fluctuation of the axial detection system T_z during irradiation with the spin-flip drive $\nu_{\mathrm{rf,PT}}$, which alters the magnetic field experienced by the Larmor-particle relative to the Cyclotron-particle due to the residual magnetic bottle $B_{2,\mathrm{PT}}$ in the PT. This axial temperature difference $\Delta T_\mathrm{z} = 0.68(7)\,\mathrm{K}$ leads to an uncertainty of $0.97(7)\,\mathrm{p.p.b.}$ [56]. To mitigate these effects, magnetic shielding and shimming systems were installed in the experimental setup in order to shim the residual $B_{1,\mathrm{PT}}$ and $B_{2,\mathrm{PT}}$ out. More details can be found in the PhD thesis of Stefan Erlewein [86].

Nevertheless, the main contribution to the final uncertainty of the 2017 antiproton g-factor measurement is the statistical uncertainty of 1.1 p.p.b., mainly imposed by the long re-cooling times of the Larmor-particle. One measurement cycle with the two-particle method takes about 40 min, and imposes a mean fluctuation rate of $\Delta T_{+,\mathrm{L}} = 17\,\mathrm{mK}$ per cycle, enabling the measurement of about 75 cycles before re-cooling is necessary again, resulting in about 50 h of measurement time followed by 48 h of cooling time.

In order to reduce the required cooling time a dedicated Cooling trap, originally proposed in the BASE technical design report [137], was implemented in trap stack together with improved cyclotron detectors [89] developed within the PhD of Markus Fleck [90]. The next section describes the commissioning and characterization of the new particle cooling procedure resulting in a cold particle preparation time of about 8 min.

4.2 Order of magnitude improved cyclotron mode cooling

As mentioned in Section 4.1, sub-thermal cooling is widely used in g-factor measurements of protons and antiprotons [56, 57, 135, 138] to reduce the particle's cyclotron temperature T_+ and is thus essential in reaching high-precision. Here, the long re-cooling times of the modified cyclotron mode result in long sampling times of multiple hours [56], and thus in an overall dominant statistical uncertainty [56, 139]. To decrease the cooling time in future g-factor measurements, we have built a novel Cooling trap (CT), developed for strong particle-detector interaction, and an improved cyclotron detection system [90], and time-optimized every step in the sub-thermal cooling procedure. With this, the preparation time for a cyclotron cold particle is reduced by about a factor of 100 and enables the detection of single spin transitions with a mean error rate of $E_s < 0.000\,023$, more than three orders of magnitude better than in [41]. These results were published in Phys. Rev. Lett. [63], where the author of this thesis contributed to the characterization of the setup, which is summarized in the following.

4.2.1 Setup

The principle of the sub-thermal cooling routine is based on the principle of resistively cooling a particle's eigenmode when it is interacting with a tuned circuit with a similar resonance frequency [140] (see Chapter 2.2), and then decoupling it again [70]. To utilize this principle a cooling resistor is needed, as well as a detection system to monitor changes in the respective mode energy E_i of the particle, where i refers to the three eigenmodes (Chapter 2.1.1). As this procedure is referred to as 'cooling', i.e. reducing energy, the term temperature T is also often used instead of the mode energy of the particle E_i and corresponds to $T_i = E_i/k_\mathrm{B}$.

In the presented results, the sub-thermal cooling setup consists of two Penning traps, the AT and the CT, and their corresponding detection systems [41, 88, 90]. The AT and CT are part of the BASE trap stack [141] (Chapter 3.2.4), which is placed in its own vacuum chamber, the trap can. More details on the complete experimental setup can be found in Chapter 3.

Figure 4.5 shows a schematic drawing of the setup. The AT and CT are placed adjacent to each other, with a distance of 21 mm between both central electrodes. Connected to the

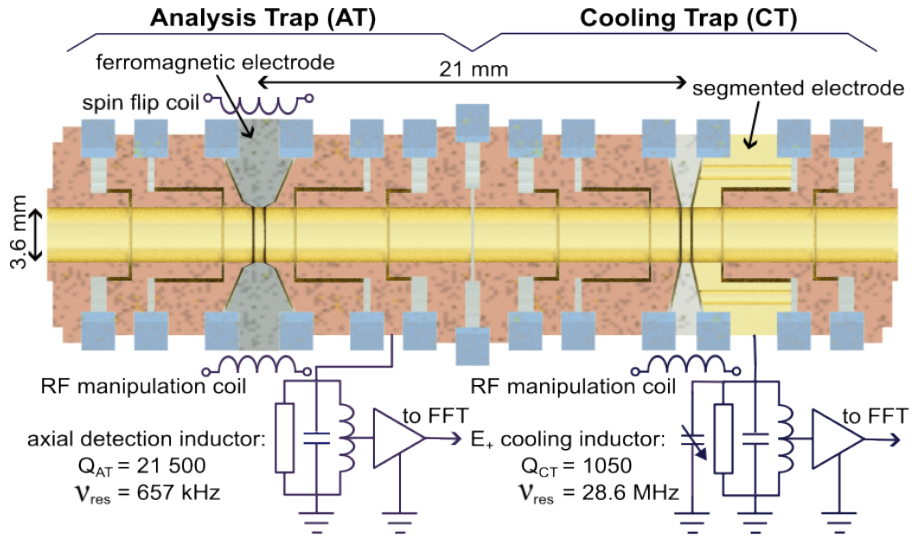

Figure 4.5: Setup for the sub-thermal cooling procedure. Essential is the optimized Cooling trap with its cyclotron detection system to efficiently cool the cyclotron mode of the stored particle. In order to read out the change in cyclotron energy, the Analysis trap with its strong magnetic bottle (Figure 4.6) is used. The quadratic magnetic field inhomogeneity B_2 introduces an axial frequency shift with a change in cyclotron energy of the particle, which can be read out using the axial resonator coupled to the analysis trap. Adapted from [63].

AT is an axial detection system [88] including a feedback loop [94] (see also Chapter 2.2 and Chapter 3.2.6) in order to read-out the axial frequency of a trapped particle $\nu_{\mathrm{z,AT}}$ [68]. The resonator has a resonance frequency $\nu_{\mathrm{res,AT}} \approx 658\,\mathrm{kHz}$, a Q-value $Q_{\mathrm{AT}} \approx 21\,500$, an inductance $L_{\mathrm{AT}} \approx 1.7\,\mathrm{mH}$ and a signal-to-noise ratio of 27 dB [88]. Additionally, the AT is equipped with a ferromagnetic ring electrode in order to generate a magnetic field $B(z) = B_0 + B_2 z^2$ with a superimposed magnetic bottle of the strength B_2. In such a magnetic bottle the orbital magnetic moment $\mu_+ = \frac{q}{m}\frac{E_+}{\omega_+}$ of the modified cyclotron frequency couples to the axial frequency ν_{z}, which becomes dependent on the cyclotron energy of the particle E_+ [70]

$$\nu_{\mathrm{z,AT}} = \nu_{\mathrm{z,0,AT}} + \frac{1}{4\pi^2 m \nu_{\mathrm{z,0,AT}}} \frac{B_{2,\mathrm{AT}}}{B_{0,\mathrm{AT}}} E_+, \tag{4.6}$$

where $\nu_{\mathrm{z,0,AT}} \approx 657.92(1)\,\mathrm{kHz}$.

Figure 4.6 shows the magnetic field in the center of the AT as a function of the particle position in z-direction, determining the magnetic bottle strength B_2 and its center in order to suppress systematic frequency shifts [138]. To do so, the modified cyclotron frequency is measured as a function of an offset voltage applied to one correction electrode. This

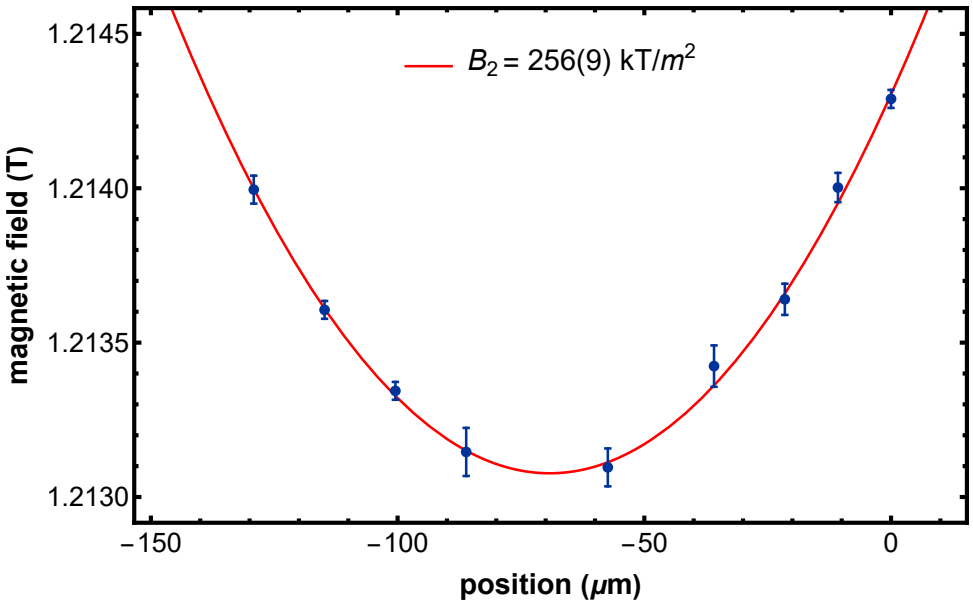

Figure 4.6: Magnetic field in the center of the Analysis trap. From this measurement we can extract a quadratic magnetic field contribution of $B_2 = 256(9)\,\mathrm{kT/m^2}$.

changes the particle's axial position by $1.435\,\mu\mathrm{m/mV}$, which can be analytically calculated by the geometry of the trap. In each offset-point, the modified cyclotron frequency is excited by a radial excitation drive. The excitation frequency is swept in a range of 20 kHz in steps of 2 kHz for 10 s at a drive strength of -15 dB seven times per step. Before and after every irradiation the axial frequency is measured. When the drive frequency is resonant with the modified cyclotron frequency of the particle, its cyclotron energy increases E_+ and according to Equation (4.6) results in an axial frequency shift $\Delta\nu_z$. Fitting a quadratic function to the data results in a magnetic bottle strength of $B_2 = 256(9)\,\mathrm{kT/m^2}$ and a homogeneous magnetic field of $B_{0,\mathrm{AT}} = 1.213(1)\,\mathrm{T}$, and yields the geometrical center of the magnetic bottle. With this measurement, we determine the center of the magnetic bottle with a resolution of $\sim 1\,\mathrm{kHz}$, which is sufficient compared to the line width of $\sim 10\,\mathrm{kHz}$ in the AT [138]. A more accurate determination of the magnetic bottle strength B_2 can be extracted from single spin-flip measurement (Section 4.2.3) and gives a value of $B_{2,\mathrm{AT}} = 266(8)\,\mathrm{kT/m^2}$, which is in a 2σ agreement with the one determined using cyclotron frequency measurements. Inserting this value in Equation (4.6), a cyclotron temperature change of $\Delta T_+ = 1\,\mathrm{K}$ corresponds to a frequency shift of $\Delta\nu_z = 69.7(5)\,\mathrm{Hz}$, or in other words, to an E_+ resolution of 14.7 mHz, or $1.2\,\mu\mathrm{eV}$ per $\Delta\nu_{z,\mathrm{AT}} = 1\,\mathrm{Hz}$ axial frequency shift.

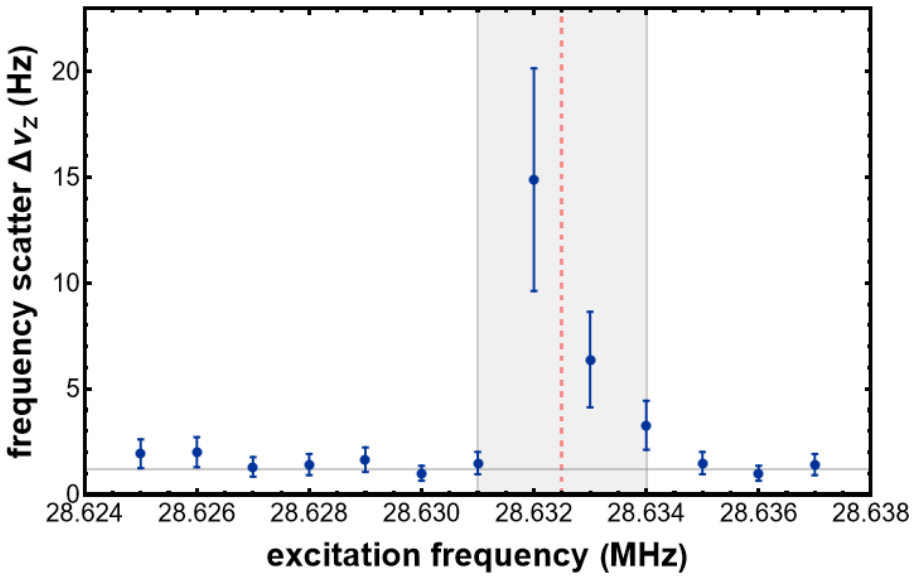

Figure 4.7: Cyclotron frequency resonance of the particle parked in the segmented electrode in the CT. One point represents the mean of the axial scatter $\Delta\nu_{z,AT}$ induced by a cyclotron excitation sweep in a span of 2 kHz in the CT. With this we determine the cyclotron frequency of the particle in the CT $\nu_{+,CT} = 28.6325(15)$ MHz (red dashed line) with the uncertainty corresponding to the width of the resonance (gray area).

Adjacent to the AT is the CT, with a tunable cyclotron detection system [89, 90] connected to its segmented electrode (see Figure 4.5). It has a resonance frequency $\nu_{\mathrm{res,CT}} \approx 26.1\,\mathrm{MHz}$ with a tuning range of 4.5 MHz and a Q-value of $Q = 1050(50)$ when connected to the CT. For better temperature thermalization and for a reduction of parasitic capacitance, the cyclotron detector is placed inside the trap can, whereas the axial detection systems of the other traps are placed in a separate segment of the cryogenic stage next to the trap can (Chapter 3.2.1). To cool the trapped particle with the resonator, it has to be tuned to the particle's modified cyclotron frequency $\nu_{+,\mathrm{CT}}$ in the segmented electrode of the CT. For this, we perform a cyclotron resonance scan as was done in the AT to determine the magnetic bottle shape. First, we detune the cyclotron resonator and measure the axial frequency of the particle $\nu_{\mathrm{z,AT}}$ in the AT. Then we transport it to the CT and radiate a cyclotron excitation drive $\nu_{\mathrm{rf,CT}}$ and subsequently transport the particle back to the AT, where its axial frequency is measured again. This is done multiple times for excitation drive sweeps from $(28.8625 - 28.6238)\,\mathrm{MHz}$ in steps of 1 kHz for 1 s. When the excitation drive is on resonance with the particle's modified cyclotron frequency $\nu_{+,\mathrm{CT}}$, it will increase its cyclotron energy and therefore induce an axial frequency shift $\Delta\nu_{\mathrm{z,AT}}$ in the AT (Equation (4.6)). Figure 4.7 depicts the recorded cyclotron frequency resonance curve. A steep rise in the scatter is visible close to the modified cyclotron frequency of the particle with a slow decrease. This reflects the Boltzmann-distributed temperature $T_{\mathrm{z,AT}}$ of the axial detection system together with the strong magnetic bottle [133]. From this measurement a modified cyclotron frequency of $\nu_{+,\mathrm{CT}} = 28.6325(15)\,\mathrm{MHz}$ of a particle in the CT is obtained, and the resonance frequency of the detector $\nu_{\mathrm{res,CT}}$ can be tuned accordingly. It should be noted that the 3dB-width of the cyclotron detector is $\sim 25\,\mathrm{kHz}$ resulting in a well-tuned resonator compared to the resolution of the modified frequency estimation.

The interaction time constant of a particle with a resonator tuned to one of its eigenfrequencies is described by [68]

$$\tau_{+,\mathrm{CT,th}} = \frac{m}{R_p}\left(\frac{D_{+.\mathrm{eff}}}{q}\right)^2 \tag{4.7}$$

where m is the mass and q the charge of the particle, $D_{+.\mathrm{eff}} = 4.82\,\mathrm{mm}$ is the effective pick-up length [79]. The parallel resistance R_p of the resonator is given by $R_p = 2\pi\nu_{+,\mathrm{CT}}\,QL \approx 340\,\mathrm{k\Omega}$ with the resonators inductance $L \approx 1.73(3)\,\mu\mathrm{H}$. This leads to a theoretical cooling-time-constant of $\tau_{+,\mathrm{CT,th}} = 4.5(2)\,\mathrm{s}$, which is 20 times faster than in other state-of-the-art

Penning trap experiments [57, 85, 142] and corresponds to an about 100-fold reduction compared to previous measurements conducted in BASE [55, 56].

4.2.2 Cooling protocol

To achieve sub-thermal temperatures, we follow a specific protocol, outlined in Figure 4.8. Prior to initiating the sequence, a single particle is moved to the AT and magnetron cooled to a temperature $T_- = E_-/k_\mathrm{B} = 7(1)\,\mathrm{mK}$ by sideband-coupling (Chapter 2.2.3) the magnetron to the axial mode and letting the particle interact with a feedback-cooled resonator (Chapter 2.2.2). The time optimization of each step is crucial for the efficient execution of a rapid cooling routine, including the frequency read-out, transport time, and thermalization time in the CT, as well as the physical temperature of the cyclotron resonator.

For this reason, we have developed a fast frequency determination algorithm with high cyclotron energy E_+ resolution. First, we take an FFT-spectrum of the resonator without the particle in a frequency span of 800 Hz, which corresponds to a cyclotron temperature range T_+ of ≈12 K. Next, this reference spectrum is subtracted from spectra with particle signatures [68]. A particle is then visible on the subtracted spectrum as a peak at its corresponding frequency. To distinguish between particle signatures and noise peaks, only peaks above a certain threshold are accepted. During the execution of the cooling protocol, the trap parameters are tuned so that a cold particle lies within the 3 dB range of the resonator. With this, particles with cyclotron temperatures $T_+ < 440\,\mathrm{mK}$ can be detected at an averaging time of ≈ 10 s with a significance of 2σ.

After recording a reference spectrum, the cooling protocol starts by transporting the particle from the AT to the CT. This is done by applying voltage ramps to the 10 connecting electrodes. One transport takes 4.8 s limited by the time constants of the filters connecting the power supply to the electrodes, and induces a scatter of 14(2) cyclotron quanta, as can be seen in Figure 4.8 b). This results in a background temperature fluctuation of 18 mK (≈ 1.2 Hz), which is negligible compared to the several 100 Hz that have to be resolved in order to detect particles with different cyclotron temperature T_+. In the CT the particle is parked for a time τ_th during which it interacts with the cyclotron resonator tuned to the particle's modified cyclotron frequency (see Section 4.2.1). Afterward, the particle is transported back to the AT to measure its axial frequency and therefore its change in cyclotron energy E_+. This cycle is repeated until the particle's frequency is

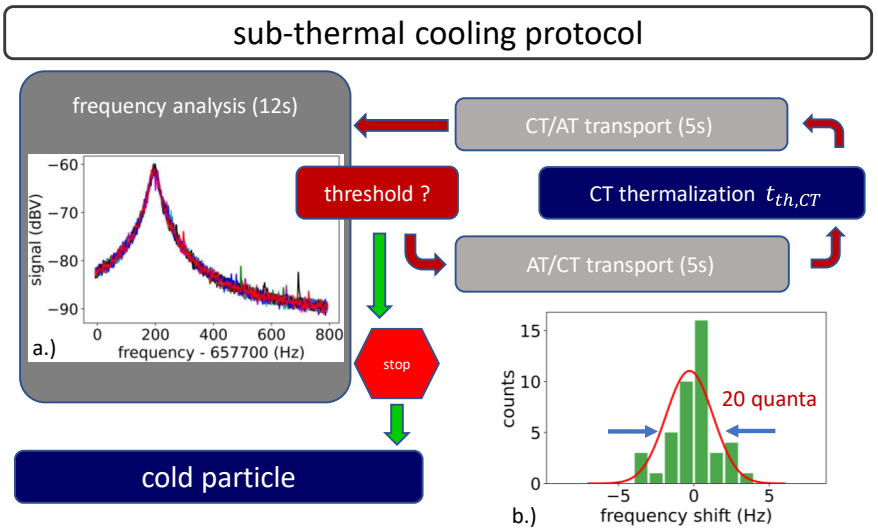

Figure 4.8: Visualization of the sub-thermal cooling protocol. For details see text. Adapted from [63].

under a set threshold. Then the measurement cycle stops, and a cyclotron cold particle is prepared.

When the particle is parked in the CT, it interacts with the cold resistor $R_{p,\mathrm{CT}}$ of the connected cyclotron detector, which results in a random walk of the particle's modified cyclotron energy E_+ [68, 70]. Once the particle is shuttled back to the AT it loses contact with the thermal bath of $R_{p,\mathrm{CT}}$ and the modified cyclotron energy of the particle "freezes" $E_{+,k}$. Arriving in the AT the imprinted modified cyclotron energy $E_{+,k}$ can be read out using Equation (4.6). To evaluate the mean temperature of the particle's modified cyclotron mode after thermalization in the CT, we first identify the lowest observed axial frequency ν_{z,k^*}. Then we convert the frequency shift $\Delta\nu_{\mathrm{z},k} = \nu_{\mathrm{z},k} - \nu_{\mathrm{z},k^*}$ to an absolute temperature T_+ using the strength of the magnetic bottle $B_2 = 266(8)\,\mathrm{kT/m^2}$. With this, we also infer the temperature of the thermalization resistor $R_{p,\mathrm{CT}}$. To do so, we have used the above described protocol with a particle thermalization time $\tau_{th,\mathrm{CT}} = 20\,\mathrm{s}$. Figure 4.9 a) shows the measured axial frequencies $\nu_{\mathrm{z},k}$ referenced to the measurement with the lowest frequency $\nu_{\mathrm{z},0,\mathrm{AT}}$. These data are described by a truncated Boltzmann distribution of a weakly bound one-dimensional thermal oscillator of $\approx 4\,\mathrm{K}$ [70, 133]. To determine the temperature, we then find the amount of measured events N_j in temperature

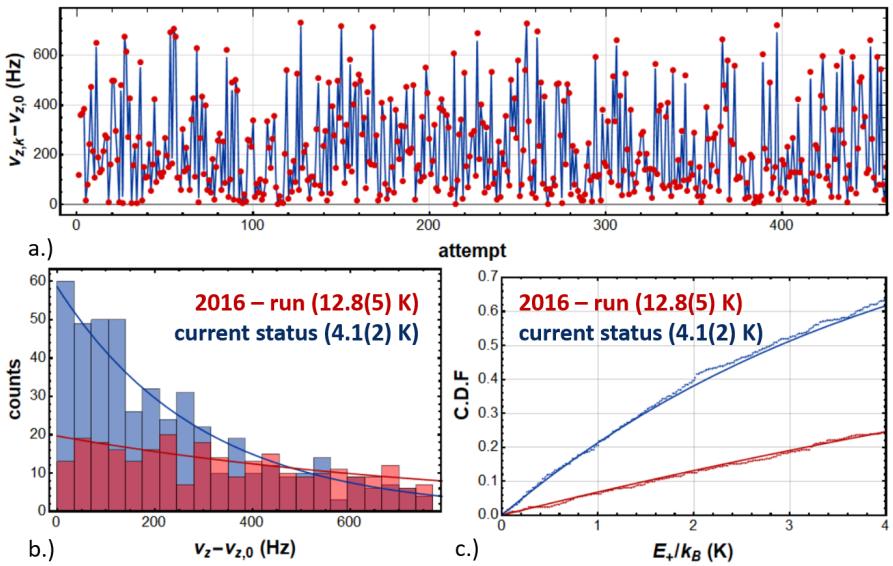

Figure 4.9: a) Frequency measurements in the AT with thermalization in the CT in between data points, as described in the text. b) Histogram of the data in a) is displayed in blue. For comparison data from the previous g-factor measurement campaign, [56] is plotted in red. c) Cumulative density function of the data shown in a) and b). From a fit the CT resonator temperature $T_{+,\mathrm{CT}} = 4.1(2)\,\mathrm{K}$ is extracted. Adapted from [63].

steps of $\Delta T_+ = 0.001\,\mathrm{K}$ and evaluate the normalized cumulative density function

$$\mathrm{CDF}(T_{\mathrm{thr}}) = \frac{1}{N} \sum_{j}^{N(T_{\mathrm{thr}})} N_j(\Delta T_+), \tag{4.8}$$

where N is the total number of conducted thermalization cycles and the upper index $N(T_{\mathrm{thr}})$ is the number of events until a defined threshold temperature T_{thr}. Next, the thermal cumulative density function

$$\mathrm{CDF}(T_{+,\mathrm{CT}}) = 1 - \exp(-T/T_{+,\mathrm{CT}}) \tag{4.9}$$

is fitted to the data and the cyclotron detector temperature $T_{+,\mathrm{CT}} = 4.1(2)\,\mathrm{K}$ is extracted.

Figure 4.9 b) and c) show the temperature binned data from Figure 4.9 a) in blue as a histogram and CDF, respectively. The red data corresponds to a measurement conducted with the apparatus as used in the last g-factor run [56] (Section 4.1.3), where the cyclotron detection temperature was $T_{+,\mathrm{PT}} = 12.8(5)\,\mathrm{K}$. The three times reduced temperature of the cyclotron cooling resonator can be explained by the relocation of the newly developed

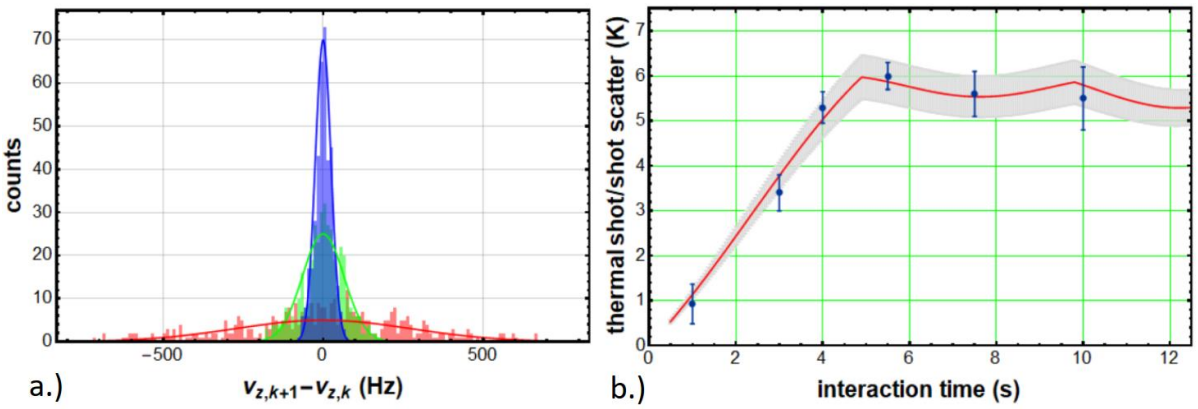

Figure 4.10: a) Histograms of frequency shift $\Delta\nu_{z,AT,k} = \nu_{z,AT,k+1} - \nu_{z,AT,k}$ for different CT cyclotron detector interaction times τ_{th}: blue 0.5 s, green 3 s and red 15 s. b) Width of histograms like in a) as a function of the interaction time τ_{th} in the CT. Taken from [63].

CT cyclotron detector [90] inside the trap can, which acts as a cryogenic shield, and puts the resonator closer to the trap, reducing wire length and parasitic capacitance. Thanks to the CT, the reduced cyclotron detection temperature, and the optimized transport time, the acquisition of the data set shown in Figure 4.9 takes 3.7 h at fully optimized parameters, whereas it took 55 h for the red data set.

To determine the optimal thermalization time of the particle with the cyclotron detector in the CT, we park the particle for different thermalization times τ_{th} in the CT. We measure the axial frequency in the AT before the thermalization $\nu_{z,AT,k}$ and afterward $\nu_{z,AT,k+1}$. Figure 4.10 a) shows this frequency scatter for different interaction times. It increases linear with increasing interaction time τ_{th} until the correlation time $\tau_{+,CT}$ is reached. From then onward, the width of the measured histograms converges to a mean value, which is weakly structured by the correlation time $\tau_{+,CT}$, illustrated in Figure 4.10 b). Here, the particle is parked in the segmented electrode, the closest possible position between the particle and detector, providing the strongest particle-detector coupling. From these measurements we extract a correlation time between particle and cyclotron detector of $\tau_{+,CT} = 4.7(4)$ s which is in perfect agreement within the uncertainties with the theoretical value of $\tau_{+,CT,th} = 4.5(2)$ s,

In summary, the newly implemented CT with its cyclotron detector and the frequency read-out in the AT provides fast and reliable cooling of the modified cyclotron mode and is easy to implement in an existing Penning trap stack. One cycle of the cooling protocol is accomplished in about 27 s (see Table 4.1) compared to 820 s in the 2017 g-factor

step	time (s)
frequency read-out	12
transport (AT - CT)	4.8
CT thermalization	4.7
transport (CT - AT)	4.8
total	26.3

Table 4.1: Time consumption for each step in the sub-thermal cooling protocol.

campaign [56]. Overall, this leads to a preparation time of a cold proton or antiproton with a modified cyclotron temperature $T_+ < 200\,\mathrm{mK}$ of $\approx 500\,\mathrm{s}$ and is therefore about $100\times$ faster than in the previous measurement [56]. Figure 4.11 illustrates the difference in cooling time needed to reach a specific temperature, comparing the 2017 antiproton g-factor run (red) [56] and what is achieved now (blue).

4.2.3 Impact on the spin-state initialization/g-factor measurement

To demonstrate the importance of the new sub-thermal cooling device, we have recorded non-destructive high-fidelity spin quantum jump spectroscopy. This is done as explained in Section 4.1. Utilizing the magnetic bottle B_2 in the AT, the spin magnetic moment of the trapped particle is coupled to its axial frequency due to the continuous Stern-Gerlach effect

$$\Delta\nu_{\mathrm{z,SF}} = \frac{gh\nu_+ B_2}{4\pi^2 m\,\nu_{\mathrm{z,0,AT}},\, B_0} \tag{4.10}$$

and induces an axial frequency shift of $\Delta\nu_{\mathrm{z,SF}} = 173(5)\,\mathrm{mHz}$ in the AT. As mentioned above, noise densities on the trap electrodes can drive cyclotron quantum transitions leading to a frequency shift $\Delta\nu_{\mathrm{z},+} = \pm 65\,\mathrm{mHz}$. These induced frequency fluctuations thus lead to considerable mean error rates E_S in the spin-state determination. As the cyclotron transition rate $dn_+/dt \propto E_+$ (Equation (4.3)) [122], the contrast in the spin-state identification increases for cyclotron cold particles [95].

Using the novel sub-thermal cooling device, we prepare an antiproton with a cyclotron temperature $T_+ < 100\,\mathrm{mK}$, which is now possible in under 20 min. Then, we measure the axial frequency of the particle interleaved with the irradiation of an rf-drive to flip the antiproton's spin. Figure 4.12 shows the result of such a measurement. In the upper

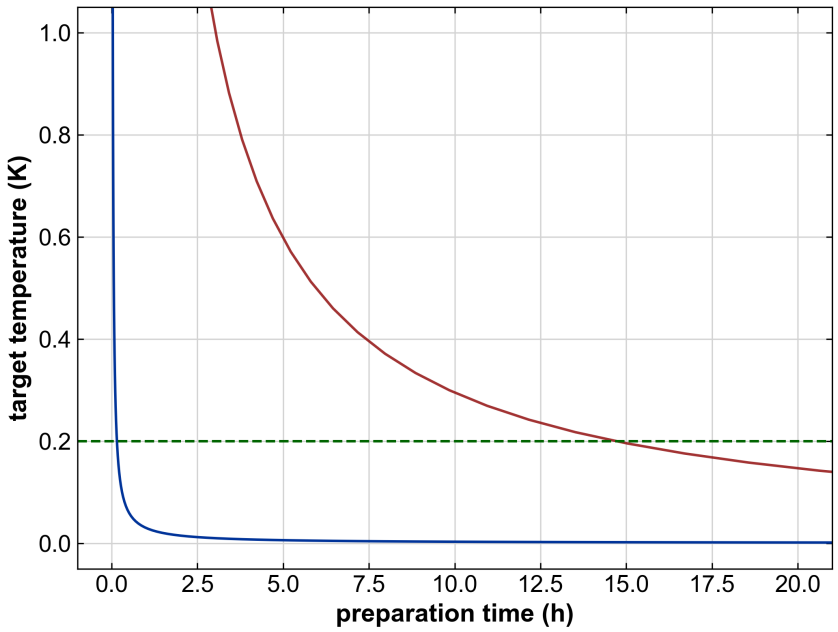

Figure 4.11: Comparison of the cooling time with the 2017 setup [56] in red and the results presented here [63] in blue. The green dashed line denotes the 200 mK threshold.

plot, the axial frequency $\nu_{z,k}$, referenced to the first measurement in the sequence $\nu_{z,0}$, is plotted. Here, the two spin-states $|\uparrow\rangle$ and $|\downarrow\rangle$ are clearly distinguishable. The lower plot shows a histogram of the consecutive axial frequency shift $\nu_{z,k+1} - \nu_{z,k}$. The outer sub-histograms at $\Delta\nu_z = \pm 173(1)$ mHz represent the spin transition from $|\uparrow\rangle \rightarrow |\downarrow\rangle$ and $|\downarrow\rangle \rightarrow |\uparrow\rangle$. For the central histogram, no spin-flip occurred. The width of the histogram of $\sigma(\Delta\nu_z) = 21(1)$ mHz is consistent with frequency measurement noise resulting from the power supply and the detection system. The resulting error rate is $E_S = 2.3 \times 10^{-5}$ and therefore > 1500 times better than the previously recorded error rates [41], which is already visible when comparing to the best resolution in 2017 in Figure 4.1.

With this novel device, we are able to cool the modified cyclotron mode of a single particle almost 100× faster than in the previous magnetic moment measurement [56, 57] with a significantly lower spin-state identification error rate. This paves the way for an improved antiproton magnetic moment measurement with a fractional precision of about 100 p.p.t., together with other experimental upgrades like the improved shielding and shimming system [86]. Moreover, such a device provides the pathway towards the direct measurement of the nuclear magnetic moment of heavier nuclei, like $^3He^{2+}$, which would establish a new absolute magnetometry standard [139]. Additionally, it could be applied

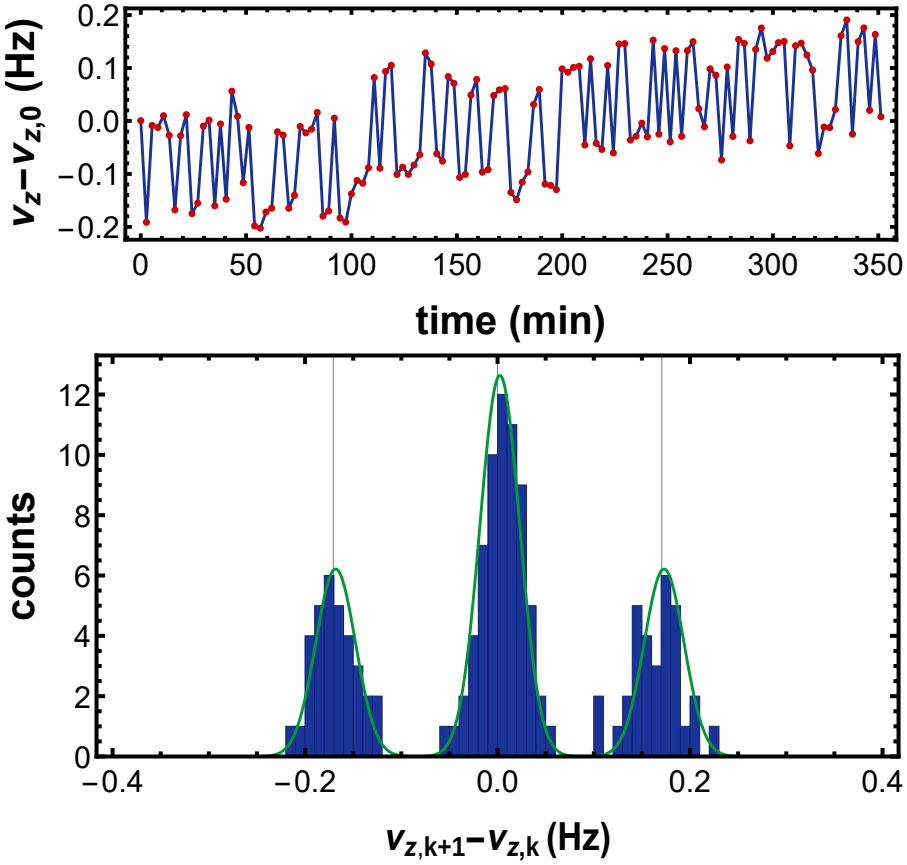

Figure 4.12: Spin-flip resolution of a single antiproton using the new sub-thermal cooling device. Upper plot: Axial frequency measurements interleaved with the irradiation of a spin-flip drive, referenced to the first measurement in the sequence. The two spin-states are clearly distinguishable. Lower plot: Histogram of the frequency shifts in the upper plot. Three distributions are well separated. The central one corresponds to the frequency shift, where no spin-flip occurred. The left one shows events, where the spin was flipped from $|\uparrow\rangle \rightarrow |\downarrow\rangle$ and the right from $|\downarrow\rangle \rightarrow |\uparrow\rangle$. Adapted from [63].

in experiments using coherent measurements of the cyclotron frequencies in high-precision mass spectrometry and measurements of the bound electron g-factor [85, 143], as here sideband-cooling is used to re-cool the particle, which is inducing phase scatter. This could be reduced with the usage of a distinctive sub-thermal cooling device, as presented here.

Chapter 5

The Reservoir trap and antiproton catching

The Reservoir trap (RT) [118] is the most upstream trap in the BASE trap stack. We use it to catch antiprotons, clean them from contaminants, and store them long term to extract single particles for high-precision measurements of the antiproton charge-to-mass ratio and the antiproton magnetic moment [55, 95, 118]. It is especially important because we need to perform these high-precision measurements during the shutdown of the CERN accelerators (YETS), where no antiprotons are available anymore, so the stored antiproton cloud in the RT enables us to perform high-precision measurements undisturbed by fields of the running decelerator.

The maintenance of the stored particles in the RT, the reservoir, is therefore critically important. This means regular cooling and cleaning of the particles to enable long storage without any losses. Additionally, protection against power cuts is implemented by a network of uninterruptible power supplies. With this safeguarding, we can store an antiproton cloud for over a year. This enables us to set new limits on the direct measurement of the antiproton lifetime (see Chapter 6).

5.1 The Reservoir trap

The RT is a five-pole cylindrical Penning trap [78] in compensated and orthogonal design, equipped with a resonant superconducting LC circuit used to detect the axial motion of the trapped particles. Figure 5.1 shows a scheme of the RT with all its electronic connections during regular operation. While catching antiprotons, different power supplies

are connected to supply the needed high-voltage (HV), which is discussed in detail in Section 5.2.

At the top of Figure 5.1 the trap electrodes of the RT and the HV-electrodes, needed to catch antiprotons, are shown. The trap electrodes are labeled with R0X, where X is an index increasing from left to right. The upstream (US) HV-electrode is called HVP, where the P stands for pulse, as the voltage on the electrode is quickly ramped up and down during catching. The downstream (DS) HV-electrode is called HVS, the S standing for static, as this electrode is supplied with a constant voltage, which is not varied during catching. Additional electrodes used for transport are depicted with TX, where X is, once again, a number counting the electrodes from US to DS. All trap electrodes are separated by sapphire rings.

The trap system is maintained within a cryogenic environment. Figure 5.1 illustrates the electronic setup, starting from the 4 K stage (yellow background), where the trap electrodes are located, passing through the pin-base region (brown), which routes the cables out of the trap area, and continuing to the 77 K stage (green background). Finally, the connections reach room temperature (300 K – white background), where they interface with power supplies and frequency generators. For more details of the cryogenic setup, the reader is referred to Chapter 3.2.1.

Figure 5.1 also depicts all cables going from the trap toward their respective power supplies and frequency generators. The four different types of connections are the DC biasing lines for the electrodes (black), high-voltage (HV)-lines (green) needed to catch the antiprotons, the axial (orange) and radial (blue) excitation lines, and the detection readout (purple). The different lines are explained in more detail in the following.

The trap electrodes are biased (when not indicated otherwise) by the ultra-stable precision power supply UM 1-14 from Stahl Electronics [124]. The biasing lines are all filtered with four RC low pass filters (in case of T01 only three filters) with a cut-off frequency of about 30 Hz. They are built using 10 nF NP0 ceramic capacitors and 500 kΩ resistors, where always two 1 MΩ resistors are connected in parallel as a safeguard in case one breaks. We typically implement four filter stages in order to have a higher noise suppression, because noise, in the form of RF-pick-ups and electromagnetic interferences, can lead to a temperature increase of the detectors, and thus to unwanted heating of the trapped particles. All electrode bias lines except for the ring and correction electrodes have an additional relay switch on the room temperature side, grounding the electrodes when not needed, e.g., for transporting or extracting single antiprotons. The UM 1-14

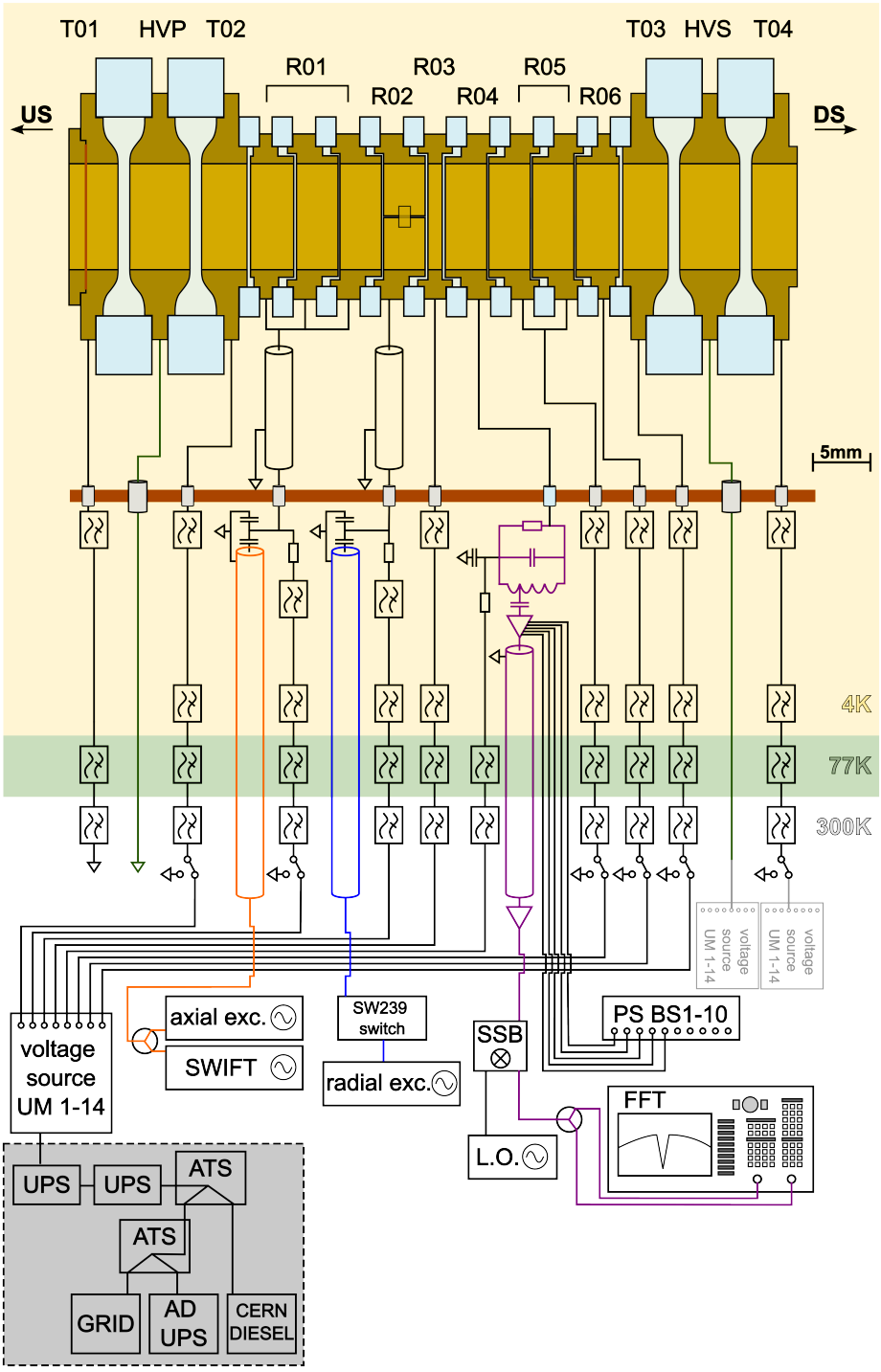

Figure 5.1: RT electronics during regular operation. For details see text.

electrode	R01	R02	R03	R04	R05	R06
voltage (V)	0	6.4035	7.2726	6.4035	0	0

Table 5.1: Voltage applied to the RT electrodes during regular operation. The applied ring voltage to electrode R03 corresponds to an axial frequency of 801 812 Hz.

power supply has two modes, the so-called fast and precision mode, with voltage precision of $\approx 1\,\mathrm{mV}$ and $1 \times 10^{-6}\,\mathrm{V}$, respectively. In the fast mode, voltages in the range of $-14\,\mathrm{V}$ to $14\,\mathrm{V}$ can be applied, whereas the precision mode is unipolar. The fast mode is used for particle shuttling as well as for particle extraction (Section 5.4). Typical voltages applied to the electrodes during normal operation are summarized in Table 5.1.

The high-voltage lines are marked in green and are tested to supply voltages up to 4.5 kV, normally operated only up to 2 kV. For these lines caution in the implementation is necessary in order to avoid sparking and crosstalk with the rest of the apparatus. Therefore, they are supplied via a wire inside a grounded stainless steel tube and have a screw connector on the feedthrough flange (brown bar in Figure 5.1) that can hold up to 20 keV. During normal operation, both high-voltage electrodes, HVP on the upstream side and HVS on the downstream side, are grounded. For the currently ongoing g-factor campaign, HVS is used as a park trap and is therefore also connected to a UM 1-14 power supply.

Another special type of electrode lines are the excitation lines marked in orange (axial) and blue (radial). Here, the rf-signal for the excitation is overlaid with the DC trap biasing signal inside the trap can and implemented as a coaxial cable, where the shield is grounded to the feedthrough flange. After the feedthrough flange, the RF and DC lines split. This is realized by putting a capacitive voltage divider to suppress DC-current in the rf-line, and additionally, a $1\,\mathrm{M}\Omega$ resistor is placed between the voltage divider and the lowpass filters of the biasing line, in order to block the AC-signal from the RF-line flowing back to the DC-biasing line. The axial excitation line (orange) is connected to the endcap electrode R01 and is split again at room temperature. It is connected to a frequency generator for axial excitation and one for supplying the SWIFT cleaning (see Section 5.3). The radial line (blue) is connected to the segmented correction electrode R02. This enables the application of a quadrupole excitation by applying an rf-signal to one half of the electrode. The two half-electrodes are connected by a $10\,\mathrm{M}\Omega$ block resistor, allowing to bias both segments with the same DC line. On the room temperature side,

the radial line is connected to a switch (SW239) and then to a frequency generator. The additional switch is necessary to avoid excitation of the trapped particles while applying a magnetron sideband drive, as described in Chapter 2.2.3. The frequency generator produces an output signal spike when turned on. As the magnetron sideband frequency is close to the axial frequency, the output spike can excite the ultra-sensitive axial detector and thus the axial motion of the particles.

The third special electrode line is the detection pick-up line (purple). Here, the electrode is biased through the axial resonator [88] (see Chapter 2.2). On the room temperature side, the amplified detection signal is downconverted by a single sideband (SSB) downconverter and then fed into an FFT analyzer (SR 780). For the RT operation, we currently split the detection signal and record FFT spectra using both channels of the FFT analyzer, one in a small frequency range for good dip detection (200 Hz) and one with the whole resonator visible (3200 kHz) in order to monitor potential noise problems. Note that the detection pick-up line is connected to the correction electrode R04 on the opposite side of the excitation line to avoid crosstalk.

To safeguard the antiprotons against a power cut, a multiple-stage power failure net was established, shown in Figure 5.1 in the gray box. The electrode biasing voltage source UM 1-14 is linked to two UPS batteries connected in series. These batteries are connected to an automatic transfer switch (ATS), switching between the AD power supply and CERN's Diesel generator. The AD power supply also switches between the normal power grid and the uninterruptible power supply (UPS) of the AMF. With this safety net, we have survived all power cuts so far.

5.2 Antiproton catching

While precision measurements are running, the BASE experiment disconnects unused equipment in order to minimize noise from the power grid of the accelerator hall. This also includes hardware needed for catching. This section first describes the hardware changes implemented to prepare the experiment for taking beam and also outlines the antiproton catching process.

Figure 5.2 shows a top view of the BASE experiment, highlighting the equipment needed for antiproton catching. It depicts the superconducting magnet with the trap stack, enclosed by its own vacuum chamber named the trap can, and the support structure inside the magnet. A degrader is installed upstream of the trap stack to reduce the

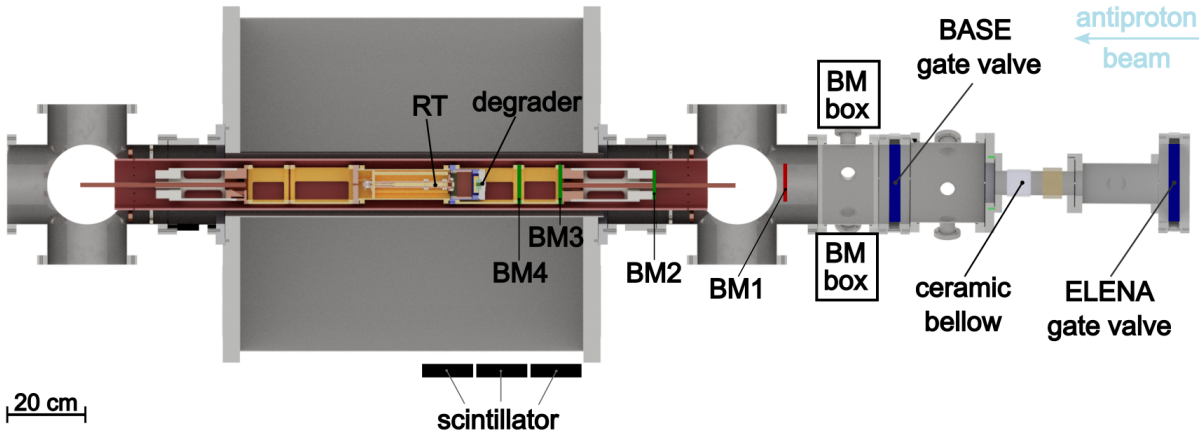

Figure 5.2: Top view of parts of the experiment and the beamline with all important instruments for catching labeled. To monitor the position of the beam, four beam monitors (BM) are installed in the system. Three are positioned on the electronics and support system of the trap at the 4 K stage (green) and one on the 77 K stage (red). To monitor the annihilation location of the antiproton beam, scintillators are placed next to the magnet at the same level as the most downstream beam monitors, the degrader, and the center of the RT.

energy of the incoming antiprotons (Chapter 3.2.3) [115]. Following the BASE beamline upstream, four beam monitors are installed (Chapter 3.2.2), which are important for beam steering. Between the transfer line coming from ELENA (from here on referred to as ELENA beamline) and the BASE experiment, two gate valves are installed, where the ELENA gate valve marks the handover point between the ELENA beamline and the BASE beamline. During precision measurements, the BASE experiment is completely disconnected from ELENA to reduce residual noise, and the BASE gate valve is closed. When preparing for catching, both gate valves are connected with a custom-made ceramic vacuum chamber to electrically decouple the experiment from the ground loops of the accelerator facility.

Additionally, scintillators are installed outside the superconducting magnet at the position of the Reservoir trap, the degrader, and the most downstream beam monitors. The scintillators detect pions resulting from antiproton annihilation [144, 145]. They are triggered by the antiproton ejection towards BASE and give us insight into how far the antiprotons traveled into the beamline and the trap stack, which is important for beam steering and catching of the antiprotons.

5.2.1 Electronics for catching

To catch antiprotons from ELENA, high-voltage (HV) potential barriers are needed. For us, this means connecting the HV voltage trap electrodes to appropriate power supplies. Figure 5.3 shows the change in the electronic setup within the trap stack. Compared to Figure 5.1, it also includes the electron gun (see Chapter 3.2.7), which is mounted on the outermost downstream side of the trap stack, and the repeller electrode, completing the trap stack from the upstream side. The electron gun is used to either load electrons or protons in the trap. Between the electron gun and the Reservoir trap lie the other traps (see Chapter 3.2.4), which are not drawn in this diagram.

Focusing on the Reservoir trap and the high-voltage electrodes, both HV-electrodes need to be connected to a high-voltage power supply in order to provide a trapping potential for the antiproton beam coming from ELENA. The high-voltage power supply of type CAEN NDT1470 can supply up to 8 kV but has a noise of up to 30 mVpp [146], which is comparably high to the standard trap biasing power supply UM 1-14 LN-SW, which fluctuates up to 0.5 μVpp [124] (but can only supply voltages in the range of $\pm$14 V). Therefore, a diode-bridged RC filter is installed after the CAEN output. The diode bridge blocks constant voltages, which then pass the RC filter. In case of a large and fast voltage pulse, the diode bridge opens and lets the pulse pass. Nevertheless, for the purpose of lower noise reduction, we also connect a lower noise power supply to the HV-electrodes, the Stahl electronics BSHV-400. It can supply up to 400 V and has a maximum noise level of 0.75 mVpp [147]. The switching of the two HV power supplies is fulfilled by relays, which are controlled by a DC voltage.

Additionally, the line for the HVP-electrode, upstream of the Reservoir trap, has a fast switching, low-noise HV switch (Stahl electronics HS2000) implemented. The switch facilitates the HV-pulse necessary to trap the antiprotons and switches between the catching high-voltage and ground. The switch is triggered via a delay generator, which also triggers the readout of the scintillators and beam monitors; more details can be found in Section 5.2.2. The rise time of the signal is 250 ns.

5.2.2 Beam Steering and catching

Each experiment at the AD/ELENA (see Chapter 3.1) facility can request antiprotons, with simultaneous delivery possible to four experiments. If the request is fulfilled, an antiproton bunch will be ejected from ELENA towards the experiment via a transfer line.

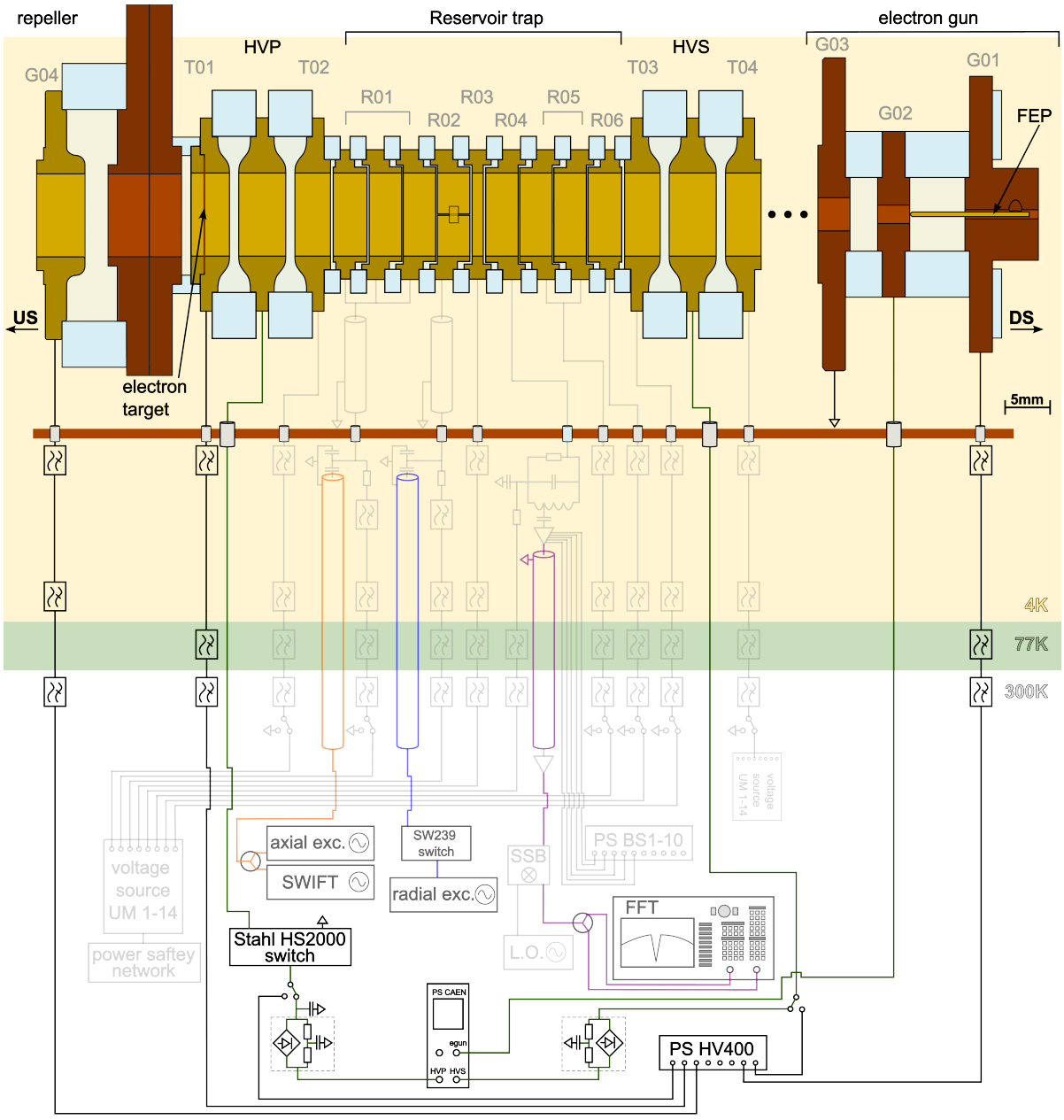

Figure 5.3: RT electronics for catching. Similar to Figure 5.1, with additional elements needed for catching. Added are the electron gun on the DS part and the repeller US. Electronics used during normal electronics are shown in light gray, whereas the additional added elements are shown in black and in green for the HV-lines. For more details see text.

Each transfer line has electrostatic steering elements with which the antiprotons can be manipulated. The steering can be modified by the user through different control knobs provided by the AD/ELENA team. The BASE experiment can adjust a horizontal and vertical angle and offset and additionally has a focus knob. The ELENA transfer line ends with a gate valve and goes over in the BASE beamline, as is shown in Figure 5.2. In the BASE beamline, four beam monitors (see Chapter 3.2.2) are used to determine the position of the beam and help understand the influence of the steering elements on the antiproton bunch. Additionally, scintillators are installed outside the BASE magnet to gain timing information on the antiprotons.

The timing information is attained by knowing the antiproton velocity and a reference time. As reference time the ELENA ejection trigger to BASE is used. This signal is fed into a Stanford Research Instrument DG645 delay generator and is distributed and appropriately delayed to trigger the beam monitors, the scintillators and HV-switch used to pulse the catching pulse applied to the HVP-electrode. As a reference, the time-of-flight of the antiprotons from ELENA ejection to the ELENA gate valve is measured by annihilating the antiprotons on the gate valve and reading out the scintillator signal, which corresponds to a time of 10.5 μs. Knowledge of the distance between the different elements in the BASE beamline (e.g. the beam monitors, degrader), the velocity of the antiprotons, and the annihilation time from the scintillators gives us insight into the annihilation point of the antiproton bunch in our experiment beamline. The antiprotons ejected from ELENA have an energy of 100 keV, corresponding to a travel time of 228 ns per meter and a bunch length of 75 ns [148]. After passing the installed degrader foil of 1760 nm thickness, the antiproton energy is reduced to 5 keV [115] corresponding to a flight time of 1022 ns per meter. Figure 5.4 shows the distance between the different elements (blue) in mm in the BASE beamline and the corresponding flight time (green) in ns for the antiprotons. The flight time is calculated assuming 100 keV antiprotons upstream and 5 keV particles downstream of the degrader. To catch the most antiprotons, we would like to catch them once the first particles fly through the Reservoir trap, get repelled by the high-voltage applied to the downstream HV-electrode (HVS), and before they leave the Reservoir trap again, the upstream HV-electrode (HVP) is biased, trapping the antiprotons. This leads to a total theoretical flight time of 578.8 ns. Knowing the response of the HV-switch (250 ns), we can set a delay time in the delay generator reflecting the flight time of the antiprotons after the ejection trigger until the particles traverse the Reservoir trap, get reflected at HVS and can be caught by biasing HVP, which is done by

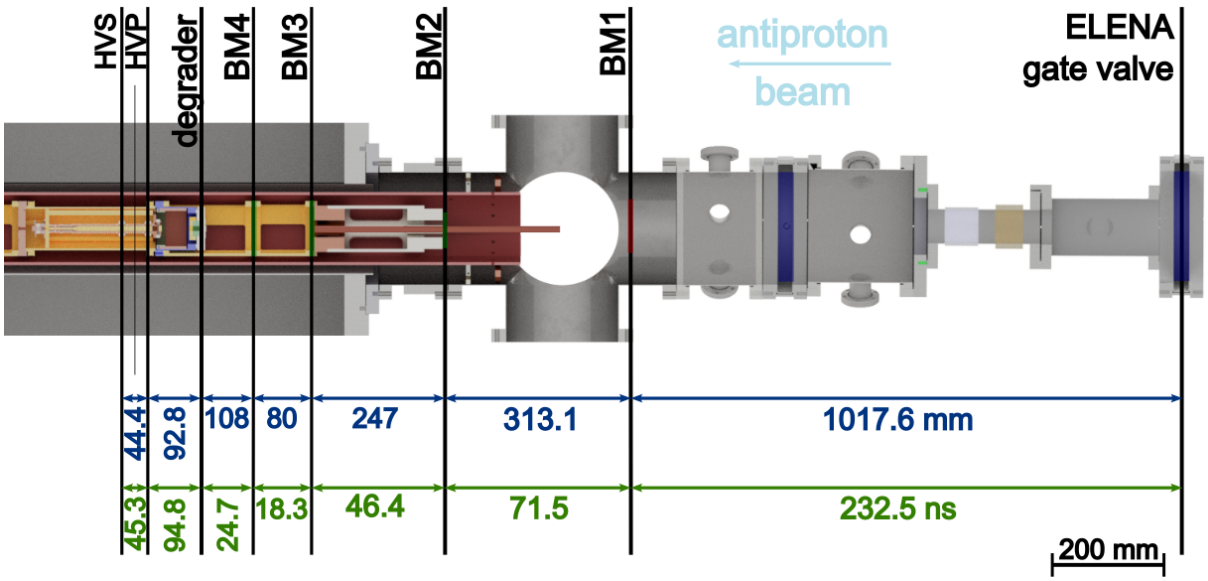

Figure 5.4: Distance (blue) of the ELENA gate valve, beam monitors, and HV-electrodes of the RT in mm and the corresponding antiproton flight time (green) in ns for a 100 keV beam upstream of the degrader and 5 keV antiprotons downstream of the degrader.

switching the HV-switch from ground to the applied HV, resulting in a set delay time of 10.83 μs after the ELENA ejection trigger.

In practice, we optimized the steering and timing parameters by maximizing the shift of the axial resonator of the Reservoir trap. As mentioned in Chapter 3.2.7, the amount of trapped electrons shifts the resonance frequency of the detector, and the electrons are being generated as a result of part of the antiproton bunch annihilating on the degrader.

The antiproton catching is summarized in Figure 5.5. First (Figure 5.5 a)), a deep axial potential (14V) is applied on the central RT electrode and electrons are being loaded in the trap, typically in the order of 6.3×10^6, as they are important to cool the caught antiprotons sympathetically [149]. The procedure follows the one described in Section 3.2.7 and both HV-electrodes are ramped to the catching potential of -1 500 V (Figure 5.5 b)). In the case of HVS it is directly applied (Figure 5.5 c)). Once the antiprotons traverse the Reservoir trap, HVP is also biased by triggering the HV-switch, switching between ground and the catching voltage (Figure 5.5 d)). Now the antiprotons are trapped and are sympathetically cooled by the already stored electrons. Once they are cold enough they are further cooled resistively through the interaction with the resonator, and the HV is switched off again. For the 2023 run the final trapping voltage applied was -1 500 V and the HV-switch was triggered with a delay time of 10,8 μs after the ELENA ejection

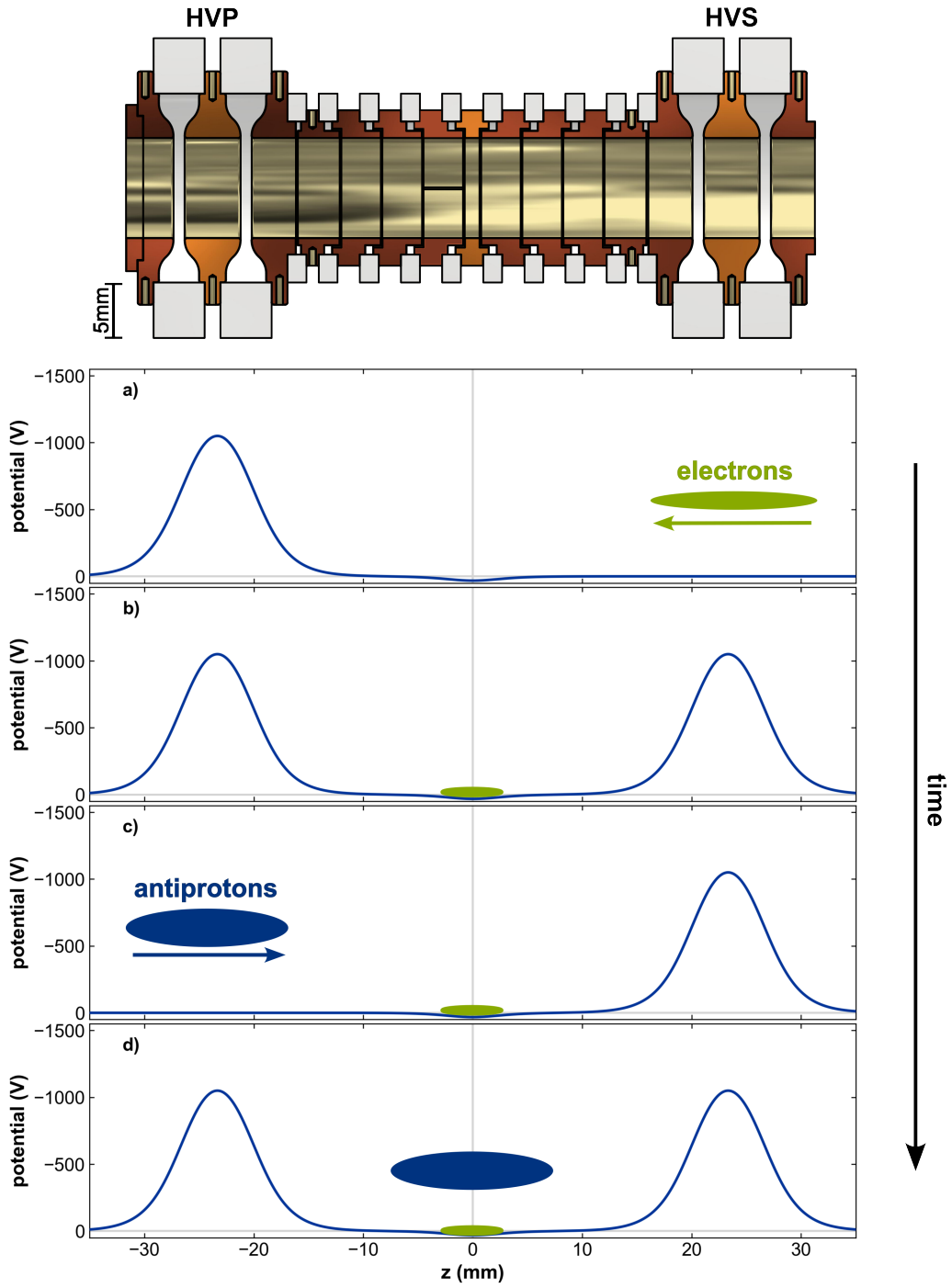

Figure 5.5: Potential of the RT and the adjacent HV-electrodes during catching. First electrons are injected a) and caught b) in the potential of the RT. Next, HVP is switched to ground to let in antiprotons (c) and HVS is creating a potential barrier for the incoming antiprotons. d) After an appropriate time, triggered by the ELENA-to-BASE ejection trigger and a delay generator, HVP is switched on and the antiprotons are caught. Afterwards, they are sympathetically cooled by the already trapped electrons. Note: the central trap potential is for visualization purposes significantly larger than actually applied, and the antiproton bunch length (75 ns) is much longer than the dimensions of the trap.

trigger.

The now trapped particles are a mixture of antiprotons, electrons, H^--ions, and other negative ions. With this, the standard particle detection method, a dip visible on the FFT of the time transient signal of the resonance circuit, is not possible (Chapter 2.2). To check if particles are trapped, a parametric resonance scan is run [150]. Here, the double axial frequency of the antiproton is irradiated, and the trap voltage is ramped in a voltage range of 6-8 V corresponding to axial frequencies of antiprotons and H^--ions correlating with the detector frequency. With the double axial drive irradiating, antiprotons will be visible as a peak on the FFT spectrum of the resonator.

5.3 Cleaning of the caught antiproton cloud

After the catching procedure to capture antiprotons from AD/ELENA, we not only trap antiprotons in our Reservoir trap, but also other contaminants like electrons, $H^-$and potentially also C^- and O^-. These trapped contaminants disturb the frequency of the antiprotons in the trap. Depending on the number and kind of other co-trapped particle, a dip is either not visible or with a lower signal-to-noise ratio (SNR) and a shifted axial frequency.

To get a clean antiproton cloud different cleaning procedures are used, which are explained in this section.

5.3.1 Electron cleaning

Electron cleaning is performed to remove co-trapped electrons, which are the main trap contaminant. For catching the antiprotons they are necessary to sympathetically cool them. However, electron contamination can also occur from time to time through beta-decay electrons. The degrader and trap stack get activated during beamtaking by the bombardment of antiprotons. We observed that the frequency with which such an event occurs is significantly higher after beam taking and decreases over time.

An efficient way to remove particles out of the trap is to apply a resonant rf-drive at one of the particles' eigenfrequencies. In our trap, electrons have an axial frequency of $\nu_{z,e} \approx 34\,\mathrm{MHz}$ at a standard ring voltage of $V_r = 7.27\,\mathrm{V}$. If an electron is on a larger magnetron orbit, its axial frequency can be an order of magnitude higher. Therefore, we do not directly excite the electrons on their axial frequency, but at a frequency of $\approx 12.5\,\mathrm{MHz}$

while lowering the axial potential. Decreasing the applied ring voltage decreases the axial frequency as well. During such a potential ramp, the electrons reach the frequency of the irradiated drive and get heated out of the trapping potential, which also holds for particles on larger magnetron radii.

In more detail, when electron cleaning in the Reservoir trap, we irradiate an axial drive at 12 MHz and -15 dBm power. Then we apply a shallower trapping potential by ramping the ring voltage down to $V_r = 0.6\,\mathrm{V}$ and up again. This value is carefully characterized by incrementally lowering the trapping potential until a small particle loss is observed. After such a potential ramp the antiprotons can accumulate magnetron energy and therefore, magnetron cooling is performed (more details in Chapter 2.2.3). This process is repeated multiple times until a clean dip is visible, e.g., at the expected axial frequency and SNR. A positive voltage can be applied to the target electrode to absorb the heated electrons, enhancing the electron removal rate.

It should be noted that the Reservoir trap has an axial resonator tuned to a higher frequency than the other traps. A standard BASE axial detector has a resonance frequency of $\approx 650\,\mathrm{kHz}$, whereas the resonance frequency of the RT detector was chosen to be $\approx 800\,\mathrm{kHz}$. The reason for this is that at a trapping voltage of $V_r = 5\,\mathrm{V}$, the axial frequency for antiprotons is around $\nu_{z,\bar{\mathrm{p}}} \approx 670\,\mathrm{kHz}$, but for electrons it is at $\nu_{z,e} = 28.7\,\mathrm{MHz}$. This is very close to the cyclotron frequency of the antiprotons $\nu_{+,\bar{\mathrm{p}}} \approx 29.5\,\mathrm{MeV}$ at a magnetic field of $B = 1.945\,\mathrm{T}$. Operating the Reservoir trap at higher axial frequencies minimizes antiproton loss, resulting from accidentally exciting the cyclotron mode of the antiprotons during electron cleaning of the reservoir.

5.3.2 SWIFT cleaning

Heavier ions can also be removed by applying a stored waveform inverse Fourier transform (SWIFT) drive [151], which, in a nutshell, is a broad-band white noise excitation signal ranging from 80 kHz to 750 kHz irradiated into the trap. Ions with a larger mass have a smaller axial frequency and therefore get excited by the drive, whereas the antiproton and H^--ions are not affected by the drive. The upper cut frequency is chosen such that H_2^+-ions still get excited. The drive is typically irradiated for 10 s with a power of -5 dBm. Subsequently, the trap is ramped to a low trapping voltage of $V \approx 0.3\,\mathrm{V}$, the excited particles leave the trap and the potential is ramped back to its original value. One voltage ramp typically takes $\approx 10\,\mathrm{s}$. When the particles are back on resonance with the

detector, magnetron cooling is performed (see Chapter 2.2.3).

5.3.3 High-voltage cleaning

Another way to clean heavier ions is to use the stability criterion in a Penning trap. As discussed in Chapter 2.1.1, a Penning trap is only stable if the relation $2\omega_z^2 < \omega_c^2$ holds. Following this, the Penning trap is not stable if

$$\frac{q}{m} < \frac{4C_2V_r}{B^2} \tag{5.1}$$

is true. Therefore, particles with a higher mass leave the trap by either decreasing the magnetic field B or by increasing the trapping voltage V_r. In our case changing the magnetic field is not an option, but applying a high-voltage is possible. As the (anti)proton has the largest $\frac{q}{m}$-ratio, heavier elements except H^--ions will leave the trap.

To utilize the so-called HV-cleaning, we first transport the (anti)protons to the downstream HV-electrode HVS, which is in this case biased by the HV-power supply CAEN NDT1470. Then the potential is slowly increased to $\approx 2\,\mathrm{kV}$, the particles are kept there for $\approx 60\,\mathrm{s}$ and afterward, the voltage is decreased again to a regular trapping voltage. Subsequently, the particles are transported back to the center of the Reservoir trap.

This cleaning method was not applied during the 2023-2025 antiproton run but was heavily used during proton operation when preparing a fresh proton reservoir.

5.3.4 H^--cleaning

With the above-described cleaning methods electrons and negative ions can be removed, mostly by applying an appropriate rf-drive. For H^--ions a direct excitation of the axial frequency is not desirable, because the axial frequency difference between H^--ions and antiprotons scales with a factor of $\sqrt{m_{\overline{\mathrm{p}}}/m_{\mathrm{H}^-}}$, resulting in a shift of only $\approx 440\,\mathrm{Hz}$.

Therefore, H^--ions are heated out of the trap via a sweep excitation of the cyclotron mode. For the cyclotron mode, the H^--ion's frequency is $\approx 32\,\mathrm{kHz}$ lower than the one of the antiproton, giving enough distance in frequency space to excite the H^--ions but not the antiprotons.

To excite the H^--ions, a drive is swept in a frequency span of 6 kHz around the calculated H^--frequency for 60 s at a power of -20 dBm. Subsequently, the trap potential is lowered to $V_r = 0.37\,\mathrm{V}$ and the excited H^--ions can escape. Then, the potential is raised again to

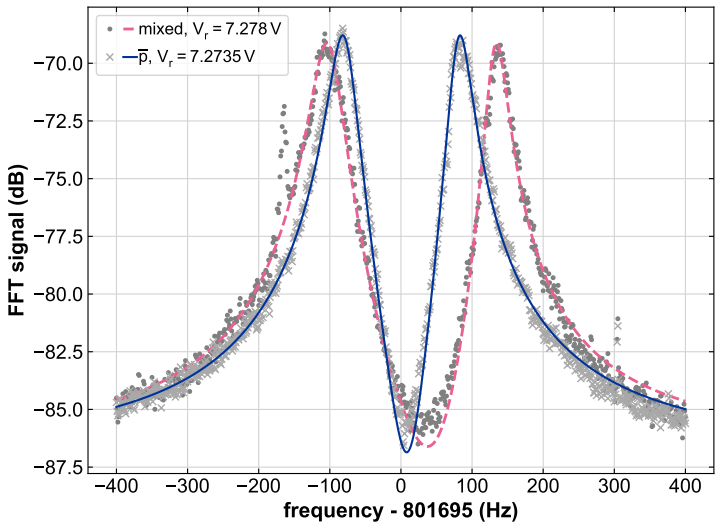

Figure 5.6: Mixed dip (H^--ions & antiprotons) in pink and dip after H^--cleaning with only antiprotons in blue.

its initial value, and the remaining particles are magnetron cooled (see Chapter 2.2.3).

This procedure is repeated multiple times until all H^--ions are removed, visible by the fact that only particles at the antiproton axial frequency are detected. Moreover, after successfully catching antiprotons for the first time, the trap is emptied again and the Reservoir trap is characterized with protons. Here, especially the cyclotron frequency is measured and the strength of the heating drive is characterized in a way, that all protons are 100% removed from the trap. These parameters are then used to remove H^--ions out of the trap after another successful antiproton catching attempt.

Figure 5.6 shows the FFT spectrum of a mixed dip (H^--ions and antiprotons) in pink and the cleaned antiproton dip in blue. We expect that the frequency of the mixed dip corresponds to the average frequency of antiprotons and H^--ions, meaning we would expect the axial frequency of the mixed cloud -220 Hz below the one of the pure antiproton cloud. However, these dip spectra were taken at different ring voltages V_r, as indicated on the plot. A difference of $\Delta V_r = +1\,\text{mV}$ results in an axial frequency shift of $+55\,\text{Hz}$. Here, we have a $\Delta V_r = +4.5\,\text{mV}$, therefore the mixed dip is $+250\,\text{Hz}$ higher than the pure antiproton one. Both shifts in total result in a frequency difference of $\Delta\nu_z = +30\,\text{Hz}$ of the mixed dip compared to the pure antiproton dip. The fitted axial frequencies of both clouds are $\nu_{z,\overline{\text{p}}} = 801702\,\text{Hz}$ and $\nu_{z,\text{mixed}} = 801732\,\text{Hz}$ and reflect this frequency shift of 30 Hz. Therefore, we conclude on having a pure antiproton cloud stored in the Reservoir

trap. Highlighting the pureness of the antiproton cloud, we also have never observed the extraction of any H^--ions into the Precision trap.

5.4 Extraction of single antiprotons

To perform measurements in the precision traps, it is important to extract the stored particles from the Reservoir trap. For this purpose, we can separate a fraction of particles in the Reservoir trap and extract them to the precision measurement traps.

For this reason, the so-called 'potential tweezers scheme' was invented [118] and further developed over the years. The goal of this scheme is to extract a single antiproton from the reservoir. Figure 5.7 illustrates the steps as applied in the current antiproton run. First, the voltage is symmetrically increased to form a deep trapping potential ($V_r = 12.5\,\mathrm{V}$). Then, a slightly larger voltage is applied to the upstream correction electrode. This shifts the center of mass of the particles slightly upstream, we call this applied voltage the 'separation voltage' because it defines the fraction of separated particles (a). In the next step, the ring electrode is ramped to $V_r = -13.5\,\mathrm{V}$, essentially splitting the potential well into two (b). Afterward, the downstream fraction of the particles is transported using adiabatic ramps to the outermost RT electrode (c). In the last step, the downstream HV-electrode HVS is ramped to form a trapping potential, and the outermost RT electrode is set to zero again, such that the separated particles are solely trapped by HVS (d). From here onward the extracted particles get controlled by the control system of the precision measurement traps and the number of extracted particles can be determined in the Precision trap.

Figure 5.8 shows the result of separation studies performed at the beginning of November 2023. Here, the separation voltage was changed to see its effect on the fraction of particles extracted from the reservoir. The blue dots depict the number of particles in the Reservoir trap after an extraction. Considering the Boltzmann-distributed particles due to the interaction with the detection system, the fraction of extracted particles can be described as [118]

$$N_{\mathrm{exc}} = C \cdot \int_{z_0}^{\infty} |z| \exp(-\frac{2\pi^2 m(\nu_z z)^2}{k_{\mathrm{B}} T_z}) dz. \tag{5.2}$$

It demonstrates that we can reproducibly separate different fractions of particles out of the reservoir. Only two measurements (blue diamonds) were taken of the particle count

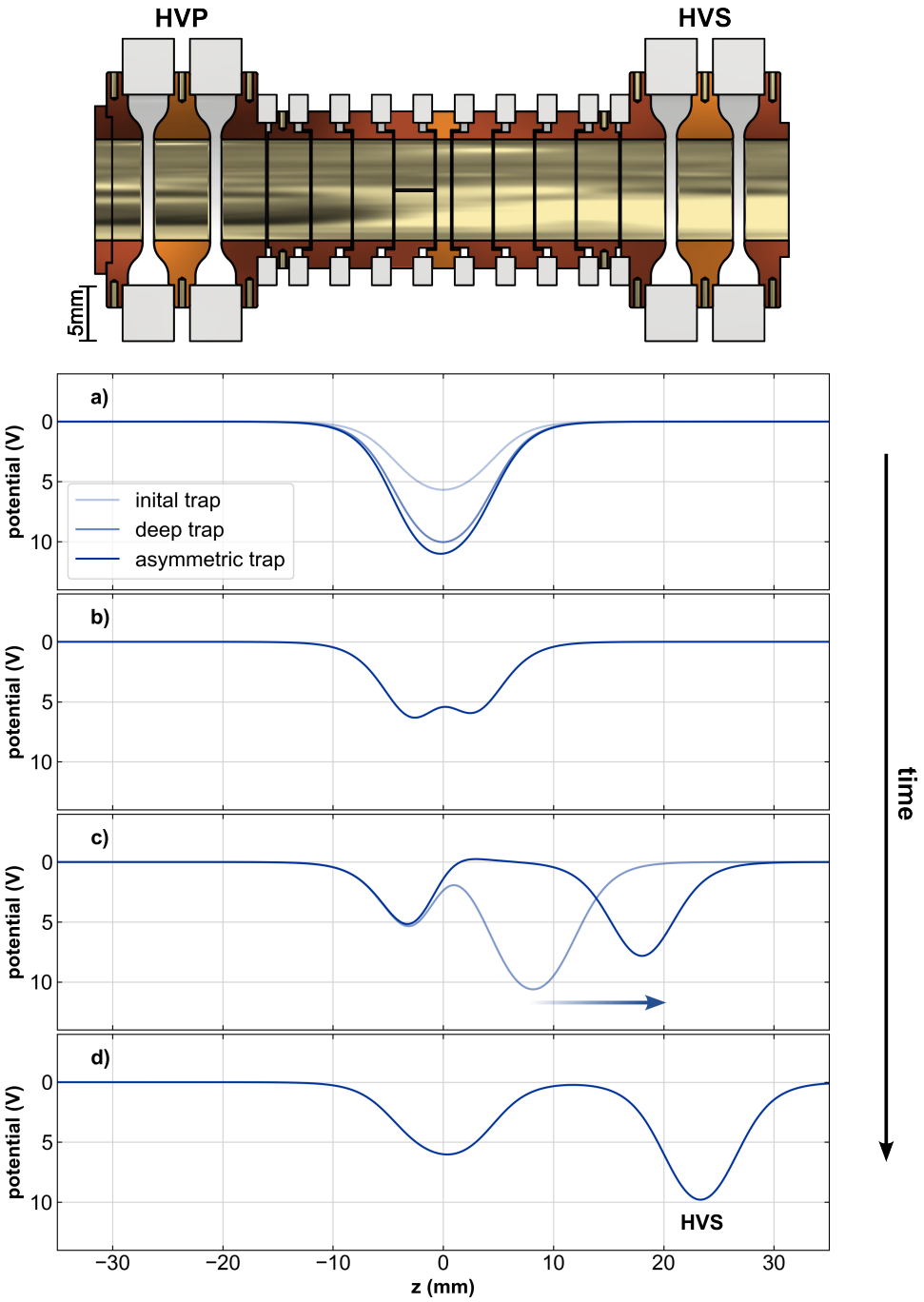

Figure 5.7: Voltages applied during separation and merging. a) The trap potential is lowered to 12.5 V, forming a deep potential trap. In the last step, the potential is slightly asymmetric by applying a larger absolute voltage on the upstream correction electrode. b) A large positive voltage is applied to the central electrode, splitting the reservoir in two. c) The particles in the left (downstream) potential well are transported closer to the Precision trap via adiabatic ramps. d) In the last step the separated particles are transported to HVS, the handover-point to the precision measurement traps and their control system.

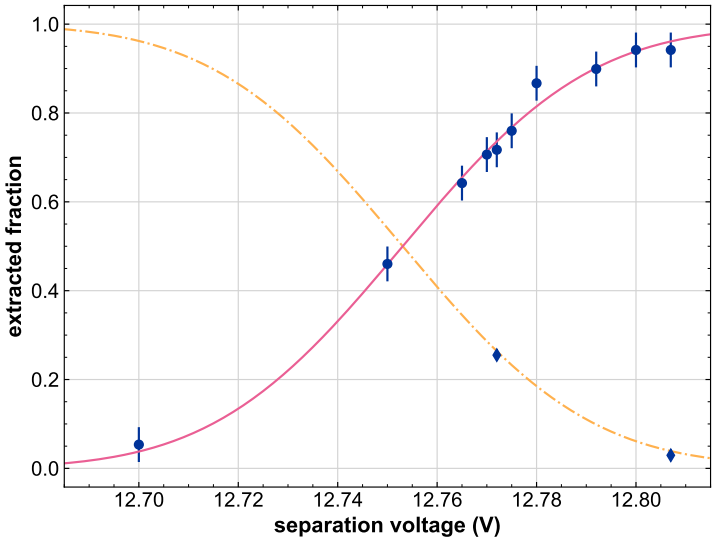

Figure 5.8: The extracted fraction of particles after separation in the Reservoir trap is dependent on the separation voltage (blue circles, pink line). The predicted particle number in the precision trap is projected and visible as the yellow dashed-dotted line. Twice the dip width was also measured in the Precision trap after the separation procedure, resulting in the two diamond data points, which fit well to the predicted fraction of extracted particles.

in the PT after the extraction, but they agree well with the predicted fraction. With this, and the knowledge of earlier performed separation studies [118], we can say that lossless separation and extraction can be performed. This information is especially important for transportable trap systems like BASE-STEP [61], which rely on reliable extraction to high-precision Penning trap experiments.

5.5 Maintenance of the reservoir

The content of the Reservoir trap is very important for the operation of a precision measurement. Therefore, we regularly maintain our antiprotons stored in the Reservoir trap. When unsupervised, the antiprotons interact with each other and accumulate magnetron energy, which could potentially result in particle loss. Moreover, electrons emitted by beta-decay of activated trap material can contaminate the antiproton cloud.

To counteract this, we repeatedly uphold the reservoir. This means we electron clean and magnetron cool the particles in the Reservoir trap. This is done after every cryoliquid filling cycle of the experiment, which happens every 2-3 days.

In detail, we first magnetron cool the particles by irradiating the upper magnetron

sideband ($\nu_z + \nu_-$) at a drive strength of -20 dBm until a prominent double dip is visible, indicating the particles are magnetron cold, before we start the electron cleaning procedure. As outlined in Section 5.3.1, we first ramp the trap down to 0.6 V without irradiating the electron cleaning drive. This is done to check the behavior of the antiprotons after having undergone the voltage ramp. In case heating occurs, due to noise on the system, we would not continue with electron cleaning. It should be noted here that a bit of heating is normal, meaning that the particles accumulate axial energy (SNR reduced by 1-2 dB) and magnetron energy. After another round of magnetron cooling, the electron cleaning procedure as described above is executed. After a final round of magnetron cooling, the maintenance activity is concluded.

At this point, it should be noted that the particle interaction and cooling times depend strongly on the particle number [152]. For a large particle cloud of hundreds of particles it is necessary to irradiate the magnetron drive for ≈ 10 min, with an additional waiting time ≈ 10 min after the drive is switched off to let the axial motion thermalize as well. During the application of the drive, the axial potential is ramped by ± 30 mV in steps of 1 mV in order to cool magnetron hot particles in a broader frequency range. A waiting time of ≈ 1 min after ramping the voltage to a shallow potential and back is also advised in order to let the particles thermalize with the resonator. For small particle clouds with ≈ 15 particles, the timescales are much shorter. A magnetron cold particle cloud is prepared by irradiating the drive for ≈ 1 min, and waiting afterward is not necessary.

The effect of the reservoir maintenance is visualized in Figure 5.9 a). The axial frequency, signal-to-noise ratio (SNR), and dip width are shown over 5 days during which no particle extraction occurred. After performing the maintenance on the reservoir (green line), the particles accumulate magnetron energy over time, resulting in an increase in axial frequency. Therefore, the measured dip SNR decreases as the particles move over the resonator and the scatter in the axial frequency increases. This also leads to an increase in the width of the dip. Two points are highlighted as magenta and orange diamonds. Figure 5.9 b) shows the FFT spectra of these two points. The magenta dashed line represents a dip shortly after the maintenance action, and the orange line one just before, visualizing the difference in axial frequency, SNR, and dip width.

Thus, this effect could influence the determined number of particles stored in the trap. For the later presented determination of the antiproton lifetime (Chapter 6), only data in a 12 hour window after maintaining the reservoir is considered, here marked in yellow.

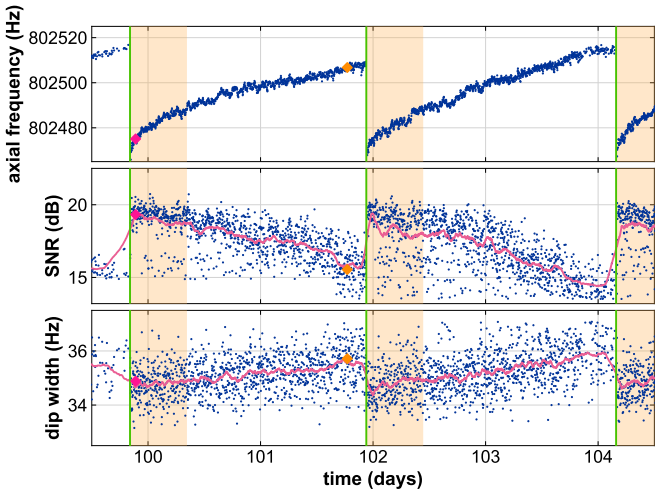

(a) Time evolution for axial frequency, SNR and dip width

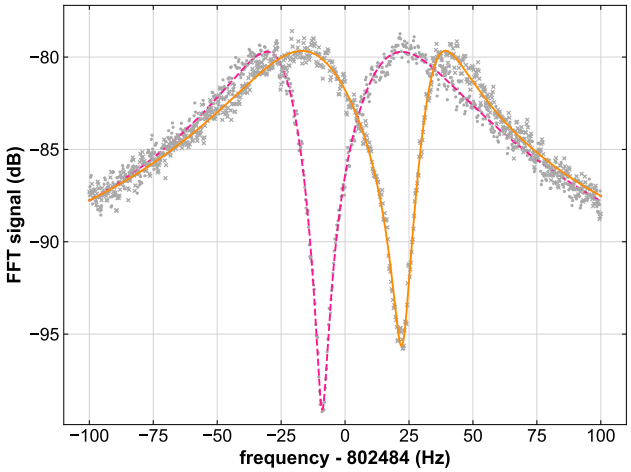

(b) FFT spectra of dips directly after and before maintenance

Figure 5.9: (a) The dip frequency, signal-to-noise ratio (SNR), and dip width over 5 days during which no particle extraction occurred are depicted in blue, with a moving average plotted in pink to guide the eye. After performing the maintenance on the reservoir (green), the particles accumulate magnetron energy over time resulting in an increase in axial frequency (upper). Therefore, the measured dip SNR is decreasing (middle), as the particles are moving over the resonator and the scatter in the axial frequency is increasing. This also leads to an increase in the width of the dip (lower plot). Thus this effect can influence the extracted amount of particles stored in the trap. For the later presented determination of the antiprotons lifetime only data in a 12 hour window after maintaining the reservoir is considered, here marked in yellow. (b) shows the FFT spectra for the magenta and orange diamonds in (a). Here, the difference in lineshape directly after maintenance (magenta dashed) and just before the maintenance action (orange) is visualized.

Chapter 6

Improved direct limits on the antiproton lifetime

6.1 Motivation

The CPT theorem [28] states that the properties of matter and antimatter should strictly have the same absolute values. These properties include the charge-to-mass ratio, the magnetic moment, and the lifetime. When looking more specifically at the properties of the proton and antiproton, there is a striking difference of multiple orders of magnitude in the known lower limits on their respective lifetimes.

Recent results from the SNO+ collaboration constrain the proton lifetime to $\tau_{\mathrm{p}} > 3.6 \times 10^{29}\,\mathrm{a}$ [153]. Here, the decay of $^{16}\mathrm{O} \rightarrow {}^{15}\mathrm{N}^{*}$ is monitored by searching for the emission of characteristic gamma radiation during the de-excitation of $^{15}\mathrm{N}^{*}$. This result is independent of any models and branching ratios and also includes invisible decays, where the final states are not detectable. For specific decay channels, the proton lifetime is even constrained to $\tau_{\mathrm{p}}(\mathrm{p} \rightarrow e^{+}\pi^{0}) > 1.6 \times 10^{34}$ years [154].

For the antiproton, on the other hand, the experimentally determined lifetime constraints are significantly smaller. The antiproton lifetime was, for example, estimated to $\tau_{\overline{\mathrm{p}}} > 0.8 \times 10^{6}$ years by looking at the incident antiproton flux in cosmic rays on earth [155]. This result strongly depends on the models used to describe the production and propagation of antiprotons and their interactions in earth's heliosphere. First direct measurements of the antiproton lifetime have been conducted by the APEX collaboration at Fermilab's Antiproton Accumulator [156, 157]. Searching for leptonic decay products originating from the circulating antiprotons in the storage ring sets constrains on 13 decay channels ranging from $\tau_{\overline{\mathrm{p}}}(\overline{\mathrm{p}} \rightarrow e^{-}\omega) > 2 \times 10^{2}$ years to $\tau_{\overline{\mathrm{p}}}(\overline{\mathrm{p}} \rightarrow e^{-}\gamma) > 7 \times 10^{5}$ years.

However, some antiproton decay channels preferred by Grand Unification Theories, like $\overline{\mathrm{p}} \rightarrow \nu_{e,\mu} K^-$ [158], are not covered by the lifetime constraints.

In the BASE Reservoir trap, continuous monitoring of the stored antiprotons allows for inferring direct constraints on the antiproton lifetime that do not depend on specific decay channels or theoretical models and are also sensitive to invisible decays in the aforementioned sense.

6.2 Measurement concept

From our antiprotons stored in the Reservoir trap, we can derive a direct lower limit of the antiproton lifetime. This requires the knowledge of the number of stored particles, which we can extract from the interaction of particles with the resonant detection system. As discussed in Chapter 2.2, a single particle in thermal equilibrium with an LC resonant circuit tuned to its resonance frequency is visible as a dip on the noise spectrum of the resonator. Figure 6.1 shows the dip spectrum of stored antiprotons in the Reservoir trap. The width of this dip $\delta\nu_\mathrm{z}$ for a single particle is given by [68]

$$\delta\nu_\mathrm{z} = \frac{1}{2\pi}\frac{R_p}{m}\frac{q^2}{D_\mathrm{eff}^2}, \tag{6.1}$$

where $R_p = \omega_\mathrm{res} Q L$ is the effective parallel resistance of the resonator, and D_eff the effective electrode distance, which is a geometrical measure describing the coupling strength of a particle to the electrode on which the detector picks up the particle signal [79]. For multiple particles, the dip width scales with the number of particles, as analysed and described in [68]. For large particle clouds $\delta\nu_\mathrm{z} \propto \sqrt{N}$, whereas for smaller particle numbers the dip width scales linearly with the single particle dip with:

$$\delta\nu_\mathrm{z}(N) = N \times \delta\nu_{z,\mathrm{single}} = \frac{N}{2\pi}\frac{R_p}{m}\frac{q^2}{D^2}. \tag{6.2}$$

The content of the Reservoir trap is continuously monitored by recording the time transient of the signal and taking its fast Fourier transform (FFT). With a least-squares fit of the well-known line shape to the FFT spectrum, we determine the dip width $\delta\nu_\mathrm{z}$, as well as the dip frequency, the resonator frequency and width, and the dip signal-to-noise ratio (SNR) of the antiproton cloud. The behaviour for large particle clouds is already accounted for in the fitting routine, enabling the use of the linear scaling as in Equa-

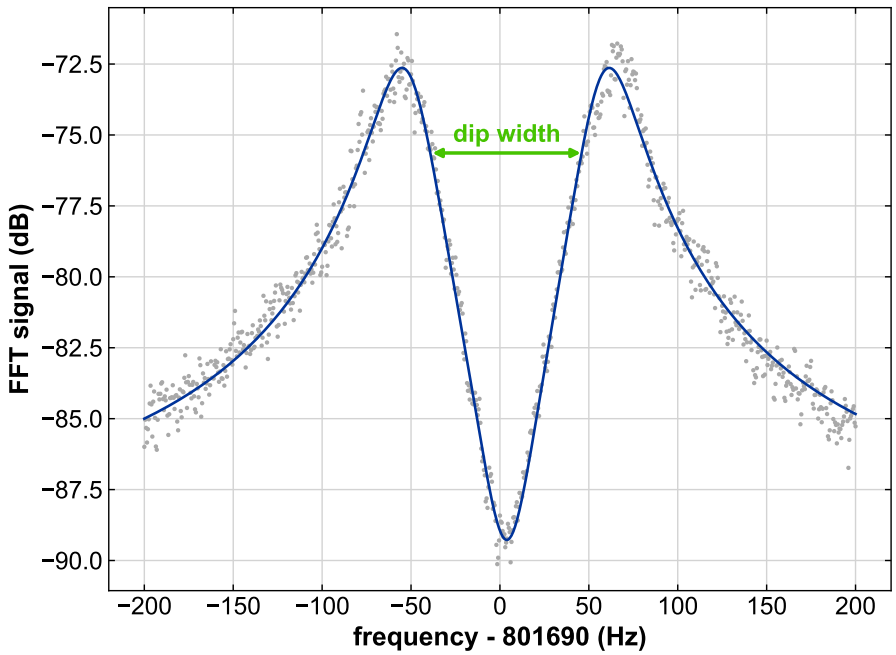

Figure 6.1: FFT spectrum of the antiprotons in the reservoir trap. The dip width is the 3 dB width of the dip, shown in green. This spectrum was recorded on 2023-11-04 and shows the dip of a full reservoir with 99 trapped antiprotons.

tion (6.2) to estimate the amount of trapped particles.

To obtain a lower limit on the lifetime, we first integrate the particle number over time, which yields an equivalent single particle observation time

$$T_{\mathrm{obs}} = \int N(t)dt. \tag{6.3}$$

Having recorded multiple such data sets over the years, we can combine them and get a total observation time of $T_{\mathrm{obs,total}} = \sum T_{\mathrm{obs,i}}$. A possible antiproton decay can be described by Poisson statistics. The probability of observing n decays during the time T_{obs} is given by

$$p(n;\lambda) = \frac{\lambda^n \exp(-\lambda)}{n!}, \tag{6.4}$$

where $\lambda = T_{\mathrm{obs}}/\tau_{\overline{\mathrm{p}}}$. In case no particle decay is observed, the probability is described by the decay law

$$p(0;\lambda) = \exp(-\lambda) = \exp(-T_{\mathrm{obs}}/\tau_{\overline{\mathrm{p}}}). \tag{6.5}$$

We can constrain the antiproton lifetime for a desired confidence level (CL) with:

$$\mathrm{CL} = 1 - \exp\left(\frac{T_{\mathrm{obs}}}{\tau_{\overline{\mathrm{p}}}}\right) \tag{6.6}$$

$$\tau_{\overline{\mathrm{p}},\mathrm{lower}} = -\frac{T_{\mathrm{obs}}}{\ln\left(1-\mathrm{CL}\right)}. \tag{6.7}$$

The following sections discuss the determination of an improved value for the direct lower limit on the antiproton lifetime, using data from three different measurement campaigns at BASE.

6.3 Antiproton lifetime limits measured in 2017 - 2019

During the last BASE charge-to-mass ratio measurement [55], running from 2017 to 2019, the Reservoir trap was loaded with bunches of antiprotons and H^--ions before the precision measurements could start over the YETS. This section presents two datasets of recorded reservoir data accumulated over the 2017/2018 and 2018/2019 runs. It should be noted that in both cases, a mixed cloud of both antiprotons and negatively charged hydrogen ions (also hydride (H^-)) was stored, as required for the charge-to-mass ratio comparisons [142]. The following discussion includes both species, and is subsequently corrected for the H^--ion content in Section 6.3.3. The particles were continuously monitored by recording a fast Fourier transform (FFT) of the time transient signal of the stored particles interacting with the superconducting LC-circuit; an exemplary spectrum recorded in 2023 can be seen in Figure 6.1.

From the well-known line shape [68], we can extract via a least-squares fit the axial frequency ν_{z} of the particles in the reservoir, as well as their dip width $\delta\nu_{\mathrm{z}}$, and the resonator frequency ν_{res} and its width $\delta\nu_{\mathrm{res}}$. From Equation (6.2) we see that the particles' dip width depends on the the number of stored particles, but also on the resonator's parallel resistance $R_p = 2\pi\nu_{\mathrm{res}}QL$ and the effective electrode distance $D_{\mathrm{eff}} = 10.3\,\mathrm{mm}$, which is calculated by potential theory and is robust within the machining precision of the trap electrodes.

During the charge-to-mass ratio run, the RT's axial detector was operated at $\nu_{\mathrm{res}} \approx 793\,\mathrm{kHz}$ and had an inductance $L = 1.675(25)\,\mathrm{mH}$, characterized in a separate measure-

ment. The quality factor Q is influenced by parasitic losses, such as those arising from a long resonator line, which is shielded as effectively as possible, and by variations in capacitive coupling that change with each assembly after a warm-up, leading to changes in Q with each run. For the 2017/2018 run $Q \approx 22\,200$, resulting in an $R_p = 185(3)\,\mathrm{M\Omega}$ and a single particle dip width of $\nu_{z,\mathrm{single}} = 4.50(7)\,\mathrm{Hz}$. For the 2018/2019 run the quality factor was higher $Q \approx 28\,400$ leading to $R_p = 237(4)\,\mathrm{M\Omega}$, which yields a single particle dip width of $\nu_{z,\mathrm{single}} = 5.75(9)\,\mathrm{Hz}$. The uncertainty in the single particle dip width is rooted in the uncertainty of the inductance L. Antiproton lifetime limits of these two datasets have already been discussed in the PhD thesis of Matthias Borchert [93].

6.3.1 2017/2018 data

During the 2017/2018 run 241 020 spectra were recorded over 189.5 days. Figure 6.2 a) shows the particle number history, extracted from these spectra, starting from the catching of the antiprotons and H^--ions. The particle number is calculated by applying Equation (6.2) and using the resonator's frequency ν_{res} and width $\delta\nu_{\mathrm{res}}$, and the dip width $\delta\nu_{\mathrm{z}}$, taken from the least-squares fit to the spectrum. The gray points display all data points except noise-related outliers. The scatter in the particle number is caused by fit-noise, and the drifts are due to electron contamination, which are caused by beta-decays in the activated degrader. This can be seen, for example, in a very strong downwards drift in particle number after around 65 days. Electron contamination is visible as a decrease in axial frequency and SNR of the particle's dip and is accounted for in the evaluation.

As explained in Section 5.5, magnetron cooling and electron cleaning are performed regularly. To ensure accuracy and adopt a conservative approach, only the first twelve hours of data following reservoir maintenance (see Chapter 5.5) were included in the evaluation, which are the data points depicted in blue. A moving average over the blue points is shown in pink to guide the eye.

In the beginning, 69 particles are stored in the Reservoir trap. All following drops were caused by an operator interacting with the trap, e.g., to extract (see Chapter 5.4) a particle to the precision measurement traps. The first month of the dataset corresponds to the commissioning phase of the experiment, during which new routines – including rf-drive calibration and transport procedure – were established, consequently causing higher particle losses. The larger downward step in particle numbers around day 65 of trapping is due to an unscheduled power cut, where the particle in the Precision trap was lost.

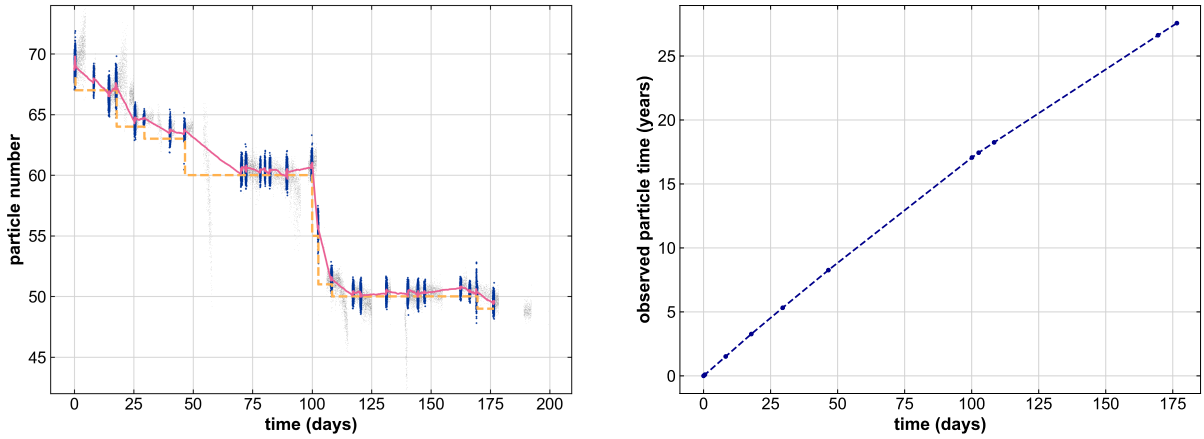

(a) Particle number over time (2017/2018)

(b) Observed particle years (2017/2018)

Figure 6.2: Results from the 2017/2018 run. a) shows the number of particles over time. The points in gray represent data noise filtering; for better visibility, only every 10th point is plotted. The blue points depict all data points used for the evaluation, which are always the first 12 hours after the strap maintenance. Also, electron-contaminated data was excluded. More details can be found in the text. To guide the eye, a moving mean of the blue points is plotted in pink. The dashed yellow line shows the particle number estimate used to compute the equivalent single particle observation time, plotted in b).

During the following extraction attempt, three particles were extracted, reducing the particle number in the reservoir to 60, from which two were evaporated in the Precision trap. After about 100 days, the first precision measurement cycle was completed, and an extensive electron cleaning was required in the Reservoir trap, resulting in the loss of 9 particles. During the cleaning procedure, the noise of the strong rf-drives overlapped with the frequency window of the trapped particles, leading to their evaporation. Afterwards, a systematic and precision measurement campaign started again in which only two particles were lost. Figure 6.2 b) shows the cumulated single particle observation time for the 2017/2018 run. As we are constraining a lower limit on the antiproton lifetime, the conservative approach was chosen to use the mean value of the particle number minus one standard deviation and round this number to an integer value for the stored number of particles in a given time interval. These values are plotted as the yellow dashed line in Figure 6.2 a). The integrated equivalent single particle observation time over the storage time of the mixed reservoir is shown in Figure 6.2 b) and accumulates to $T_{\mathrm{obs},2017} = 27.56$ years. Section 6.3.3 discusses the contribution of the antiproton content in the mixed reservoir.

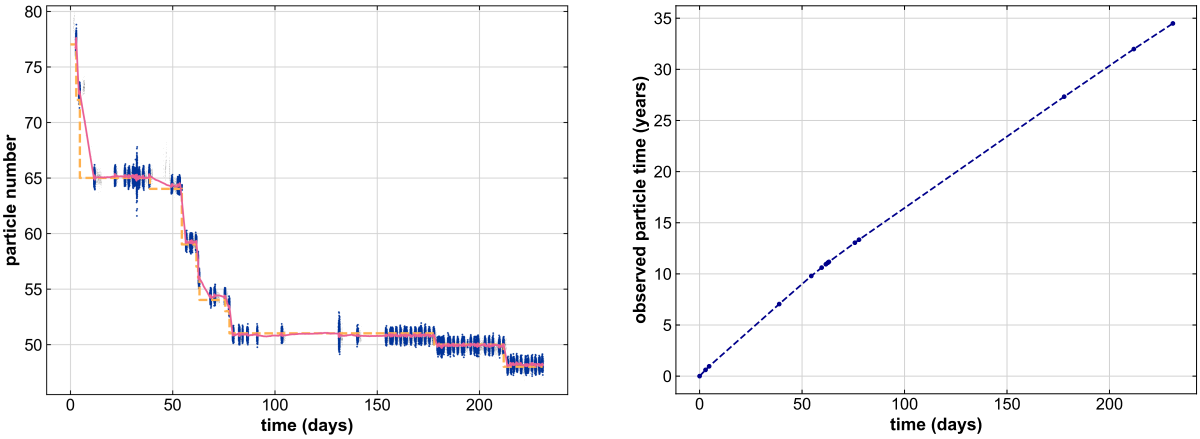

(a) Particle number over time (2018/2019)

(b) Observed particle years (2018/2019)

Figure 6.3: Results from the 2018/2019 run. a) shows the number of particles over time. The points in gray represent data noise filtering; for better visibility, only every 10th point is plotted. The blue points depict all data points used for the evaluation, which are always the first 12 hours after the strap maintenance. Also, electron-contaminated data was excluded. More details can be found in the text. To guide the eye, a moving mean of the blue points is plotted in pink. The dashed yellow line shows the particle number estimate used to compute the equivalent single particle observation time, plotted in b).

6.3.2 2018/2019 data

In the 2018/2019 run, we have stored antiprotons for 231 days during which 157 246 spectra of the reservoir were recorded. From these recorded spectra, we extract the stored particle number using Equation (6.2), as described above. Figure 6.3 a) shows the number of particles stored in the Reservoir trap over time. The gray points depict all data after outlier removal. For better visibility, only every 10th point was plotted. Compared to the 2017/2018 dataset, the one from 2018/2019 is more stable and robust. This is most likely due to the fact that the degrader was exchanged and only a few antiproton catching attempts were performed, contrary to the previous run. This results in less activation of the degrader and trap electrodes and therefore in fewer beta-decay electrons and a more stable antiproton reservoir. As in the previous evaluation, data from an electron-contaminated reservoir was excluded from the final result. Electrons were removed from the trap on a regular basis (see Chapter 5.5). Only data points in a 12-hour window after the maintenance operation are accepted for the final evaluation, shown by the blue points, in order to counteract for possible drifts on the dip. A moving average of these data points is plotted in pink.

In the first few days after catching the antiprotons, the loss rate in the reservoir is high due to the commissioning of the whole experiment and intentional particle loss to reduce the cooling time after reservoir maintenance and particle extraction [152] (Chapter 5.5). After 10 days, the precision measurement starts, and the particle number is stable for over a month. A striking feature in Figure 6.3 a) is the three large losses between 50 and 80 days. Here, the higher loss rate is due to problems merging the extracted particles back to the reservoir, as the number of lost particles correlates with the amount of extraction attempts [93]. Afterwards, the reservoir is very stable; only three particles were consumed in over 5 months. All losses in the Reservoir trap are due to an operator interacting with the trapped particles, for example, when extracting a particle into the Precision trap. For instance, it was necessary to extract a new particle into the Precision trap around day 63, when the particle in the Precision trap was lost, because the ground of the BASE experiment was disconnected from the one in the AMF during (see Chapter 5.5) maintenance work in CERN's long shutdown two (LS2). This caused the precision voltage supplies to float and resulted in a particle loss. Excluding particle losses not caused by environmental factors, we compute the equivalent single-particle observation time as outlined in Section 6.2. To estimate a lower bound on the particle number, we subtract one standard deviation from the mean particle count during a stable period and round the result to the nearest integer. This estimate is shown as the yellow dashed line in Figure 6.3 a). Summing the resulting observation periods yields a total equivalent single-particle observation time of $T_{\mathrm{obs,2019}} = 34.48$ years.

6.3.3 Antiproton content of the reservoir

During the time of the charge-to-mass ratio campaign in 2017 - 2019, a mixed reservoir of both antiprotons and negatively charged hydrogen ions (H^-) was stored in the Reservoir trap, making it necessary to determine the amount of trapped antiprotons to establish a lower limit on the antiproton lifetime. Usually, one would measure the amount of antiprotons by removing the H^--ions as described in Chapter 5.3.4. Unfortunately, both experimental campaigns ended unexpectedly due to quenching of the experiment. Therefore the amount of antiprotons can be estimated using data from extraction attempts (see Chapter 5.4). After each extraction, the content of the extracted particle cloud is analyzed in the Precision trap. Here, the axial frequencies of the antiproton and H^--ion differ by about 350 Hz due to their different mass, allowing us to distinguish between them

Run	Run-Time	Consumed particles	Observed particle years mixed reservoir	Observed particle years $\overline{\mathrm{p}}$	Observed particle years $\overline{\mathrm{p}}$ (lower limit)
2017/2018	189.5 days	20	27.56 a	14.37 a	11.58 a
2018/2019	231 days	29	34.48 a	8.50 a	4.92 a

Table 6.1: Summary of reservoir content of the charge-to-mass ratio campaign 2017 - 2019.

(see also Chapter 5.3.4).

Using the knowledge of the extracted particle type sequence and the number of particles $N_{0,k}$ before an extraction attempt, the initial antiproton particle number can be calculated by maximizing the probability P_S of extracting a sequence of antiprotons and H^--ions [93]:

$$P_S(N_{\overline{\mathrm{p}}}) = \prod_{k,1}^{N} P_k(N_{0,k},\, N_{\overline{\mathrm{p}},k}), \tag{6.8}$$

where the estimator $N_{\overline{\mathrm{p}},k}$ is the number of antiprotons in the reservoir. This gives for the 2017/2018 dataset an initial antiproton number of $N_{\overline{\mathrm{p}},2017} = 36(7)$ and for the 2018/2019 run $N_{\overline{\mathrm{p}},2019} = 19(8)$. With these numbers, we can give a value and lower limit on the equivalent observed single particle time for antiprotons, which can be found in Table 6.1.

6.4 Antiproton lifetime limit measured in 2023 - 2025

During CERN's Long Shutdown 2 (LS2) (2019-2021), the BASE experiment was re-built for measuring g-factors and catching antiprotons from the new ELENA storage ring, which provides antiprotons with less energy than the AD did before. This includes a completely new trap system, corresponding electronics, and a novel degrader system [115] (see Chapter 3). With this new system, we caught antiprotons for the first time on October 27, 2023. More details on the catching of antiprotons can be found in Chapter 5.2 and in the thesis of Bela Arndt [159]. Following the capture of antiprotons, contaminants such as H^--ions and electrons were carefully removed, as described in Chapter 5.3.4.

As explained in Section 6.2, we want to extract the number of stored antiprotons to determine a direct limit on the antiproton lifetime. This can be done using the width of the antiprotons' dip on the resonator's spectrum (see Figure 6.1). For this, we recorded in total 360 456 spectra accumulated over 566 days, the longest time antiprotons have ever been trapped continuously. We extract the dip width $\delta\nu_z$ from this spectra by employing

a least-square fit, which also gives us values for the dip center frequency ν_z as well as the resonator center frequency ν_{res} and the resonator width $\delta\nu_{res}$. During this run, noise disturbances on the RT detection system required an adjustment of the amplifier's working point, which in turn led to a shift in the resonator's center frequency ν_{res} and Q-value due to feedback effects (Chapter 2.2.2). The Q-value is about $Q \approx 10\,600$ and a careful determination of the resonator's inductance is discussed in Section 6.4.1.

Figure 6.4 shows the recorded dip width over time during the commissioning phase of the trap system for the 2024 g-factor run. During the first weeks after capturing, the whole experiment had to be commissioned, which caused particle losses. Further, reducing the number of antiprotons is also practical for efficient experiment operation, as the cooling time increases with increasing particle number [152], as described in Chapter 5.5.

Each such change in particle number can be attributed to an operator working on the trap. The most striking events are labeled in Figure 6.4. As a first step of commissioning the experiment after antiproton catching, the separation routine has to be characterized in order to extract single particles from the Reservoir trap. The first separation attempt was not successful, and a fraction of the antiprotons was lost (①) in Figure 6.4). We continued with the characterization of the separation, and on that occasion, a larger fraction of antiprotons were transported to the Precision trap and stored there overnight ③. The next morning, we merged the particles together ④. The number of particles is now reduced due to the fact that while some particles were stored in the Precision trap, evaporation studies were performed in the PT. Here, the trap potential is consecutively ramped down to have a shallow trap, at which point antiprotons with higher energy start to leave the trap. This information is important for the execution of the cleaning routines (see Chapter 5.3) and single particle preparation in the precision traps.
Nevertheless, particle loss occurred during the merging of an extraction attempt ⑦ after which the merging routine was optimized ⑧ and a single particle extraction ⑨ was performed.
A problem arising during the operation of the experiment was noise on the system, especially at the same frequency as the particles axial motion in the Reservoir trap. To counteract the noise heating of the particles, we changed the gate voltage of the amplifier of the resonator, which changes the resonance frequency. When changing the ring voltage of the particles accordingly, we can move the particles away from the noise peak. This, on the other hand, induces feedback effects on the resonator, which changes the Q-value of the resonator and with that also the interaction constant between particles and resonator.

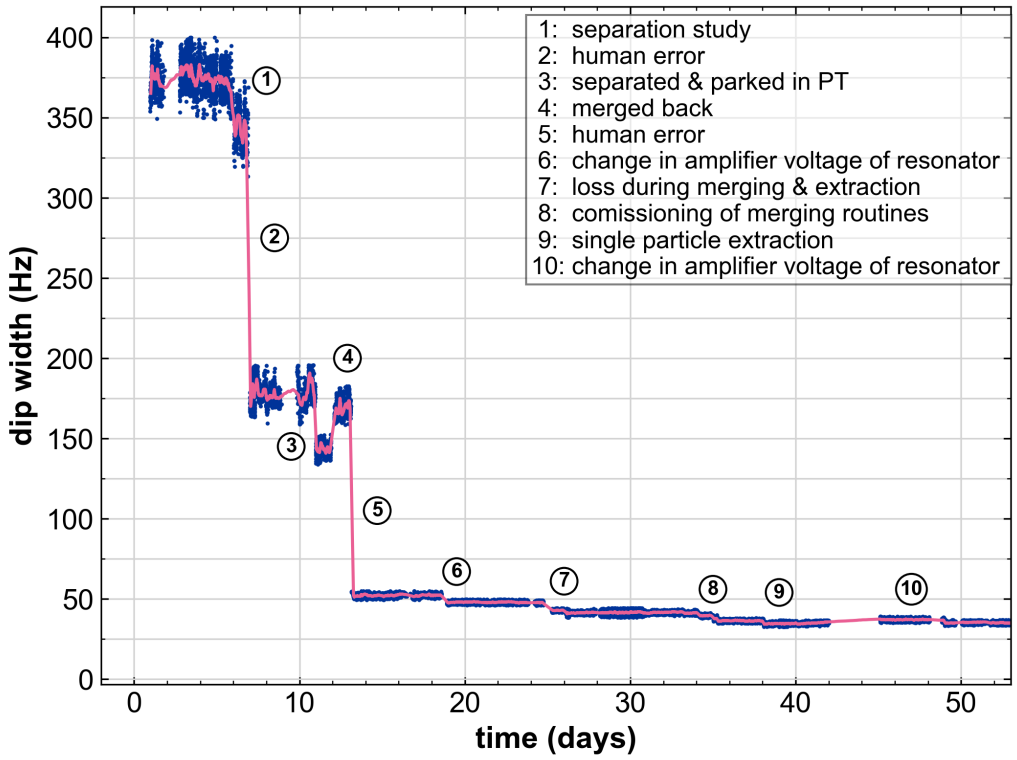

Figure 6.4: The first 53 days of the captured antiproton cloud in 2024. Shown is the dip width $\delta\nu_z$ as a function of measurement time after antiproton capture. The change in dip width can be correlated to different events as labeled. For example, also in an increase in dip width is visible (10) due to a change in the detector working point. More details can be found in the text.

This then can lead to a change in dip width as observed in (6) and (10) as a decrease and an increase, respectively, but does not represent a change in particle number.
The largest change in particle number is caused by human errors (2) & (5). Both times, the particles were heated out of the trap by accidently applying an rf-drive by accident. After these incidents, we developed clear routines in the operation of the antiproton reservoir, and no more losses of this nature occurred.

6.4.1 Particle number calibration

For the determination of the antiproton lifetime, the correct determination of the number of antiprotons stored in the Reservoir trap is of high importance. Therefore, we need to perform a careful particle number calibration. As mentioned above, during the run we had to change the working point of the resonator's amplifier and with this the effective parallel resistance $R_p = 2\pi\nu_{\mathrm{res}}LQ = 2\pi L\nu_{\mathrm{res}}^2/\delta\nu_{\mathrm{res}}$ of the resonator. Change of the amplifier working point affects the quality factor due to feedback and resistive damping, and thus, the single particle dip width (Equation (6.1)) changes. This means, that we need to be able to quantify the single particle dip width whenever the amplifier working point was changed. The simplest approach is to determine the inductance L of the coil and then calculate the single particle dip width for each recorded spectrum with the knowledge of the resonator's center frequency and its width, which is extracted using a least-squares fit to the data. We can calculate the single particle dip width for one working point by measuring the difference in dip width after a single particle extraction $\Delta\delta\nu_{\mathrm{z}} = \delta\nu_{\mathrm{z,before}} - \delta\nu_{\mathrm{z,after}}$.

This is deterministic and practically free of uncertainties, since we know that only a single particle was extracted by measuring the dip width of the extracted particle in the Precision trap, which is carefully calibrated as a part of the commissioning routine of the experiment. For this calibration, the single-particle dip width is determined by first loading a cloud of protons or antiprotons into the Precision trap, and slowly evaporating particles. To that end, the trapping potential is slowly decreased, so that hotter particles can escape the trap. Afterwards, the trap potential is increased to its previous value and the dip width is measured again. The decrease of the potential has to occur in small enough steps, so that only single particles will be evaporated. As this method involves particle losses, rather than applying it in the Reservoir trap, it consumes less particles to apply this protocol in the Precision trap for only a few particles. This calibration

extraction date	$\Delta\delta\nu_z$ (Hz)	uncertainty $\Delta\delta\nu_z$ (Hz)	L (mH)	uncertainty L (mH)
2023-12-04	1.63	0.2	1.362	0.167
2023-12-15	1.98	0.10	1.533	0.077
2024-03-01	1.84	0.02	1.429	0.016
2024-07-26	1.82	0.11	1.401	0.085

Table 6.2: Difference in dip width after a single particle extraction $\Delta\delta\nu_z = \delta\nu_{z,\text{before}} - \delta\nu_{z,\text{after}}$ and the corresponding calculated inductance of the RT resonator coil.

leads to a quasi-deterministic (CL $> 10\,\sigma$) measurement of the number of extracted particles. With the knowledge from the dip signal in the Precision trap, we can calculate the change in dip width in the RT during a single particle extraction by averaging over all measurements from the last change in dip width before the extraction $\delta\nu_{z,\text{before}}$ and after the extraction until the next change in dip width occurs $\delta\nu_{z,\text{after}}$, and subtracting both values $\Delta\delta\nu_z = \delta\nu_{z,\text{before}} - \delta\nu_{z,\text{after}}$. The inductance is then calculated using this change in dip width $\Delta\delta\nu_z$ as the single particle dip width and the mean of the resonator frequency and resonator width for the corresponding working point. For the determination of the inductance L only single particle extractions with sufficient statistics for the amount of stored antiprotons in the Reservoir trap before and after extraction were considered. Table 6.2 shows the determined single particle dip width and the calculated inductance for four single particle extractions.

Figure 6.5 a) visualizes the values from Table 6.2. The inductance of the resonator's coil is determined by the weighted mean of these four measurements and is $L = (1.432 \pm 0.015)\,\text{mH}$. Knowing the inductance of the coil, the single particle dip width is calculated for each spectrum using Equation (6.1) and the ν_{res} and $\delta\nu_{\text{res}}$ from least square fit of the line shape to the data. Dividing the fitted dip width of the spectra by this calculated single particle dip width gives us the particle number. The particle number calibration is illustrated in Figure 6.5 b). Here, a histogram of the particle number is shown, calculated from the extracted dip widths of all recorded spectra using the inductance L determined in Figure 6.5 a). For better visibility, only particle numbers after the second significant loss, e.g., after around 13 days of measurement time, are shown. This histogram shows data also presented in Figure 6.6.

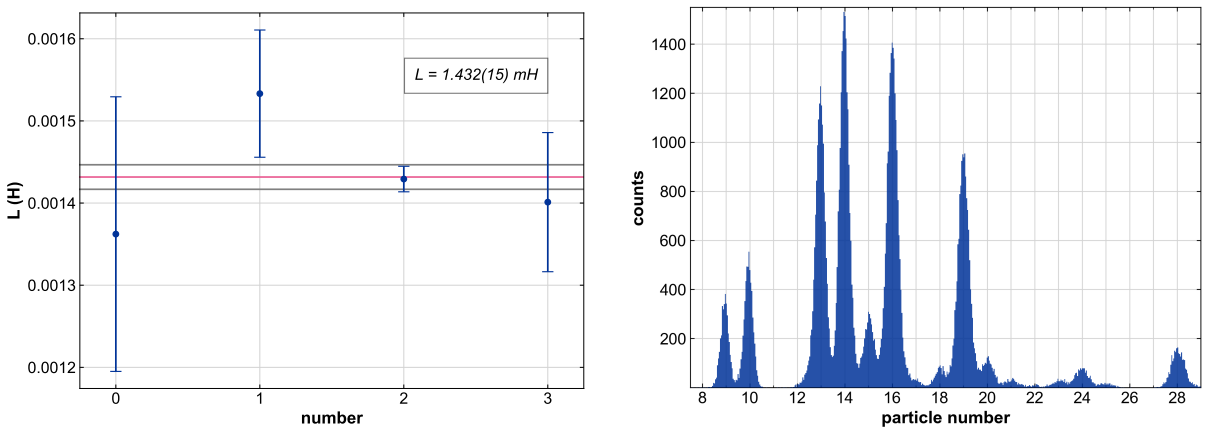

(a) Inductance of the RT coil

(b) Histogram of particle number after day 13

Figure 6.5: a) Extracted values for the determination of the inductance of the RT resonator coil. The weighted mean of the different values is $L = (1.432 \pm 0.015)\,\mathrm{mH}$ and depicted in pink. b) Histogram of the calculated particle numbers. For visibility, only the data after the second big loss (after day 13) is shown.

6.4.2 2023 - 2025 data

Figure 6.6 shows the evolution of stored antiprotons in the BASE Reservoir trap for the 2023 - 2025 run. The particle number extracted from the recorded FFT spectra is depicted in gray and blue. The gray points represent all data points after noise filtering, whereas the blue points are the ones used for the final determination of the equivalent single particle observation time. Selected are always the first 12 hours of observation time after the reservoir was maintained (see Chapter 5.5). The pink line is a moving average of the blue points, and the yellow dashed line represents the number of particles projected to an integer value. It is used to calculate a conservative estimate on the equivalent single particle observation time by integration, and the resulting evolution of the recorded observation time $T_{\mathrm{obs},2025} = 28.06$ years is shown as the dashed blue line in Figure 6.6 a).

Figure 6.6 b) shows the particle number after finishing the commissioning of the experiment, once the g-factor measurement started. This time is marked by the gray line in Figure 6.6 a). Remarkable is the low loss rate of only nine particles in over 1.5 years one particle per two months. During the first two months, we measured the g-factor and part of the systematics in the precision traps (AT & PT), which was lossless. Afterwards, we lost three particles during particle transports between the Precision and the Analysis trap. We attribute this to heavy electron contamination in the transport section between

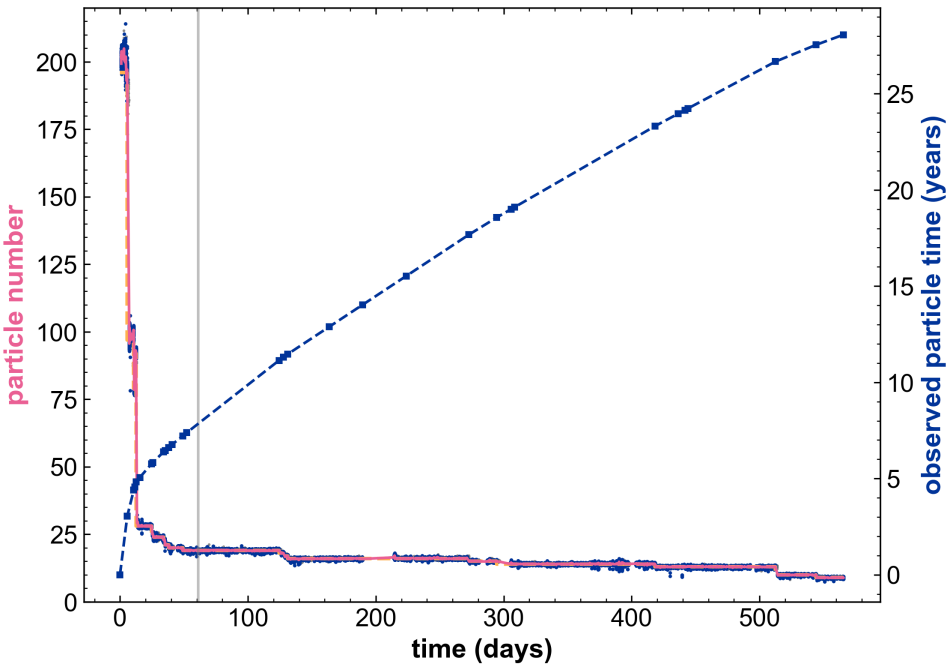

(a) Particle number and exposure (2023 -2025)

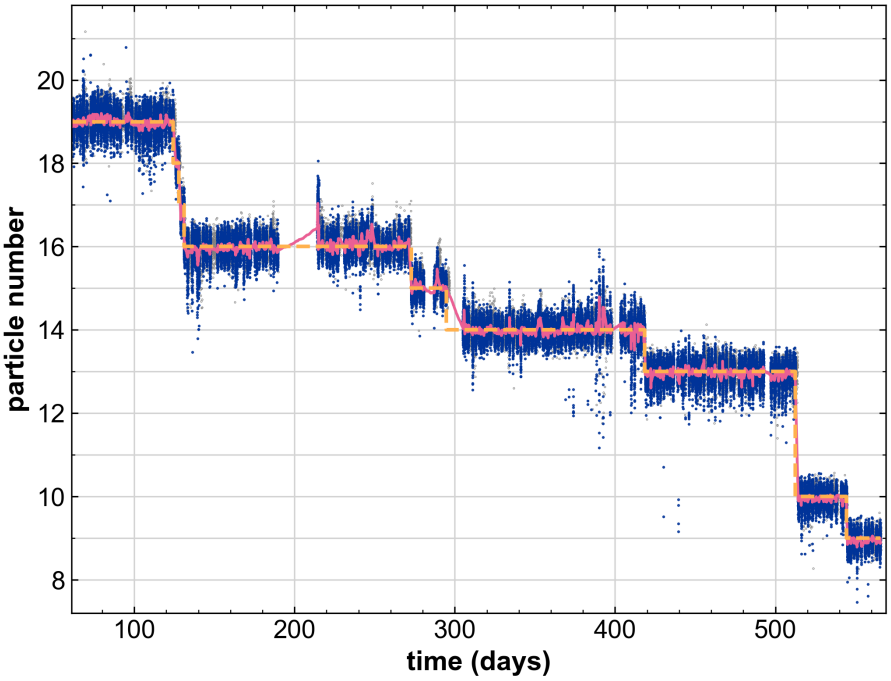

(b) Particle number after the experiment commissioning (2023 - 2025)

Figure 6.6: The particle number (pink) over time calculated with the RT inductance extracted in Figure 6.5. The dashed blue line in a) shows the integrated single particle equivalent storage time in years. b) is an excerpt of a) starting by the gray line marking the start of the g-factor measurement. More details in the text.

Day	Date	number before	number after	cause of loss
126	2024-03-01	19	18	contaminated transport section
129	2024-03-04	18	17	contaminated transport section
131	2024-03-06	17	16	contaminated transport section
273	2024-07-26	16	15	9-pole mode implementation
294	2024-08-07	15	14	phase methods implementation
419	2024-12-19	14	13	human error
497	2025-03-07	-	-	contaminated transport section
514	2025-03-24	13	10	human error
545	2025-04-24	10	9	human error

Table 6.3: Particle losses since the beginning of the precision measurement campaign on 2023-12-28 and reservoir content before and after the extraction of the corresponding particle loss in the precision measurement traps. Only 9 particles were lost in over 1.5 years of measurement time, resulting in a particle consumption rate of one particle per two months. Note that on 2025-03-07, a particle was lost in the precision traps, but no particle was extracted from the RT. On 2025-03-24, a particle got lost in the precision traps, due to a human mistake. Subsequently, two particles were extracted from the RT into the precision traps, and one particle was lost in the process.

the two precision measurement traps, as no particle was transported between the traps for a month after the g-factor measurement ended. After cleaning the transport electrodes between the two traps multiple times, no more particle loss occurred for 4.5 months. Then the implementation of new experimental techniques like a 9-pole mode in the Analysis trap [160] and phase-sensitive detection in the Precision trap [161] caused the loss of two more particles, which was followed again by a lossless period of four months. Table 6.3 summarizes particle loss events during the precision modus of the experiment, which, due to the excellent performance of the experiment, also includes the implementation of novel methods with minimal particle loss.

The stored antiproton cloud can also be used as a vacuum gauge. Following the approach presented in [162], we first determine a lower lifetime limit of the current antiproton run $\tau_{\overline{\mathrm{p}},2025}$ using the extracted observation time of $T_{\mathrm{obs},2025} = 28.06$ years, resulting in $\tau_{\overline{\mathrm{p}},2025} > 24.62$ (CL: 0.68) years. This allows us to estimate the hydrogen partial pressure to be smaller than $p_{\mathrm{H}} < 3.5 \times 10^{-19}$ mbar and helium partial pressure to $p_{\mathrm{He}} < 8.0 \times 10^{-19}$ mbar. Note that this corresponds in our trap can volume of 1.2 l to 750 particles (H) to 1750 particles (He) residual rest-gas particles in the entire volume of the trap vacuum chamber. To our knowledge, assuming the laws of thermodynamics hold

at these low particle numbers – this is the best ever explicitly characterized vacuum in a physics experiment on earth.

All in all, this demonstrates an unprecedented reduction in the particle consumption, as few as one particle per two months. Such a low particle consumption rate highlights the feasibility of prolonged measurement campaigns, and the possibility of conducting high-precision measurements also on ultra-rare species, such as antideuterium and the antihydrogen molecular ion $\bar{H}_2^-$.

6.5 Improved antiproton lifetime limits

So far, this Chapter has discussed the determination of the observed equivalent single antiproton storage time T_{obs} in the BASE Reservoir trap for three different runs. During this period, no unexplainable particle losses occurred, and a lower limit on the antiproton lifetime can be extract.

As described in Section 6.2, the observed equivalent single antiproton storage times from different runs can be combined, and, in addition, the storage time of the antiprotons in the precision measurement traps can be included. This comprises one additional particle stored in the Precision trap during the charge-to-mass ratio run (2017–2019), and two additional particles during the g-factor run (2023–2025). Moreover, the observation times from previous measurements reported in [59] and [118] can be incorporated as well. Table 6.4 summarizes all equivalent antiproton years observed in BASE.

These contributions result in a total equivalent single-particle observation time of $T_{\overline{\text{p}},\text{total}} = 66.24$ years and, incorporating the lower limits extracted for the mixed particle clouds from 2017 - 2019, a lower limit of $T_{\overline{\text{p}},\text{total,lower}} = 59.87$ years. From this, we extract a direct lower lifetime limit using Equation (6.7) of $\tau_{\overline{\text{p}},\text{lower}} = 52.54$ years (CL: 0.68) and $\tau_{\overline{\text{p}},\text{lower}} = 19.98$ years (CL: 0.95), increasing the direct lifetime limit by a factor of five compared to the previously published best value [59].

In the future, a dedicated experiment could provide an increased limit on the antiproton lifetime. This could be realized with a permanent magnet trap, which BASE is currently developing [163]. Given the efficiency of the BASE Reservoir trap, it is feasible to store hundreds to thousands of antiprotons in an optimized trap. Considering the trapping of approximately 1000 antiprotons over three years in such a trap, a lower direct limit on the antiproton lifetime of approximately 2 600 years could be extracted.

Run	Observed particle years $\overline{p}$	Observed particle years $\overline{p}$ (lower limit)
2014 [118]	1.56 a	1.56 a
2016 [59]	10.10 a	10.10 a
2017/2018	14.37 a	11.58 a
2017/2018 other	0.52 a	0.52 a
2018/2019	8.50 a	4.92 a
2018/2019 other	0.63 a	0.63 a
2023 - 2025	28.06 a	28.06 a
2023 - 2025 other	2.5 a	2.5 a
Total	66.24 a	59.87 a

Table 6.4: Summary of all observed equivalent antiproton years recorded in BASE from 2014 - 2025.

Chapter 7

Conclusion and Outlook

The BASE experiment tests CPT symmetry by comparing the fundamental properties of protons and antiprotons with the highest possible precision, like the charge-to-mass ratio [55], the magnetic moment [56], and the lifetime [59]. This enables, for example, to constrain coefficients in the SME framework [32] and to set stringent boundaries on the Standard Model of particle physics. The goal of such experiments is to steadily improve the fractional resolution with which these properties can be measured, by new experimental inventions and upgraded technology.

This thesis has discussed a novel cooling device for improved cyclotron-mode cooling of a single trapped antiproton in a Penning trap. It comprises a cyclotron resonator and a dedicated Penning trap with an optimized design for strong particle-resonator coupling. A low cyclotron-mode temperature is crucial for the thermal stability and signal-to-noise ratio of antiproton frequency measurements, and for low spurious mode-heating rates [122]. In previous g-factor measurements [56, 138], cooling the particle's cyclotron mode required several hours and had to be repeated approximately every second day [56], resulting in a significant reduction of the effective measurement time and introducing statistical uncertainty. This is particularly problematic due to the limited window available for precision measurements in the noisy environment of the Antimatter Factory.

With the here presented novel mode-cooling device, the cold particle preparation time was reduced from about 15 h to 8 min resulting in an about 100× improved cooling time. Using this device, it is also feasible to cool the cyclotron mode to even lower temperatures, enabling measurements at improved frequency stability, which in turn results in a decreased spin state identification error rate. In this thesis, the detection of antiproton spin transitions with an error rate $< 2.3 \times 10^{-5}$ was demonstrated, which is more than three orders of magnitude better than in previous experiments [56].

Moreover, this thesis presents the optimization and routine operation of the unique antiproton Reservoir trap [118]. It is pivotal in conducting precision experiments in BASE, as it supplies the BASE experiment with rare antiprotons during the accelerator shutdown – the only time BASE can perform high-precision measurements. A detailed overview of the configuration of the Reservoir trap was given, as well as a discussion on antiproton catching, the subsequent cleaning and maintenance of the stored antiproton cloud. With these methods, a particle consumption rate as low as one particle per two months was established. This unprecedented efficiency extends the feasibility of long-term measurement campaigns and opens up new possibilities for experiments with extremely rare antimatter species, such as antihydrogen molecular ions, that might become available in the future [164].

Thanks to careful maintenance of the antiproton cloud, antiprotons captured in October 2023 have remained stably confined in the Reservoir trap for over 1.5 years – the longest demonstrated storage of baryonic antimatter. Continuous monitoring during this period enabled a new direct lower limit on the antiproton lifetime [59]. This thesis presents the methods used to verify long-term storage integrity and the statistical framework behind the updated result, which incorporates data from the 2017/2018 and 2018/2019 runs to establish a new lifetime limit of 52.54 years.

In conclusion, this thesis reports significant advancements in precision antimatter research. A newly developed cooling device reduced the cyclotron-mode cooling time by a factor of about 100 compared to the previous antiproton g-factor campaign by BASE [56]. This innovation enabled a new g-factor measurement with roughly ten times lower statistical uncertainty, marking a major step forward, even as systematic investigations continue. Additionally, novel techniques for the long-term storage of exotic antiprotons were introduced, achieving a still-ongoing confinement duration of 1.5 years – the longest ever demonstrated for baryonic antimatter. This breakthrough enabled a fivefold improvement in the direct limit on the antiproton lifetime. Together, these accomplishments represent substantial progress toward more precise tests of fundamental symmetries using antimatter.

7.1 Outlook

7.1.1 Cyclotron-mode cooling

The improved cyclotron-mode cooling presented in this thesis could be further enhanced by either decreasing the time of one cycle in the sub-thermal cooling protocol or by reducing the temperature of the cyclotron detection system. In order to reduce the required time for one cooling cycle, cyclotron cooling and temperature readout could happen simultaneously by monitoring the axial frequency. Currently, the Cooling trap is equipped with an axial resonator, but patch potentials on the electrodes could result in a higher axial frequency than predicted. For this reason, a new axial resonator at a higher frequency was built [165] and will be implemented the next time the experimental apparatus is opened. With this, the transport between the Cooling and Analysis trap is no longer necessary, which decreases the time budget per cooling cycle by approximately 1.5. Additionally, the temperature of the cyclotron resonator can be reduced by applying negative feedback (see Chapter 2.2.2). This would lead to a further decrease in cooling time.

The two-particle method (Chapter 4.1.3), which is currently used to determine the antiproton magnetic moment, was essential for its p.p.b.-determination, but has its natural limits. During the application of the Larmor drive, the Larmor particle – used for spin state identification – is subject to thermal drifts within the apparatus and voltage settling effects on the trap electrodes. These factors introduce uncertainties in the assumption that the magnetic field remains stable between the cyclotron frequency measurement and the Larmor drive application. In order to counteract these uncertainties, a double-trap measurement scheme (Chapter 4.1.2) can be used. In this single-particle method, the most significant limitation for a high-precision g-factor measurement in an accelerator facility was the low sampling statistics, imposed by the long cyclotron-mode cooling times of several hours. With the presented novel cooling device, the cold particle preparation time is significantly reduced to only 8 minutes, making a double-trap measurement feasible again, also in the AMF of CERN. Further improvements for implementing the double-trap method are currently being developed, for example, faster spin flip identification methods, and can be found in [166].

7.1.2 Antiproton lifetime

The presented result of 52.54 years on the lower direct limit on the antiproton lifetime could be immensely increased with a dedicated experiment. In the BASE precision experiment, the number of antiprotons is typically reduced to around 30, in order to facilitate experimental operation. With optimized catching parameters, we estimate it feasible to trap a cloud of 1000 - 10 000 antiprotons, which can be maintained without losses. In addition, it must be ensured that the detection system is optimized to resolve individual particles. Such a dedicated experiment could be realized within the BASE future program [163] of a permanent magnet Penning trap, which could be supplied by the transportable trap system BASE-STEP [61]. Considering the trapping of approximately 1000 antiprotons over three years in such a trap, a lower direct limit on the antiproton lifetime of approximately 2 600 years could be extracted.

For a larger amount of stored antiprotons, different detection methods have to be utilized. With a time projection chamber (TPC) based detector, surrounding the trap, the ALPHA collaboration is able to distinguish the annihilation of single antihydrogen atoms [39]. Additionally, particle losses due to heating effects or annihilation with background gas could also be monitored with such a detection system and could distinguish between antiproton annihilation [145] and possible decay products [156]. The PUMA collaboration would be able to increase the limit on the antiproton's direct lifetime with a large number of trapped particles. Their experiment is equipped with a TPC and aims to store 10^9 antiprotons in their trap [43]. With only one day of antiproton storage, they could, in principle, set a lower direct limit on the antiproton lifetime of approximately 10^6 years.

7.1.3 BASE collaboration

After successful antiproton catching in October 2023, the BASE collaboration commissioned the experimental apparatus and sampled antiproton g-factor resonances during the accelerator down times, culminating in an approximately ten times reduced statistical uncertainty compared to the previous measurement [56], with still ongoing systematic studies. Moreover, the first coherent g-factor resonance has been measured [167].

The future strategy of BASE has been laid out recently in the BASE Future Proposal [163]. The long-term goal of the BASE experiment is to further increase the precision on the fundamental properties of protons and antiprotons. To this end, the BASE-CERN apparatus will be used as a dedicated charge-to-mass ratio experiment in an

off-line laboratory at CERN, supplied by the transportable trap BASE-STEP [61], which recently demonstrated the first proton transport [62]. A new experiment at Heinrich-Heine-Univeristät (HHU) is currently under development and will function as a g-factor apparatus, which will also be supplied with antiprotons by BASE-STEP.

By establishing an extremely low particle consumption rate of one particle per two months while performing a precision measurement, as demonstrated in this thesis, the BASE collaboration has shown the feasibility of conducting such measurements also on ultra-rare species, such as antideuterium and the antihydrogen molecular ion $\bar{H}_2^-$, which could be achieved in the future.

Publications

[I] F. Völksen, J. A. Devlin, M. J. Borchert, et al., "A high-Q superconducting toroidal medium frequency detection system with a capacitively adjustable frequency range > 180 kHz", Review of Scientific Instruments **93**, 093303 (2022),
No explicit references.

[II] B. M. Latacz, B. P. Arndt, B. B. Bauer, et al., "BASE—high-precision comparisons of the fundamental properties of protons and antiprotons", The European Physical Journal D **77**, 94 (2023),
Referenced in Chapter 4.

[III] B. M. Latacz, B. P. Arndt, J. A. Devlin, et al., "Ultra-thin polymer foil cryogenic window for antiproton deceleration and storage", Review of Scientific Instruments **94**, 103310 (2023),
Referenced in Chapters 3, 5 & 6.

[IV] C. Smorra, F. Abbass, D. Schweitzer, et al., "BASE-STEP: a transportable antiproton reservoir for fundamental interaction studies", Review of Scientific Instruments **94**, 113201 (2023),
Referenced in Chaptes 1, 3, 5 & 7.

[V] M. Wiesinger, F. Stuhlmann, M. Bohman, et al., "Trap-integrated fluorescence detection with silicon photomultipliers for sympathetic laser cooling in a cryogenic Penning trap", Review of Scientific Instruments **94**, 123202 (2023),
No explicit references.

[VI] C. Will, M. Wiesinger, P. Micke, et al., "Image-Current Mediated Sympathetic Laser Cooling of a Single Proton in a Penning Trap Down to 170 mK Axial Temperature", Phys. Rev. Lett. **133**, 023002 (2024),
No explicit references.

[VII] B. M. Latacz, M. Fleck, J. I. Jäger, et al., "Orders of Magnitude Improved Cyclotron-Mode Cooling for Nondestructive Spin Quantum Transition Spectroscopy with Single Trapped Antiprotons", Phys. Rev. Lett. **133**, 053201 (2024),
Heavily referenced in Chapter 4 and referenced in Chapter 1.

[VIII] M. Leonhardt, D. Schweitzer, F. Abbass, et al., "Proton transport from the antimatter factory of CERN", Nature, (2025),
Referenced in Chapters 1 & 7.

References

[1] S. Navas, C. Amsler, T. Gutsche, et al., "Review of particle physics", Physical Review D **110**, 030001 (2024).

[2] G. Arnison, A. Astbury, B. Aubert, et al., "Experimental observation of isolated large transverse energy electrons with associated missing energy at s=540 GeV", Physics Letters B **122**, 103–116 (1983).

[3] M. Banner, R. Battiston, P. Bloch, et al., "Observation of single isolated electrons of high transverse momentum in events with missing transverse energy at the CERN $\overline{\mathrm{p}}\mathrm{p}$ collider", Physics Letters B **122**, 476–485 (1983).

[4] G. t. Arnison, A. Astbury, B. Aubert, et al., "Experimental observation of lepton pairs of invariant mass around 95 GeV/c2 at the CERN SPS collider", Physics letters B **126**, 398–410 (1983).

[5] P. Bagnaia, M. Banner, R. Battiston, et al., "Evidence for $\mathrm{Z}^0 \rightarrow \mathrm{e}^+\mathrm{e}^-$ at the CERN $\overline{\mathrm{p}}\mathrm{p}$ collider", Physics Letters B **129**, 130–140 (1983).

[6] F. Abe, H. Akimoto, A. Akopian, et al., "Observation of top quark production in $\overline{\mathrm{p}}\mathrm{p}$ collisions with the collider detector at Fermilab", Physical review letters **74**, 2626 (1995).

[7] S. Abachi, B. Abbott, M. Abolins, et al., "Search for high mass top quark production in $\mathrm{p}\overline{\mathrm{p}}$ collisions at s= 1.8 TeV", Physical review letters **74**, 2422 (1995).

[8] G. Aad, T. Abajyan, B. Abbott, et al., "Observation of a new particle in the search for the Standard Model Higgs boson with the ATLAS detector at the LHC", Physics Letters B **716**, 1–29 (2012).

[9] S. Chatrchyan, V. Khachatryan, A. Sirunyan, et al., "Observation of a new boson at a mass of 125 GeV with the CMS experiment at the LHC", Physics Letters B **716**, 30–61 (2012).

[10] Planck Collaboration, Aghanim, N., Akrami, Y., et al., "Planck 2018 results - VI. Cosmological parameters", A&A **641**, A6 (2020).

[11] F. Capozzi, E. Lisi, A. Marrone, et al., "Neutrino masses and mixings: status of known and unknown 3ν parameters", Nuclear Physics B **908**, 218–234 (2016).

[12] G. Lüders, "Proof of the TCP theorem", Annals of Physics **2**, 1–15 (1957).

[13] W. Pauli, "Pauli Manuscript Collection: Exclusion Principle, lorentz Group and reflection of space-time and charge", Typed (original) with annotations by Wolfgang Pauli.

[14] M. Dine and A. Kusenko, "Origin of the matter-antimatter asymmetry", Reviews of Modern Physics **76**, 1 (2003).

[15] B. Gato-Rivera, *Antimatter* (Springer, 2021).

[16] L. Canetti, M. Drewes, and M. Shaposhnikov, "Matter and antimatter in the universe", New Journal of Physics **14**, 095012 (2012).

[17] A. Sakharov, "Violation of CP-invariance, C-asymmetry, and baryon asymmetry of the universe", Usp. Fiz. Nauk **161**, 61–64 (1991).

[18] A. D. Sakharov, "Baryon asymmetry of the universe", Soviet Physics Uspekhi **34**, 417 (1991).

[19] J. H. Christenson, J. W. Cronin, V. L. Fitch, et al., "Evidence for the 2π decay of the K_2^0 meson", Phys. Rev. Lett. **13**, 138–140 (1964).

[20] V. Fanti, A. Lai, D. Marras, et al., "A new measurement of direct CP violation in two pion decays of the neutral kaon", Physics Letters B **465**, 335–348 (1999).

[21] A. Alavi-Harati, I. F. Albuquerque, T. Alexopoulos, et al. (KTeV Collaboration), "Observation of direct CP Violation in $K_{S,L} \to \pi\pi$ decays", Phys. Rev. Lett. **83**, 22–27 (1999).

[22] B. Aubert, D. Boutigny, I. De Bonis, et al. (BABAR Collaboration), "Measurement of CP-Violating Asymmetries in B^0 Decays to CP Eigenstates", Phys. Rev. Lett. **86**, 2515–2522 (2001).

[23] K. Abe, K. Abe, R. Abe, et al. (Belle Collaboration), "Observation of large CP violation in the neutral B meson system", Phys. Rev. Lett. **87**, 091802 (2001).

[24] R. Aaij, C. Abellan Beteta, B. Adeva, et al. (LHCb Collaboration), "First observation of CP violation in the decays of B_s^0 mesons", Phys. Rev. Lett. **110**, 221601 (2013).

[25] R. Aaij, C. Abellán Beteta, B. Adeva, et al. (LHCb Collaboration), "Observation of CP violation in charm decays", Phys. Rev. Lett. **122**, 211803 (2019).

[26] R. Aaij, A. S. W. Abdelmotteleb, C. A. Beteta, et al. (LHCb Collaboration), *Observation of charge-parity symmetry breaking in baryon decays*, 2025.

[27] O. Bertolami, D. Colladay, V. Kostelecký, et al., "CPT violation and baryogenesis", Physics Letters B **395**, 178–183 (1997).

[28] R. Lehnert, "CPT symmetry and its violation", Symmetry **8**, 114 (2016).

[29] V. A. Kosteleckỳ and S. Samuel, "Spontaneous breaking of lorentz symmetry in string theory", Physical Review D **39**, 683 (1989).

[30] D. Colladay and V. A. Kostelecký, "CPT violation and the standard model", Phys. Rev. D **55**, 6760–6774 (1997).

[31] D. Colladay and V. A. Kostelecký, "Lorentz-violating extension of the standard model", Phys. Rev. D **58**, 116002 (1998).

[32] V. A. Kosteleckỳ and N. Russell, "Data tables for Lorentz and CPT violation", Reviews of Modern Physics **83**, 11 (2011).

[33] B. Schwingenheuer, R. Briere, A. Barker, et al., "CPT tests in the neutral kaon system", Physical review letters **74**, 4376 (1995).

[34] R. S. Van Dyck Jr, P. B. Schwinberg, and H. G. Dehmelt, "New high-precision comparison of electron and positron g factors", Physical Review Letters **59**, 26 (1987).

[35] D. P. Aguillard, T. Albahri, D. Allspach, et al., "Measurement of the positive muon anomalous magnetic moment to 0.20ppm", Physical Review Letters **131**, (2023).

[36] V. Chohan, ed., *Extra Low ENergy Antiproton (ELENA) ring and its transfer lines: design report*, en, CERN 2014,2 (CERN, Geneva, 2014),

[37] P. Scampoli and J. Storey, "The AEgIS experiment at CERN for the measurement of antihydrogen gravity acceleration", Modern Physics Letters A **29**, 1430017 (2014).

[38] R. Akbari, B. Alves, C. Baker, et al., "The ALPHA-2 apparatus - facilitating experimentation with trapped antihydrogen", Nuclear Instruments and Methods in Physics Research Section A: Accelerators, Spectrometers, Detectors and Associated Equipment **1072**, 170194 (2025).

[39] E. K. Anderson, C. J. Baker, W. Bertsche, et al., "Observation of the effect of gravity on the motion of antimatter", en, Nature **621**, Publisher: Nature Publishing Group, 716–722 (2023).

[40] E. Widmann, C. Amsler, S. Arguedas Cuendis, et al., "Hyperfine spectroscopy of hydrogen and antihydrogen in ASACUSA", Hyperfine Interactions **240**, 1–7 (2019).

[41] C. Smorra, K. Blaum, L. Bojtar, et al., "BASE – The Baryon Antibaryon Symmetry Experiment", The European Physical Journal Special Topics **224**, 3055–3108 (2015).

[42] P. Perez and Y. Sacquin, "The GBAR experiment: gravitational behaviour of antihydrogen at rest", Classical and Quantum Gravity **29**, 184008 (2012).

[43] T. Aumann, W. Bartmann, O. Boine-Frankenheim, et al., "PUMA, antiProton unstable matter annihilation: PUMA collaboration", The European Physical Journal A **58**, 88 (2022).

[44] M. Diermaier, C. Jepsen, B. Kolbinger, et al., "In-beam measurement of the hydrogen hyperfine splitting and prospects for antihydrogen spectroscopy", Nature communications **8**, 15749 (2017).

[45] A. Sótér, H. Aghai-Khozani, D. Barna, et al., "High-resolution laser resonances of antiprotonic helium in superfluid 4He", Nature **603**, 411–415 (2022).

[46] M. e. a. Amoretti, "Production and detection of cold antihydrogen atoms", Nature **419**, (2002).

[47] G. Gabrielse, N. S. Bowden, P. Oxley, et al. (ATRAP Collaboration), "Background-free observation of cold antihydrogen with field-ionization analysis of its states", Phys. Rev. Lett. **89**, 213401 (2002).

[48] G. Andresen, M. Ashkezari, M. Baquero-Ruiz, et al., "Trapped antihydrogen", Nature **468**, 673–676 (2010).

[49] M. Ahmadi, B. Alves, C. Baker, et al., "Observation of the hyperfine spectrum of antihydrogen", Nature **548**, 66–69 (2017).

[50] M. Ahmadi, B. Alves, C. Baker, et al., "Characterization of the 1s–2s transition in antihydrogen", Nature **557**, 71–75 (2018).

[51] C. Baker, W. Bertsche, A. Capra, et al., "Laser cooling of antihydrogen atoms", Nature **592**, 35–42 (2021).

[52] M. Ahmadi, B. Alves, C. Baker, et al., "Adiabatic expansion cooling of antihydrogen", Physical Review Research **6**, L032065 (2024).

[53] R. Caravita, A. C. Mathad, J. Hangst, et al., "CERN AD/ELENA Antimatter Program", arXiv preprint arXiv:2503.22471 (2025).

[54] S. Ulmer, C. Smorra, A. Mooser, et al., "High-precision comparison of the antiproton-to-proton charge-to-mass ratio", Nature **524**, 196–199 (2015).

[55] M. J. Borchert, J. A. Devlin, S. R. Erlewein, et al., "A 16-parts-per-trillion measurement of the antiproton-to-proton charge–mass ratio", Nature **601**, 53–57 (2022).

[56] C. Smorra, S. Sellner, M. Borchert, et al., "A parts-per-billion measurement of the antiproton magnetic moment", Nature **550**, 371–374 (2017).

[57] G. Schneider, A. Mooser, M. Bohman, et al., "Double-trap measurement of the proton magnetic moment at 0.3 parts per billion precision", Science **358**, 1081–1084 (2017).

[58] C. Smorra and A. Mooser, "Precision measurements of the fundamental properties of the proton and antiproton", Journal of Physics: Conference Series **1412**, 032001 (2020).

[59] S. Sellner, M. Besirli, M. Bohman, et al., "Improved limit on the directly measured antiproton lifetime", New Journal of Physics **19**, 083023 (2017).

[60] J. DiSciacca, M. Marshall, K. Marable, et al., "One-particle measurement of the antiproton magnetic moment", Physical review letters **110**, 130801 (2013).

[61] C. Smorra, F. Abbass, D. Schweitzer, et al., "BASE-STEP: a transportable antiproton reservoir for fundamental interaction studies", Review of Scientific Instruments **94**, 113201 (2023).

[62] M. Leonhardt, D. Schweitzer, F. Abbass, et al., "Proton transport from the antimatter factory of CERN", Nature, (2025).

[63] B. M. Latacz, M. Fleck, J. I. Jäger, et al. (BASE Collaboration), "Orders of Magnitude Improved Cyclotron-Mode Cooling for Nondestructive Spin Quantum Transition Spectroscopy with Single Trapped Antiprotons", Phys. Rev. Lett. **133**, 053201 (2024).

[64] S. Earnshaw, "On the nature of the molecular forces which regulate the constitution of the luminiferous ether", Transactions of the Cambridge Philosophical Society (1848).

[65] W. Paul and H. Steinwendel, "Ein neues massenspektrometer ohne magnetfeld", Z. Naturforschg. **8a** (1953).

[66] H. G. Dehmelt and F. L. Walls, ""bolometric" technique for the rf spectroscopy of stored ions", Phys. Rev. Lett. **21**, 127–131 (1968).

[67] X. Fan, T. G. Myers, B. A. D. Sukra, et al., "Measurement of the electron magnetic moment", Phys. Rev. Lett. **130**, 071801 (2023).

[68] D. J. Wineland and H. G. Dehmelt, "Principles of the stored ion calorimeter", Journal of Applied Physics **46**, 919–930 (1975).

[69] R. S. Van Dyck, P. B. Schwinberg, and H. G. Dehmelt, "New high-precision comparison of electron and positron g factors", Phys. Rev. Lett. **59**, 26–29 (1987).

[70] L. S. Brown and G. Gabrielse, "Geonium theory: physics of a single electron or ion in a penning trap", Rev. Mod. Phys. **58**, 233–311 (1986).

[71] F. Major, V. Gheorghe, and G. Werth, *Charged particle traps* (Springer, 2005).

[72] M. Vogel, *Particle Confinement in Penning Traps: An Introduction*, en, Vol. 126, Springer Series on Atomic, Optical, and Plasma Physics (Springer International Publishing, Cham, 2024),

[73] K. Blaum, S. Eliseev, and S. Sturm, "Perspectives on testing fundamental physics with highly charged ions in penning traps", Quantum Science and Technology **6**, 014002 (2020).

[74] H.-J. Kluge, "Penning trap mass spectrometry of radionuclides", International Journal of Mass Spectrometry **349**, 26–37 (2013).

[75] J. Dilling, K. Blaum, M. Brodeur, et al., "Penning-trap mass measurements in atomic and nuclear physics", Annual Review of Nuclear and Particle Science **68**, 45–74 (2018).

[76] M. Kretzschmar, "Particle motion in a penning trap", Eur. J. Phys **12**, 240–246 (1991).

[77] L. S. Brown and G. Gabrielse, "Precision spectroscopy of a charged particle in an imperfect penning trap", Phys. Rev. A **25**, 2423–2425 (1982).

[78] G. Gabrielse, L. Haarsma, and S. Rolston, "Open-endcap penning traps for high precision experiments", International Journal of Mass Spectrometry and Ion Processes **88**, 319–332 (1989).

[79] S. Ulmer, "First observation of spin flips with a single proton stored in a cryogenic penning trap", PhD thesis (Heidelberg University, 2011).

[80] F. C. Moon, *Chaotic vibrations: an introduction for applied scientists and engineers* (Wiley, New York, 1987).

[81] J. Ketter, T. Eronen, M. Höcker, et al., "First-order perturbative calculation of the frequency-shifts caused by static cylindrically-symmetric electric and magnetic imperfections of a penning trap", International Journal of Mass Spectrometry **358**, 1–16 (2014).

[82] G. Schneider, "300 ppt measurement of the proton g-factor", PhD thesis (Mainz University, 2017).

[83] J. L. V. Galiana, "Ultrapräzise Messung des elektronischen g-Faktors in wasserstoffähnlichem Sauerstoff", PhD thesis (Mainz University, 2003).

[84] M. Schuh, F. Heiße, T. Eronen, et al., "Image charge shift in high-precision penning traps", Physical Review A **100**, 023411 (2019).

[85] F. Heiße, F. Köhler-Langes, S. Rau, et al., "High-precision measurement of the proton's atomic mass", Physical Review Letters **119**, 033001 (2017).

[86] S. Erlewein, "Implementation of a superconducting shimming and shielding system in the base experiment", PhD thesis (Heidelberg University, 2024).

[87] P. Horowitz and W. Hill, *The art of electronics; 3rd ed.* (Cambridge University Press, Cambridge, 2015).

[88] H. Nagahama, G. Schneider, A. Mooser, et al., "Highly sensitive superconducting circuits at ∼700 kHz with tunable quality factors for image-current detection of single trapped antiprotons", Review of Scientific Instruments **87**, 113305 (2016).

[89] S. Ulmer, K. Blaum, H. Kracke, et al., "A cryogenic detection system at 28.9 mhz for the non-destructive observation of a single proton at low particle energy", Nuclear Instruments and Methods in Physics Research Section A **705**, 55–60 (2013).

[90] M. Fleck, "Towards a tenfold improvement on the measurement of the antiproton magnetic moment", PhD thesis (Tokyo University, 2022).

[91] J. Johnson, "Thermal agitation of electricity in conductors", Nature **119**, 50–51 (1927).

[92] H. Nyquist, "Thermal agitation of electric charge in conductors", Phys. Rev. **32**, 110–113 (1928).

[93] M. Borchert, "Challenging the Standard Model by high-precision comparisons of the fundamental properties of protons and antiprotons", PhD thesis (Leibniz University of Hannover, 2020).

[94] B. D'Urso, B. Odom, and G. Gabrielse, "Feedback Cooling of a One-Electron Oscillator", Physical Review Letters **90**, 4 (2003).

[95] C. Smorra, A. Mooser, M. Besirli, et al., "Observation of individual spin quantum transitions of a single antiproton", Physics Letters B **769**, 1–6 (2017).

[96] E. A. Cornell, R. M. Weisskoff, K. R. Boyce, et al., "Mode coupling in a Penning trap: Pulses and a classical avoided crossing", Physical Review A **41**, 312–315 (1990).

[97] H. Dehmelt, "Continous stern-gerlach effect: principles and idealized apperatus", Proc. Natl. Acad. Sci. USA **83**, 2291–2294 (1986).

[98] S. Ulmer, C. C. Rodegheri, K. Blaum, et al., "Observation of spin flips with a single trapped proton", Physical Review Letters **106**, 253001 (2011).

[99] J. Ellis, "Physics at the LHC", The European Physical Journal C-Particles and Fields **34**, 51–56 (2004).

[100] A. Myagkov, "Recent results from LHC experiments", Physics of Particles and Nuclei Letters **20**, 195–201 (2023).

[101] E. Kugler, "The ISOLDE facility", Hyperfine Interactions **129**, 23–42 (2000).

[102] R. Catherall, W. Andreazza, M. Breitenfeldt, et al., "The ISOLDE facility", Journal of Physics G: Nuclear and Particle Physics **44**, 094002 (2017).

[103] M. Hori and J. Walz, "Physics at CERN's Antiproton Decelerator", Progress in Particle and Nuclear Physics **72**, 206–253 (2013).

[104] C. Carli, D. Gamba, C. Malbrunot, et al., "ELENA: bright perspectives for low energy antiproton physics", Nuclear Physics News **32**, 21–27 (2022).

[105] E. Lopienska, *CERN accelerator complex*, https://cds.cern.ch/images/CERN-GRAPHICS-2022-001-1, Accessed: 2025-02-24.

[106] O. Chamberlain, E. Segrè, C. Wiegand, et al., "Observation of antiprotons", Phys. Rev. **100**, 947–950 (1955).

[107] S. Baird, D. Berlin, J. Boillot, et al., "The antiproton decelerator: AD", in Particle Accelerator Conference, 1997. Proceedings of the 1997, Vol. 1 (May 1997), 979–981 vol.1,

[108] S. Maury, "The Antiproton Decelerator: AD", en, Hyperfine Interactions **109**, 43–52 (1997).

[109] C. Amole, G. Andresen, M. Ashkezari, et al., "The ALPHA antihydrogen trapping apparatus", Nuclear Instruments and Methods in Physics Research Section A: Accelerators, Spectrometers, Detectors and Associated Equipment **735**, 319–340 (2014).

[110] C. Amsler, M. Antonello, A. Belov, et al., "Pulsed production of antihydrogen", Communications Physics **4**, 19 (2021).

[111] N. Kuroda, S. Ulmer, D. Murtagh, et al., "A source of antihydrogen for in-flight hyperfine spectroscopy", Nature communications **5**, 3089 (2014).

[112] P. Adrich, P. Blumer, G. Caratsch, et al., "Production of antihydrogen atoms by 6 keV antiprotons through a positronium cloud", en, The European Physical Journal C **83**, 1–11 (2023).

[113] M. Ahmadi, B. X. R. Alves, C. J. Baker, et al., "Observation of the 1S–2P Lyman-α transition in antihydrogen", en, Nature **561**, Publisher: Nature Publishing Group, 211–215 (2018).

[114] L. Nowak, C. Malbrunot, M. C. Simon, et al., "CPT and Lorentz symmetry tests with hydrogen using a novel in-beam hyperfine spectroscopy method applicable to antihydrogen experiments", Physics Letters B **858**, 139012 (2024).

[115] B. M. Latacz, B. P. Arndt, J. A. Devlin, et al., "Ultra-thin polymer foil cryogenic window for antiproton deceleration and storage", en, Review of Scientific Instruments **94**, 103310 (2023).

[116] S. Ulmer (BASE), *BASE-Annual Report 2023*, tech. rep. (CERN, Geneva, 2024).

[117] Apiezon, *Ultra high and high vacuum greases*, https://static.mimaterials.com/apiezon/DocumentLibrary/TechnicalDatasheets/Apiezon_L_M_and_N_Ultra_High_and_High_Vacuum_Greases_Datasheet.pdf, Accessed: 2025-05-11.

[118] C. Smorra, A. Mooser, K. Franke, et al., "A reservoir trap for antiprotons", International Journal of Mass Spectrometry **389**, 10–13 (2015).

[119] J. A. Devlin, E. Wursten, J. A. Harrington, et al., "Superconducting solenoid system with adjustable shielding factor for precision measurements of the properties of the antiproton", Physical Review Applied **12**, 044012 (2019).

[120] G. Gabrielse and J. Tan, "Self-shielding superconducting solenoid systems", Journal of Applied Physics **63**, 5143–5148 (1988).

[121] B. d'Urso, B. Odom, and G. Gabrielse, "Feedback cooling of a one-electron oscillator", Physical Review Letters **90**, 043001 (2003).

[122] M. Borchert, P. Blessing, J. Devlin, et al., "Measurement of ultralow heating rates of a single antiproton in a cryogenic penning trap", Physical Review Letters **122**, 043201 (2019).

[123] F. Voelksen, "Development of a precisely tuneable cryogenic low-loss capacitor for axion-like particle detection and precision measurements in penning traps" (Giessen University, 2021).

[124] S. Electronics, *UM series installation and user manual, rev 2025c*, https://www.stahl-electronics.com/devices/um/Manual_UM_LN_SW_V2025c.pdf, Accessed: 2025-03-06.

[125] S. R. Systems, *Um series installation and user manual, rev 2025c*, https://www.thinksrs.com/products/sr780.html, Accessed: 2025-04-26.

[126] Mini-Circuits, *Usb rf switch matrix*, https://www.minicircuits.com/pdfs/USB-8SPDT-A18.pdf?srsltid=AfmBOoqq-hOE01zn7nssYPjQbLZpPWUa_LmjBtQwDOFLLZCZmzKGQv--, Accessed: 2025-05-11.

[127] H. Nagahama, "High-precision measurements of the fundamental properties of the antiproton", PhD thesis (Tokyo University, 2017).

[128] X. Feng, M. Holzschneiter, M. Charlton, et al., "Capture and cooling of antiprotons", Hyperfine Interactions **109**, 145–152 (1997).

[129] B. R. Beck, J. Fajans, and J. H. Malmberg, "Temperature and anisotropic-temperature relaxation measurements in cold, pure-electron plasmas", Physics of Plasmas **3**, 1250–1258 (1996).

[130] G. Schneider, "Development of a penning trap system for the high precision measurement of the antiproton's magnetic moment" (Mainz University, 2014).

[131] X. Feng, M. Charlton, M. Holzscheiter, et al., "Tank circuit model applied to particles in a penning trap", Journal of Applied Physics **79**, 8–13 (1996).

[132] N. Schoen, "Optimizing catching efficiencies of antiprotons in a penning trap and developments towards resonant coupling of single protons and laser cooled beryllium ions" (Mainz University, 2018).

[133] L. S. Brown, "Geonium lineshape", Annals of Physics **159**, 62–98 (1984).

[134] H. Häffner, T. Beier, and S. e. a. Djekić, "Double penning trap technique for precise g factor determinations in highly charged ions", Eur. Phys. J. D **22** (2003).

[135] A. Mooser, S. Ulmer, K. Blaum, et al., "Direct high-precision measurement of the magnetic moment of the proton", Nature **509**, 596–599 (2014).

[136] A. Mooser, S. Bräuninger, K. Franke, et al., "Demonstration of the double penning trap technique with a single proton", Physics Letters B **723**, 78–81 (2013).

[137] S. Ulmer and et.al., *Technical design report base*, tech. rep. (CERN, 2013).

[138] H. Nagahama, C. Smorra, S. Sellner, et al., "Sixfold improved single particle measurement of the magnetic moment of the antiproton", Nature communications **8**, 1–7 (2017).

[139] A. Schneider, B. Sikora, and S. e. a. Dickopf, "Direct measurement of the 3He+ magnetic moments", Nature **606**, 878–883 (2022).

[140] W. M. Itano, J. C. Bergquist, J. J. Bollinger, et al., "Cooling methods in ion traps", Physica Scripta **1995**, 106 (1995).

[141] B. M. Latacz, B. P. Arndt, B. B. Bauer, et al., "BASE—high-precision comparisons of the fundamental properties of protons and antiprotons", en, The European Physical Journal D **77**, 94 (2023).

[142] G. Gabrielse, A. Khabbaz, D. Hall, et al., "Precision mass spectroscopy of the antiproton and proton using simultaneously trapped particles", Physical Review Letters **82**, 3198 (1999).

[143] S. Sturm, F. Köhler, J. Zatorski, et al., "High-precision measurement of the atomic mass of the electron", Nature **506**, 467–470 (2014).

[144] S. Orfanidis and V. Rittenberg, "Nucleon-antinucleon annihilation into pions", Nuclear Physics B **59**, 570–582 (1973).

[145] M. Hori, K. Yamashita, R. Hayano, et al., "Analog cherenkov detectors used in laser spectroscopy experiments on antiprotonic helium", Nuclear Instruments and Methods in Physics Research Section A: Accelerators, Spectrometers, Detectors and Associated Equipment **496**, 102–122 (2003).

[146] CAEN, *Technical specifications CAEN NDT1470*, `https://www.caen.it/products/ndt1470/`, Accessed: 2025-03-06.

[147] S. Electronics, *HV series data sheet, rev. 2013, v 2.2*, `https://www.stahl-electronics.com/bilder/HV_Series_Data-Sheet_2013_.pdf`, Accessed: 2025-03-06.

[148] L. Ponce, L. Bojtár, C. Carli, et al., "ELENA - From Commissioning to Operation", JACoW IPAC **2022**, 2391–2394 (2022).

[149] G. Gabrielse, X. Fei, L. A. Orozco, et al., "Cooling and slowing of trapped antiprotons below 100 mev", Phys. Rev. Lett. **63**, 1360–1363 (1989).

[150] C. Tseng and G. Gabrielse, "One-electron parametric oscillator", Appl. Phys. B **60**, 95–102 (1995).

[151] S. Guan and A. G. Marshall, "Stored waveform inverse fourier transform (swift) ion excitation in trapped-ion mass spectometry: theory and applications", International Journal of Mass Spectrometry and Ion Processes **157-158**, 5–37 (1996).

[152] G. Maero, "Cooling of highly charged ions in a penning trap for HITRAP", PhD thesis (Heidelberg University, 2008).

[153] M. Anderson, S. Andringa, E. Arushanova, et al. (The SNO+ Collaboration), "Search for invisible modes of nucleon decay in water with the SNO+ detector", Phys. Rev. D **99**, 032008 (2019).

[154] K. Abe, Y. Haga, Y. Hayato, et al., "Search for proton decay via p→ e+ π 0 and p→ μ+ π 0 in 0.31 megaton · years exposure of the super-kamiokande water cherenkov detector", Physical Review D **95**, 012004 (2017).

[155] S. H. Geer and D. C. Kennedy, "A new limit on the antiproton lifetime", The Astrophysical Journal **532**, 648 (2000).

[156] S. Geer, J. Marriner, M. Martens, et al., "New limit on CPT violation", Physical Review Letters **84**, 590 (2000).

[157] S. Geer, J. Marriner, M. Martens, et al. (The APEX Collaboration), "Erratum: new limit on *CPT* violation [phys. rev. lett. 84, 590 (2000)]", Phys. Rev. Lett. **85**, 3546–3546 (2000).

[158] K. Babu, J. C. Pati, and F. Wilczek, "Suggested new modes in supersymmetric proton decay", Physics Letters B **423**, 337–347 (1998).

[159] B. P. Arndt, "In preperation", PhD thesis (Heidelberg University, 2026).

[160] I. Ahrens, "Understanding the limits of the BASE antiproton spin state analysis trap" (Düsseldorf University, 2025).

[161] P. Geissler, "Phase-sensitive modified cyclotron frequency measurements of a single trapped antiproton" (Greifswald University, 2025).

[162] X. Fei, "Trapping low energy antiprotons in an ion trap", PhD thesis (Harvard, 1990).

[163] S. Ulmer (BASE), *BASE - Future Physics Program: From 2025 to 2034 and Beyond*, tech. rep. (CERN, Geneva, 2025).

[164] E. G. Myers, "*CPT* tests with the antihydrogen molecular ion", Phys. Rev. A **98**, 010101 (2018).

[165] B.-B. Bauer, "Development and characterisation of an ultra-sensitive superconducting image current detection system for protons and antiprotons in the frequency range of 2 MHz to 3.5 MHz" (Mainz University, 2023).

[166] S. Ulmer (BASE), *BASE - Annual Report 2024*, tech. rep. (CERN, Geneva, 2025).

[167] S. Ulmer, B. Latacz, S. Erlewein, et al., "Coherent spectroscopy with a single antiproton spin", Research Square (2025).

Acknowledgements

I would like to express my gratitude to Prof. Dr. Klaus Blaum for accepting me as his doctoral student and offering me the opportunity to pursue my PhD within the BASE collaboration at CERN. Klaus, thank you for your guidance, understanding, prompt responses to every email, and for your last-minute corrections. Thanks for taking me in!
I would like to extend my recognition to Prof. Dr. Ulrich Uwer for serving as the second referee for this thesis and to Prof. Dr. Mark Ladd and Prof. Dr. Joerg Jaeckel for completing the examination committee.

Next, I would like to thank Prof. Dr. Stefan Ulmer. Stefan, without you, this endeavor would not have been possible. Thanks for welcoming me into your group, for your confidence in me, for sharing your immense knowledge of physics and technology, and for always having an open ear – whether for physics questions or life in general. Thanks for sparking so much joy and motivation in everything you do, which is extremely contagious. I feel incredibly lucky and grateful for being able to work with and learn from you!

I would like to extend my thanks to the whole BASE team at CERN for their support and collaboration over the years, in no particular order: Ino Ahrens, Bela Arndt, Björn-Benny Bauer, Isabela Beine, Dr. Jack Devlin, Dr. Stefan Erlewein, Dr. Markus Fleck, Philip Geißler, Tomoka Imamura, Hanna Klett, Dr. Barbara Latacz, Jun.-Prof. Dr. Peter Micke, Phil Nuschke, Maylin Schiffelholz, Anton Siebert, Simon Stahl, Tesse Tiemens, Gilbertas Umbrazunas, Dr. Elise Wursten, Fatma Abbass, Satoshi Endo, Marcel Leonhardt, Daniel Schweitzer and Dr. Christian Smorra. I enjoyed working with every single one of you, and I'm very grateful for working on this brilliant experiment together!
I would like to thank the following people in particular:
Special thanks to Barbara for the countless hours in the lab, where sleep deprivation turned into singing, dancing, and eating (too many) sweets. Without your energy and stamina, the experiment would not be where it is today. Thank you for letting me learn

from you. I am certain that precision limits will be pushed further under your lead!
Elise, thank you for always being a calm presence and for sharing your knowledge and patiently explaining analysis methods and theoretical concepts to me.
Philip, Hanna, Anton, Isabela, and Tomoka, thank you for the fun adventures outside of work and all the laughs we shared as office mates. I also thank Philip for his patience with my Python skills.

I would also like to express my gratitude to everyone working in the Antimatter Factory for creating such a highly motivating working environment and good collaboration between the different experiments!

Furthermore, I would like to extend my sincerest thanks to everyone at the Max Planck Institute for Nuclear Physics for always making me feel at home when I visit. Especially my former colleagues from the EBIT and CSR groups, as well as everyone in the Blaum division, including Ludmila Hollmach, Britta Schwarz, and Gabi Weese: Thank you for your help in solving all administrative problems and for organizing the IMPRS retreats and seminars, and the MATS days, which were a blast!

Additionally, I recognize the support of the International Max Planck Research School for Precision Tests of Fundamental Symmetries with my co-supervisors PD Dr. Wolfgang Quint and especially apl. Prof. Dr. José R. Crespo López-Urrutia. José, I cannot thank you enough for being there for me every step of the way since I started my academic journey. I wouldn't be where I am today without you.

Moreover, I acknowledge the financial support of the Wolfgang Gentner scholarship program, funded by the German Federal Ministry for Education and Research, which has provided me with three years of funding for my doctoral student position; thank you for this generous support! I would like to express my gratitude to the CERN coordinators, Dr. Dominik Dannheim and Dr. Michael Hauschild, as well as Dr. Michael Doser, who generously agreed to act as my official CERN supervisor.

Then, I would like to thank my dear friends for their continuous support, kindness, and understanding! Thank you Ani, Anni, Bene, Clara, Laura, Leti, Lisa, Leonie, Luisa,

Mikko, Moritz, Rabea and Tobi.
Also biggest thanks to the "Crafting Society": thank you for all the fun evenings in R1!

Last but not least, I want to thank my parents for their unwavering support throughout my life, for their constant encouragement, and for always believing in me. My biggest thanks go to Hannes for enduring me during stressful times, for your support and understanding, and for always looking out for me! I'm also very thankful for physics discussions, Python support, and proofreading this thesis.

List of Figures

List of Tables